Large-eddy and direct simulation of turbulent flows

Ugo Piomelli
Department of Mechanical Engineering
University of Maryland
College Park, Maryland
USA

9e conférence annuelle de la Société canadienne de CFD

Contents

Chapter 1

INTRODUCTION

1.1 Motivation

Turbulence is a phenomenon that occurs frequently in nature, and has been the subject of study for several centuries. In 1510, Leonardo da Vinci accompanied a drawing of the vortices shed behind a blunt obstacle (Fig. 1.1) with the following observation:

> Observe the motion of the water surface, which resembles that of hair, that has two motions: one due to the weight of the shaft, the other to the shape of the curls; thus, water has eddying motions, one part of which is due to the principal current, the other to the random and reverse motion.

Although based entirely on speculation, and not accompanied by a mathematical analysis, this observation may be seen as a precursor to Reynolds' decomposition of velocity, pressure and other variables into mean and fluctuating parts.

Figure 1.1: Sketch from Leonardo da Vinci's notebooks.

Over the one-hundred and twenty years since Osborne Reynolds' experiments, much progress has been made. Statistical theories of turbulence have provided good understanding of the scaling laws in various flow regimes. Experimental studies have given great insight in the understanding of the structure of turbulent flows, particularly in the identification of the coherent eddies responsible for most of the energy production. Measurement techniques can now give single-point measurements of velocity and velocity gradient components using Laser-Doppler velocimetry or multiple wire anemometers, or velocity distributions in a plane, through Particle-Image or Particle-Tracking Velocimetry. A significant contribution to this progress, over the last thirty years, is due to the development of advancement numerical simulation methods for turbulent flows, such as the direct and large-eddy simulation. These techniques have made available data that had never been measurable previously: multi-point, unobtrusive measurements of velocity, velocity gradients, pressure, passive scalars etc. Although only over the last few years these techniques (and especially LES) have been used for more engineering-oriented configurations, the knowledge that has been gained from their application to simple, building-block flows, has been invaluable. Databases obtained from direct simulations have been used extensively for model validation and development, and have provided new insight on the physics of turbulent flows.

As the prediction and control of turbulent flows become increasingly important, the need for accurate models of turbulent flows is presently the pacing item for the development of design and analysis tools for the applications mentioned above. Large-eddy and direct simulations are two of the tools that can be used by the research and engineering communities to make inroads into this important problem.

1.2 Simulation techniques

Analytical or numerical solution of turbulent flow problems can be accomplished using various levels of approximation, yielding more or less detailed descriptions of the state of the flow. The simplest approach is to use semi-empirical correlations. Moody's diagram, which gives the skin friction factor for cylindrical pipes as a function of Reynolds number and relative roughness, is an example of this approach, which is especially useful for global, control-volume analyses, but yields no information on local quantities and relies heavily on the availability of experimental data in configurations similar to the one under study.

A more sophisticated method involves the use of Reynolds' averaging: the long-time average of a quantity f is defined as

$$\langle f \rangle = \frac{1}{T} \int_t^{t+T} f(\tau) d\tau, \tag{1.1}$$

where T is a time interval much longer than all the time scales of the turbulent flow. The averaging operation defined above permits one to decompose any quantity into its mean part, $\langle f \rangle$, and a fluctuating part, $f - \langle f \rangle$. If the averaging operation (1.1) is applied to the equations of motion, one obtains the well-known Reynolds-averaged Navier-Stokes equations (RANS), that describe the evolution of the mean quantities. The effect of turbulent fluctuations appears in a Reynolds stress term that must be modeled to close the system. A very wide range of models for the Reynolds stresses is available, ranging from simple, algebraic models, to $\mathcal{K}-\varepsilon$ models, to full or algebraic Reynolds stress closures. The solution of the RANS equations is now used in engineering applications to predict the flow in fairly complex configurations.

This approach suffers from one principal shortcoming: the fact that the model must represent a very wide range of scales. While the small scales tend to depend only on viscosity, and may be somewhat universal, the large ones are affected very strongly by the boundary conditions (see, for instance, the difference between the spanwise rollers present in mixing layers and wakes and the elongated streamwise vortices that are found in the near-wall region of a turbulent boundary layer). Thus, it does not seem possible to model the effect of the large scales of turbulence in the same way in flows that are very different.

Direct numerical simulations (DNS) of turbulence are the most straightforward approach to the solution of turbulent flows. In DNS the governing equations are discretized directly, and solved numerically. If the mesh is fine enough to resolve the smallest scales of motion, one can obtain an accurate three-dimensional, time-dependent solution of the governing equations completely free of modeling assumptions, and in which the only errors are those introduced by the numerical approximation. DNS makes it possible to compute and visualize any quantity of interest, including some that are difficult or impossible to measure experimentally, and to study the spatial relationships between flow variables (for instance, vorticity and energy production), to obtain insight on the detailed kinematics and dynamics of turbulent eddies.

DNS have been a very useful tool for the study of transitional and turbulent flow physics, but they have some limitations. First, the use of highly accurate, high-order schemes is desirable to limit dispersion and dissipation errors; these schemes (spectral methods, for example) tend to have little flexibility in handling complex geometries and general boundary conditions. Secondly, to resolve all the scales of motion, one requires a number of grid points proportional to the 9/4 power of the Reynolds number, Re, and the cost of the computation scales like Re^3 (see the discussion on the resolution requirements for LES and DNS in Section 3.1). For these reasons, DNS have largely been limited to simple geometries (flat plate, homogeneous flows) at low Reynolds numbers, and its application to engineering-type problems within the next decade appears unlikely.

Large-eddy simulations (LES) are a technique intermediate between the direct simulation of turbulent flows and the solution of the Reynolds-averaged equations. In LES the contribution of the large, energy-carrying structures to momentum and energy transfer is computed exactly, and only the effect of the smallest scales of turbulence is modeled. Since the small scales tend to be more homogeneous and universal, and less affected by the boundary conditions than the large ones, there is hope that their models can be simpler and require fewer adjustments when applied to different flows than similar models for the RANS equations.

LES are similar to DNS in that they provide a three-dimensional, time dependent solution of the Navier-Stokes equations. Thus, they still require fairly fine meshes. However, they can be used at much higher Reynolds numbers than DNS; ideally, in fact, if the small scales obey inertial-range dynamics, the cost of a computation is independent of Re (not, however, if a solid boundary is present). Among the objectives of LES are to provide data for lower-level turbulence models at Reynolds numbers beyond the reach of DNS, and to study more complex physics than can be addressed by DNS, in configurations closer to those of engineering interest.

In the past, the engineering community has mostly performed fairly well-resolved LES calculations of relatively simple flows, while in the meteorological community coarser calculations in which the resolution was inadequate near the solid boundaries have been prevalent. Although during the last decade the development of new, more accurate models for the unresolved scales has allowed the simulation of flows in more complex configurations than previously possible, the application of LES to actual technological applications hinges on the development of more efficient methodologies to represent the region near solid boundaries.

1.3 Objectives and plan

Purpose of these notes is to give the reader a flavor of the current state of LES and DNS. Over the next Chapters the required tools will be presented: governing equations, numerical methods, boundary conditions, resolution requirements will be discussed, and some achievements and applications of DNS will follow. Then, the discussion will be focused on the LES approach: several subgrid-scale models will be introduced, applications and future challenges will be presented. Some final remarks will conclude these notes.

The notes should be viewed as a tutorial, not as a comprehensive review of the area. The reader interested in more in-depth discussions of the subject is addressed to several recent reviews, in particular those by Lesieur & Métais (1995), Piomelli & Chasnov (1996), Moin (1997), Moin & Mahesh (1998), Piomelli (1999) and Meneveau & Katz (2000).

Chapter 2

PROBLEM FORMULATION

2.1 The Navier-Stokes equations

The equations governing the conservation of mass, momentum and energy in a viscous, Newtonian fluid are, in the absence of body forces:

$$\begin{aligned}
\frac{\partial \rho}{\partial t} + \frac{\partial}{\partial x_j}(\rho u_j) &= 0 && (2.1)\\
\frac{\partial \rho u_i}{\partial t} + \frac{\partial}{\partial x_j}(\rho u_i u_j) &= -\frac{\partial p}{\partial x_i} + \frac{\partial}{\partial x_j}\left[\mu\left(2S_{ij} - \frac{2}{3}\delta_{ij}S_{kk}\right)\right] && (2.2)\\
\frac{\partial e}{\partial t} + \frac{\partial}{\partial x_j}(u_j e) &= \frac{\partial Q}{\partial t} - \frac{\partial}{\partial x_j}\left(\kappa\frac{\partial T}{\partial x_j}\right), && (2.3)
\end{aligned}$$

where u_i is the velocity,[1] p the pressure, ρ the density of the fluid, μ its viscosity, $e = c_v T + \rho u_i u_i/2$ is the total energy per unit volume, c_v is the specific heat at constant volume, and T the temperature, $\partial Q/\partial t$ is the heat generation per unit volume, $\kappa = \alpha/\rho c_p$ is the molecular conductivity, c_p is the specific heat at constant pressure, α is the thermal diffusivity, and S_{ij} is the strain-rate tensor

$$S_{ij} = \frac{1}{2}\left(\frac{\partial u_i}{\partial x_j} + \frac{\partial u_j}{\partial x_i}\right). \tag{2.4}$$

An equation of state and a relationship that gives the viscosity as a function of the other state variables (Sutherland's law, for instance) close the system. For incompressible flows[2] with constant properties (2.1-2.3) reduce to

$$\begin{aligned}
\frac{\partial u_j}{\partial x_j} &= 0 && (2.5)\\
\frac{\partial u_i}{\partial t} + \frac{\partial}{\partial x_j}u_i u_j &= -\frac{1}{\rho}\frac{\partial p}{\partial x_i} + \nu\nabla^2 u_i, && (2.6)\\
\frac{\partial T}{\partial t} + \frac{\partial}{\partial x_j}u_j T &= \kappa\nabla^2 T. && (2.7)
\end{aligned}$$

where $\nu = \mu/\rho$; the equation for the temperature is decoupled from the momentum and mass conservation equations, in the absence of buoyancy effects.

2.2 The filtered Navier-Stokes equations

To separate the large from the small scales, LES is based on the definition of a filtering operation: a filtered (or resolved, or large-scale) variable, denoted by an overbar, is defined as

$$\overline{f}(\mathbf{x}) = \int_D f(\mathbf{x}')G(\mathbf{x},\mathbf{x}')d\mathbf{x}', \tag{2.8}$$

[1] Einstein's summation convention applies to repeated indices.
[2] The extension to compressible flows will be discussed in Section 7.1.

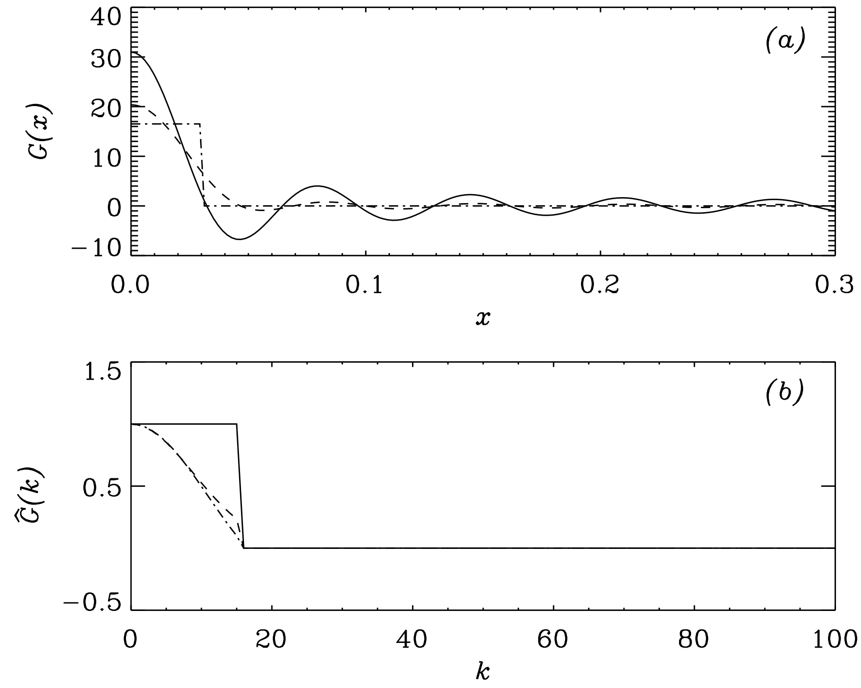

Figure 2.1: Typical filter functions. ——— : sharp Fourier cutoff; - - - : truncated Gaussian; —·— : tophat. (a) real space; (b) Fourier space.

where D is the entire domain and G is the *filter* function. The filter function determines the size and structure of the small scales. It is easy to show that, if G is a function of $x - x'$ only, differentiation and the filtering operation commute (Leonard 1974).

The most commonly-used filter functions are the sharp Fourier cutoff filter, best defined in wave space[3]

$$\widehat{G}(k) = \begin{cases} 1 & \text{if } k \leq \pi/\overline{\Delta} \\ 0 & \text{otherwise,} \end{cases} \tag{2.9}$$

the Gaussian filter,

$$G(x) = \sqrt{\frac{6}{\pi\overline{\Delta}^2}} \exp\left(-\frac{6x^2}{\overline{\Delta}^2}\right), \tag{2.10}$$

and the tophat filter in real space:

$$G(x) = \begin{cases} 1/\overline{\Delta} & \text{if } |x| \leq \overline{\Delta}/2 \\ 0 & \text{otherwise,} \end{cases} \tag{2.11}$$

These three filters and their Fourier transforms $\widehat{G}(k)$ are shown in Fig. 2.1. It should be noticed that in practice the Gaussian filter is always used in conjunction with a sharp Fourier cutoff; the truncation of the Gaussian at a non-negligible value is the cause for the ringing observed in the figure. For uniform filter width[4] $\overline{\Delta}$ the filters above are mean-preserving and commute with differentiation.

To illustrate the difference between the filters defined above they are applied to a test function obtained from random noise with a given spectrum; the spectra of the filtered variables are shown in Fig. 2.2. The tophat and Gaussian filters give similar results; in particular, they both smooth the large-scale fluctuations as well as the small-scale ones, unlike the Fourier cutoff, that only affects the scales below the cutoff wave-number.

If the filtering operation (2.8) is applied to the governing equations, one obtains the filtered equations of motion, which are solved in large-eddy simulations. For an incompressible flow of a Newtonian fluid,

[3] Unless otherwise noted, a quantity denoted by a caret $\widehat{\ }$ is the complex Fourier coefficient of the original quantity.
[4] For a discussion of filtering with non-uniform filters see Ghosal & Moin (1995).

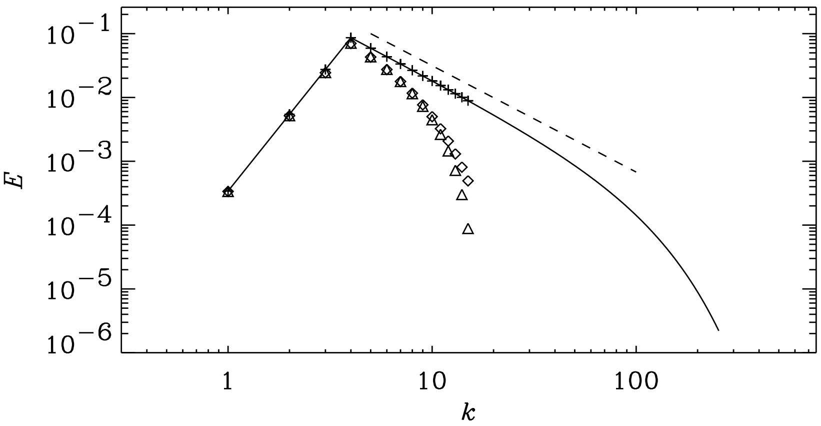

Figure 2.2: Filtering of a test function. ——— : Unfiltered; - - - $k^{-5/3}$; $+$: sharp Fourier cutoff; $\diamond$: Gaussian; $\triangle$: tophat.

they take the following form:

$$\frac{\partial \overline{u}_i}{\partial x_i} = 0. \tag{2.12}$$

$$\frac{\partial \overline{u}_i}{\partial t} + \frac{\partial}{\partial x_j}\left(\overline{u}_i \overline{u}_j\right) = -\frac{1}{\rho}\frac{\partial \overline{p}}{\partial x_i} - \frac{\partial \tau_{ij}}{\partial x_j} + \nu \frac{\partial^2 \overline{u}_i}{\partial x_j \partial x_j}. \tag{2.13}$$

The filtered Navier-Stokes equations, written above, govern the evolution of the large, energy-carrying, scales of motion. The effect of the small scales appears through a subgrid-scale (SGS) stress term,

$$\tau_{ij} = \overline{u_i u_j} - \overline{u}_i \overline{u}_j, \tag{2.14}$$

that must be modeled.

Chapter 3

NUMERICAL METHODS

In both direct and large-eddy simulations the governing equations (2.5-2.6) or (2.12-2.13) are discretized and solved numerically. For DNS, this straightforward approach presents nonetheless significant numerical challenges. In LES, the computational difficulties are slightly decreased, but modeling the small scales, the SGS stresses τ_{ij}, becomes an issue. In this Chapter, some consideration on numerical issues will be presented.

3.1 Resolution requirements

3.1.1 Direct simulations

The range of scales present in a turbulent flow is a strong function of the Reynolds number. Consider for instance the mixing layer shown in Fig. 3.1. The largest eddies in this flow are the spanwise rollers, whose scale is L; a very wide range of smaller scales is present, the smallest ones being the Kolmogorov scales η. The dissipation takes place in the non-dimensional wave-number band $0.1 < k\eta < 1.0$, which corresponds to a length scale band of about 6η to 60η.

In DNS, all the scales of motion, up to and including the dissipative scales of order η must be resolved; since the computational domain must be significantly larger than the large scale L, while the grid size must be of order η, the number of grid points required is proportional to the ratio $L/\eta \sim Re^{3/4}$ (where Re is the Reynolds number based on an integral scale of the flow). Thus, the number of grid points needed to perform a three-dimensional DNS scales like the 9/4 power of the Reynolds number.

The time-scale of the smallest eddies also supplies a bound for the maximum time-step allowed: since the ratio of the integral time-scale of the flow to the Kolmogorov time-scale is also proportional to $Re^{1/2}$ the number of time-steps required to advance the solution by a fixed time has the same dependence on Re. Assuming that the CPU time required by a numerical algorithm is proportional to the total number of points N, the cost of a calculation will depend on the product of the number of points by the number of time-steps, hence to $Re^{11/4}$.

For wall-bounded flows, the dependence of the calculation cost on the Reynolds number is even stricter. In the near-wall region, the appropriate scaling for the turbulent eddies responsible for the streaky structures shown in Fig. 3.2 is the viscous length-scale ν/u_τ, where $u_\tau = (\tau_w/\rho)^{1/2}$ is the friction

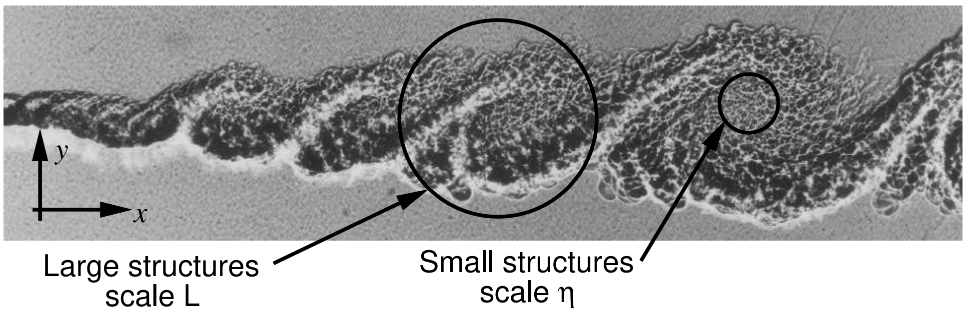

Figure 3.1: Visualization of the flow in a mixing layer (from Brown & Roshko 1974).

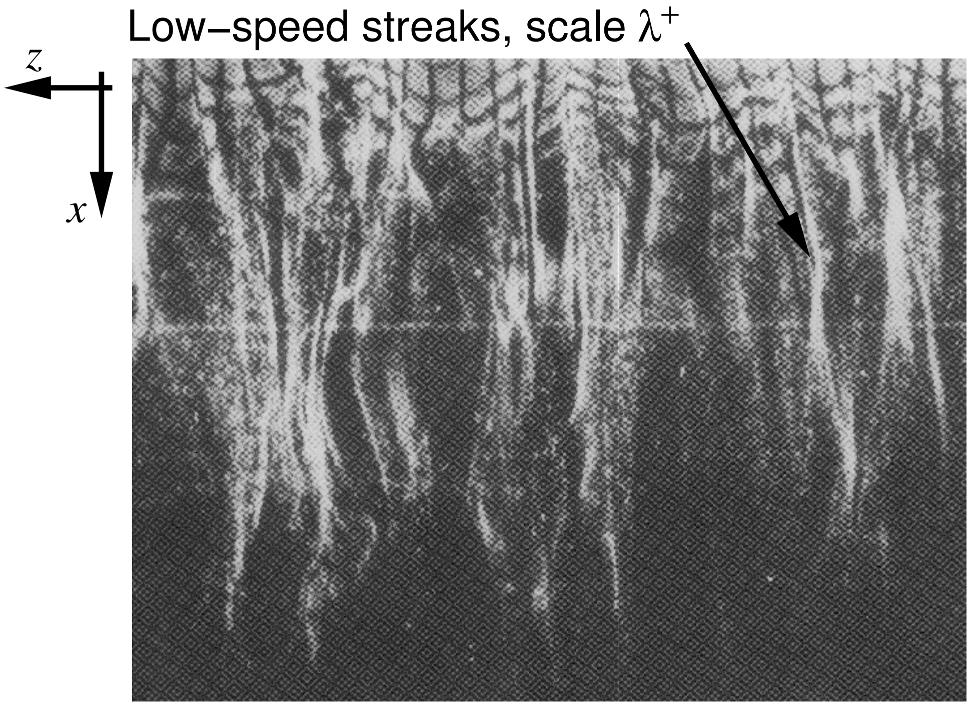

Figure 3.2: Visualization of the flow in a turbulent boundary layer (from Kline *et al.* 1967).

velocity, and τ_w is the viscous stress at the wall. In boundary layers or pipe flows, $u_\tau \sim UC_f^{1/2}$, and $C_f \sim Re^{-\alpha}$, where $C_f = 2\tau_w/\rho U^2$ is the skin-friction coefficient, U is an outer velocity scale of the flow (the free-stream velocity in a boundary layer, or the centerline velocity in a pipe) and $\alpha \simeq 0.2 - 0.25$. To maintain constant grid spacing in wall units, $\Delta x_i^+ = \Delta x_i u_\tau/\nu$, therefore, the required number of points in each direction is

$$N_i = \frac{L_i}{\Delta x_i} = \frac{L_i}{\Delta x_i^+ \nu/u_\tau} \sim \frac{L_i U Re^{-\alpha/2}}{\nu} \sim Re^{1-\alpha/2}, \tag{3.1}$$

and the total number of points is proportional at least to $Re^{2.6}$. The cost, from considerations similar to those made above, scales approximately like $Re^{3.5}$.

The landmark DNS of plane channel flow at $Re = 3\,300$ by Kim *et al.* (1987), for instance, used 2 million grid points, and required approximately 200 hours of CPU time on a Cray YMP. To increase the Reynolds number by a factor of 10, 800 million points would be necessary to resolve the flow, and approximately 600 000 CPU hours (almost seven years) would have been required on the YMP. Even with present supercomputers, that are faster by one or two orders of magnitude than the YMP, this computation would require a major effort.

3.1.2 Large-eddy simulation

In an LES only the large scales of motion must be resolved. The similarity of the small scales, which only transmit energy to smaller scales (energy cascade), and the fact that the dissipation is set by the large scales are exploited by SGS models, whose main purpose is to reproduce the energy transfer accurately, at least in a statistical sense. When the filter cutoff is in the inertial region of the spectrum, therefore, the resolution required by an LES is nearly independent of the Reynolds number.

The cost of an LES calculation, however, depends on the Reynolds number if a solid surface is present, since in that case even the largest scales of motion depend on the Reynolds number. Chapman (1979) estimated that the resolution required to resolve the outer layer of a growing boundary layer is proportional to $Re^{0.4}$, while for the viscous sublayer (which, in aeronautical applications, only accounts for approximately 1% of the boundary layer thickness) the number of points needed increases at least like $Re^{1.8}$. Thus, although LES can give some improvement over DNS, and be extended to flows at

Reynolds numbers at least one order of magnitude higher than DNS at a reasonable cost, its application to engineering flows remains expensive, unless approximate boundary conditions, or wall models, are used. This approach will be described in Section 7.2.

3.2 Time advancement

The choice of the time advancement method is usually determined by the requirements that numerical stability be assured, and that the turbulent motions be accurately resolved in time. Two stability limits apply to DNS and LES calculations. The first is the viscous condition, that requires that the time-step Δt be less than $\Delta t_v = \sigma \Delta y^2/\nu$ (where σ depends on the actual time advancement chosen). The CFL condition requires that Δt be less than $\Delta t_c = \mathrm{CFL}\Delta x/u$, where the maximum allowable Courant number CFL also depends on the numerical scheme used. Finally, the physical constraint requires Δt to be less than the time scale of the smallest resolved scale of motion, $\tau \sim \Delta x/U_c$ (where U_c is a convective velocity of the same order as the outer velocity).

In most flows, the viscous condition demands a much smaller time-step than the other two; for this reason, the diffusive terms of the governing equations are usually advanced using implicit schemes (typically, the second-order Crank-Nicolson scheme). Since, however, Δt_c and τ are of the same order of magnitude, the convective term can be advanced by explicit schemes such as the second-order Adams-Bashforth method, or third- or fourth-order Runge-Kutta schemes. In compressible flow calculations, or in unbounded flows in which the mesh must not be very fine near a solid surface, fully explicit schemes are often employed.

3.3 Spatial discretization

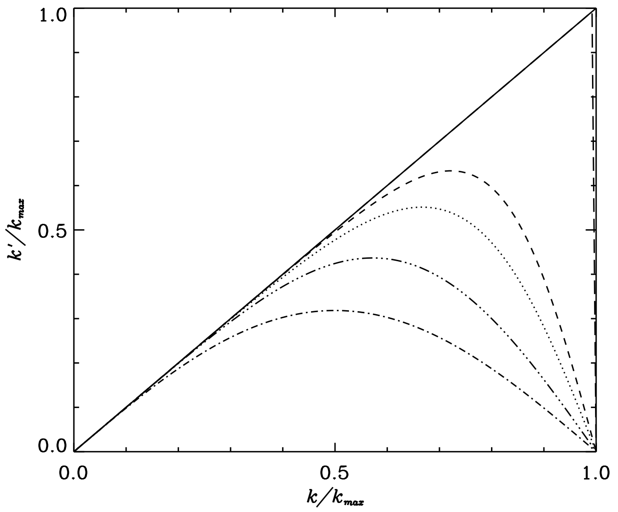

Figure 3.3: Modified wave-number for various differencing schemes. ——— Exact; —·— second-order central; —···— fourth-order compact; ········ fourth-order Padè; - - - sixth-order Padè; — — — spectral.

The analytical derivative of a complex exponential $f(x) = e^{ikx}$ is $f'(x) = ike^{ikx}$; if f is differentiated numerically, however, the result is

$$\frac{\delta f}{\delta x} = ik'e^{ikx}, \tag{3.2}$$

where k' is the "modified wave-number". A modified wave-number corresponds to each differencing scheme. Its real part represents the attenuation of the computed derivative compared to the actual one, whereas a non-zero imaginary part of k' indicates that phase errors are introduced by the numerical differentiation. Figure 3.3 shows the real part of the modified wave-numbers for various schemes. For a second-order centered scheme, for instance, $k' = k\sin(k\Delta x)/(k\Delta x)$. For small wave-numbers k the numerical derivative is quite accurate; high wave-number fluctuations, however, are resolved poorly. No phase errors, however, are introduced.

The need to resolve accurately high wave-number turbulent fluctuations implies that either low-order schemes are used on very fine meshes (such that, for the smallest scales that are physically important $k' \simeq k$), or that higher-order schemes are employed on coarser meshes. High-order schemes are more expensive, in terms of computational resources, than low-order ones, but the increase in accuracy they afford (for a given mesh) often justifies their use.

3.4 Conservation

It is particularly important, in direct and large-eddy simulations of transitional and turbulent flows, that the numerical scheme preserves the conservation properties of the Navier-Stokes equations. In the limit $Re \to \infty$, the Navier-Stokes equations conserve mass, momentum, energy and vorticity in the interior of the flow: the integral of these quantities over the computational domain can only be affected through the boundaries. Some numerical schemes, however, do not preserve this property. For instance, the convective term in the momentum equations can be cast in several ways:

$$\text{Advective form} \quad : \quad u_j \frac{\partial u_i}{\partial x_j}, \tag{3.3}$$

$$\text{Divergence form} \quad : \quad \frac{\partial}{\partial x_j}(u_i u_j), \tag{3.4}$$

$$\text{Rotational form} \quad : \quad \epsilon_{ijk} u_j \omega_k - \frac{\partial}{\partial x_i}(u_j u_j/2), \tag{3.5}$$

$$\text{Skew-symmetric form} \quad : \quad \frac{1}{2}\left[u_j \frac{\partial u_i}{\partial x_j} + \frac{\partial}{\partial x_j}(u_i u_j)\right]. \tag{3.6}$$

It is easy to show (Morinishi *et al.* 1998) that, if a typical co-located finite-difference scheme is used, the first form does not conserve either momentum or energy, the second conserves momentum but not energy, the others conserve both. If, on the other hand, a control-volume approach is used, the divergence form conserves energy but the pressure-gradient term does not. With a staggered grid and central differences the conservation properties of the Navier-Stokes equations.

Upwind schemes also have very undesirable effects on the conservation properties of the calculation, as does the explicit addition of artificial dissipation. It will be shown later in Chapter 6 that even mildly upwind-biased schemes result in a significant loss of accuracy. In incompressible flows, these type of methods are not suited to DNS and LES, and should be avoided.

3.5 Example of a numerical algorithm

One common technique used in DNS and LES calculations is the fractional time-step method (Chorin 1969, Kim & Moin 1985), in which first the Helmholtz equation is solved to obtain an estimate of the velocity field that does not satisfy mass conservation; the pressure is then computed by solving Poisson's equation, the estimated velocity field supplying the source term. If a pressure correction is applied, the resulting velocity will be a divergence-free solution of the Navier-Stokes equations. If the Navier-Stokes equations are written as

$$\frac{\partial u_i}{\partial t} = -\frac{\partial p}{\partial x_i} - H_i + \frac{1}{Re}\nabla^2 u_i, \tag{3.7}$$

where an appropriate length and velocity scale have been used to make the equations dimensionless, and H_i is the nonlinear terms, a typical time-advancement sequence using the Crank-Nicolson scheme for the viscous stresses and the second-order Adams-Bashforth method for the convective term would consist of the following steps:

1. Velocity prediction (Helmholtz equation):
$$v_j - u_j^n = -\Delta t\left(\frac{3}{2}H_j^n - \frac{1}{2}H_j^{n-1}\right) + \frac{\Delta t}{2Re}\left(\nabla^2 v_j + \nabla^2 u_j^n\right) \tag{3.8}$$
2. Poisson solution:
$$\nabla^2 \phi = \frac{1}{\Delta t}\frac{\partial v_j}{\partial x_j} \tag{3.9}$$
3. Velocity correction:
$$u_j^{n+1} = v_j - \Delta t \frac{\partial \phi}{\partial x_j}, \tag{3.10}$$

where v_j is the estimated velocity, and ϕ is the modified pressure, related to the actual pressure by $p = \phi - (\Delta t/2Re)\nabla^2\phi$. This time-advancement scheme is second-order-accurate in time.

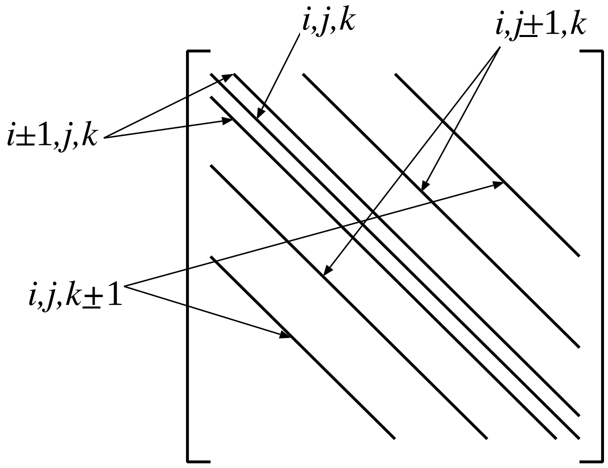

Figure 3.4: Matrix form for the central-difference discretization of the Helmholtz and Poisson equations.

The predictor step can be rewritten as

$$\left(1-\frac{\Delta t}{2Re}\nabla^2\right)v_j=-\Delta t\left(\frac{3}{2}H_j^n-\frac{1}{2}H_j^{n-1}\right)+\left(1+\frac{\Delta t}{2Re}\nabla^2\right)u_j^n. \tag{3.11}$$

The discretization of the differential operators results in a system of algebraic equations to be solved; the form of the matrix associated with the linear system depends on the discretization chosen. If central differences are used in all directions, for instance, the resulting matrix is banded hepta-diagonal (Fig. 3.4), and can be solved iteratively, or can be split into three tri-diagonal matrices that can be solved in sequence (Kim & Moin 1985).

The Poisson equation (3.9), on the other hand, results in a matrix that, although also of the form shown in Fig. 3.4, cannot, in general, be solved directly. Several techniques are commonly used, including multigrid methods, conjugate gradients and, for cases in which one or more directions of homogeneity exist, direct solvers.

Spectral methods, in which the velocity and pressure are expressed in terms of Fourier series in the directions of homogeneity of the flow, Chebychev or Legendre polynomials in the inhomogeneous directions, may allow decoupling of the equations. For a problem that is homogeneous in three directions, (the study of decaying or forced isotropic turbulence, for instance) the velocity can be written as

$$u_j(\mathbf{x},t)=\sum_{k_1=-N_1/2}^{N_1/2}\sum_{k_2=-N_2/2}^{N_2/2}\sum_{k_3=-N_3/2}^{N_3/2}\widehat{u}_j(\mathbf{k};t)e^{i\mathbf{k}\cdot\mathbf{x}}=\sum_{\mathbf{k}}\widehat{u}_j(\mathbf{k};t)e^{i\mathbf{k}\cdot\mathbf{x}} \tag{3.12}$$

where N_1, N_2 and N_3 are the number of grid points in the three directions, $\widehat{u}_i$ are the Fourier coefficients of the velocity[1] and $\mathbf{k}\equiv(k_1,k_2,k_3)^T$ is the vector wave-number. The Fourier expansion (3.12) can be differentiated term by term to yield

$$\nabla^2 u_j=\sum_{\mathbf{k}}\left(-k_1^2-k_2^2-k_3^2\right)\widehat{u}_je^{i\mathbf{k}\cdot\mathbf{x}}=-\sum_{\mathbf{k}}k^2\widehat{u}_je^{i\mathbf{k}\cdot\mathbf{x}}. \tag{3.13}$$

Taking the Fourier transform of (3.11), multiplying both sides by $\exp -i\mathbf{k}'\cdot\mathbf{x}$ and taking advantage of the orthogonality properties of the complex exponentials allows (3.8) to be replaced by a set of algebraic equation (one for each wave-number $\mathbf{k}$):

$$\left(1+k^2\frac{\Delta t}{2Re}\right)\widehat{v}_j=-\Delta t\left(\frac{3}{2}\widehat{H}_j^n-\frac{1}{2}\widehat{H}_j^{n-1}\right)+\left(1-k^2\frac{\Delta t}{2Re}\right)\widehat{u}_j^n, \tag{3.14}$$

[1]The constraint that u_i be real requires that $\widehat{u}_i(\mathbf{k})=\widehat{u}_i^*(-\mathbf{k})$, where $\widehat{u}_i^*$ is the complex conjugate of $\widehat{u}_i$.

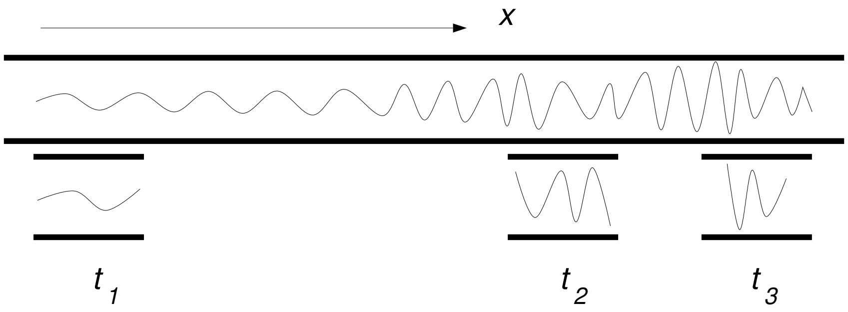

Figure 3.5: Evolution of perturbations in a channel: spatial *vs.* temporal development.

(where $k^2 = k_1^2 + k_2^2 + k_3^2$), that can be solved very easily, since each wave-number component $\widehat{v}(\mathbf{k})$ is decoupled from all the others. The Poisson equation can be treated similarly to yield

$$-k^2 \widehat{\phi} = -\frac{ik_j \widehat{v}_j}{\Delta t}, \tag{3.15}$$

while the velocity correction gives:

$$\widehat{u}_j^{n+1} = \widehat{v}_j - i\Delta t k_j \widehat{\phi}; \tag{3.16}$$

equations (3.15) and (3.16) can also be solved directly. More information on spectral methods in fluid dynamics can be found in the book by Canuto *et al.* (1988).

3.6 Boundary conditions

3.6.1 Periodic conditions

Many flows that have been studied by DNS and LES have one or more directions of homogeneity, that allow the application of periodic boundary conditions. Periodic boundary conditions imply that the computational domain repeats itself an infinite number of times. Periodic boundary conditions are convenient, since they eliminate the need to specify inflow and outflow conditions, easy to implement (in fact they are applied implicitly by Fourier methods) and efficient, since they allow use of small computational domains.

The use of periodic boundary conditions is similar to studying the time development, rather than the spatial development, of a flow; if one looks at the spatial evolution of a perturbation in plane channel (Fig. 3.5), for instance, the use of periodic boundary conditions is equivalent to studying the flow in a convecting frame of reference. Each flow realization (*i.e.*, each time-step) is equivalent to one location in the spatially developing framework. When periodic boundary conditions are used, the computational domain must be at least as long as the wavelength of the longest structure present in the flow. If such wavelength is not known *a priori*, the two-point correlations must be examined to determine whether the domain length is sufficient.

For self-similar flows, one can solve the governing equations in the self-similar coordinate frame and still apply periodic boundary conditions. Spalart performed DNS of sink flow (Spalart 1986) and flat-plate (Spalart 1988) boundary layers using this approach. Spalart also used periodic conditions to study a boundary layer in the presence of favorable, then adverse pressure gradient (which is not self-similar) by introducing the "fringe method" (Spalart & Watmuff 1993). This technique consists in adding forcing terms to the Navier-Stokes equations in small regions near the inflow and outflow of the domain to remove mass and decrease the boundary layer thickness, prior to re-introducing it at the inflow. Although this method can be effective for the simulation of equilibrium boundary layers, and in some non-equilibrium cases (Liu *et al.* 1996), its general applicability is limited, since the streamwise extent of the computational box should be increased substantially to allow the flow to return to equilibrium as it approaches the outflow boundary.

3.6.2 Inflow and outflow conditions

Despite the attempts to use periodic boundary conditions in flows that are not homogeneous in space, the specification of inflow and outflow conditions is required in many cases. Several studies have focused on the outflow conditions; at present it appears that the use of a buffer domain (Streett & Macaraeg 1989) in which the equations are parabolized, of convective boundary conditions (Orlansky 1976), or a combination of the two techniques, can give adequate results in most flows of interest.

The specification of the inflow conditions can, however, be more problematic, since the flow variables on the entire inflow plane must be specified as a function of time. To study transitional flows, perturbations can be superposed on a laminar mean flow. This approach has been used successfully in boundary layers (Rai & Moin 1993, Ducros *et al.* 1996, Huai *et al.* 1997) and mixing layers (Comte *et al.* 1998). If, however, one is interested in turbulent flows, the development of turbulence from perturbed boundary conditions may require excessively long streamwise domains, since turbulence must be allowed to develop from the imposed perturbation. Another option is to assign a mean velocity profile, upon which random noise perturbations are superimposed, with their phases adjusted to yield the desired moments. Lee *et al.* (1992) used this technique in a DNS of isotropic compressible turbulence; they found that the flow recovers fairly quickly (in about two integral length scales) from the random fluctuations. The method, however, appears to be less well suited to wall-bounded flows. Le *et al.* (1997) and Akselvoll & Moin (1996) found that several boundary-layer thicknesses (10δ and 25δ, respectively) were needed for reasonable statistics to be established before the region of interest in backward facing step computations. Similar results were reported by Lund *et al.* (1998) in their zero-pressure-gradient boundary-layer LES. In addition to the waste of computational resources due to large recovery lengths, control of the skin friction and integral thickness just upstream of the domain of interest is difficult; the development section is unphysical and the upstream conditions do not always lead to the desired statistics downstream.

Lund *et al.* (1998) proposed a method that also requires self-similarity, but has proven to be more flexible than any of the others used so far: it involves rescaling the velocity field at some downstream location, in a flat-plate boundary layer, and re-introducing it at the inflow. An advantage of this method is that it allows the calculation of non-equilibrium flows, as long as a flat-plate of sufficient length is appended before the region of interest. A large region of the flow (and substantial computational resources) are, however, used only to generate a realistic inflow condition.

The use of the results of a separate calculation may be the most realistic type of inflow condition available, since the development section can be drastically reduced or in some cases eliminated altogether. The auxiliary calculation must be run synchronously with or prior to the actual computation, and a time series of data stored on disk is used as inflow. Using this approach, several computations of spatially developing flows have been conducted successfully (Kaltenbach *et al.* 1999). In high-Reynolds number flows, however, the number of points in the inflow plane increases dramatically and the cost of the auxiliary computation may become significant from the storage and the CPU time point of view.

3.6.3 Wall boundary conditions

At solid walls, the momentum flux must be known. Since the wall velocity is assigned, the no-slip condition allows the determination of the convective part $u_i u_j$ of the momentum flux at the wall. Differentiation of the velocity profile to determine the viscous stress, however, is accurate only if the wall-layer is well-resolved. To represent accurately the structures in the near-wall region, the first grid point must be located at $y^+ < 1$, and the grid spacing must be of order $\Delta x^+ \simeq 15$, $\Delta z^+ \simeq 5$ ($\Delta x^+ \simeq 50 - 150$, $\Delta z^+ \simeq 15 - 40$ for LES). As $Re \to \infty$, an increasing number of grid points must be used to resolve a layer of decreasing thickness. This may also result in high aspect-ratio cells, with subsequent degradation of the numerical accuracy.

Alternatively, approximate boundary conditions, or wall models, may be used in LES. When the grid is not fine enough to resolve the near-wall gradients,the wall layer must be modeled by specifying a correlation between the velocity in the outer flow and the stress at the wall. This approach allows the first grid point to be located at $y^+ \simeq 30 - 150$, and, since the energy-producing vortical structures in the wall-layer do not have to be resolved, it permits the use of coarser meshes in the other directions as well: $\Delta x^+ \simeq 100 - 600$, $\Delta z^+ \simeq 100 - 300$, but the modeling of the wall-layer physics introduces further empiricism in the calculations. Some remarks on wall models will be made in Section 7.2.

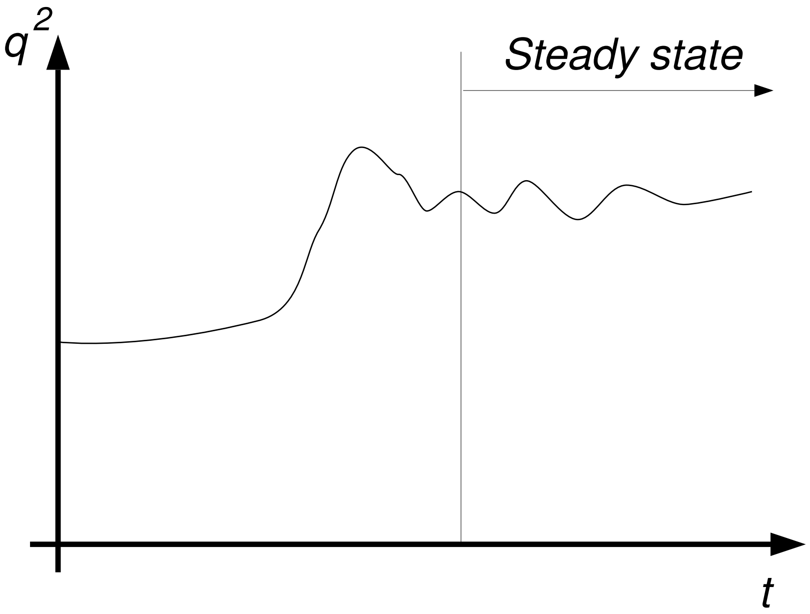

Figure 3.6: Time history in a typical time-developing calculation.

3.7 Initial conditions

For flows that are statistically steady the initial conditions are relatively unimportant; they may consist of large-amplitude perturbations superposed on a realistic mean flow, or of a fully-developed flow in a similar configuration. Typically, the flow is allowed to develop in time until a steady state is reached, and then statistics are accumulated (Figure 3.6).

For flows in which the transient is important (temporal transition, the decay of homogeneous isotropic turbulence, etc.), more care should be used when assigning the initial conditions. In problems involving laminar-turbulent transition, controlled or random perturbations can be used. For turbulent flow problems, on the other hand, assigning random noise with a given spectrum requires some adjustment time before the nonlinear interactions become realistic.

Chapter 4

APPLICATIONS OF DNS

4.1 The role of direct simulations

Direct numerical simulations supply the time-dependent velocity field at multiple locations in the flow, yielding a wealth of information from which single- and multi-point statistics can be calculated, even for quantities (such as the pressure or the vorticity) that are difficult to measure experimentally. This important feature of DNS has been exploited in several investigations that applied DNS to transitional and turbulent flows, and have contributed significantly to the understanding of the turbulence physics, and to the improvement of lower-level models. Moin and Mahesh (1998) present a recent review of the achievements of DNS. Only a brief summary of the principal ones follows.

4.2 Model validation

Since DNS allows the computation of all terms in the Reynolds stress balance equations, DNS data can be used for the direct evaluation of RANS models. While experimental data usually allow only the evaluation of the effect of the entire model, by comparing some measurable quantity such as the velocity profile, skin friction or pressure coefficient, DNS data allows the direct comparison of each term of the model.

Bardina *et al.* (1985), for instance, studied the effect of rotation on turbulence, and determined that an additional term should be used in turbulence models to account for the rotation effects correctly. Mansour *et al.* (1988) used data from the simulation of plane channel flow by Kim *et al.* (1987) to study the dissipation budget in wall-bounded flows, and were able to examine in detail the asymptotic behavior of the budget terms. Rogers *et al.* (1989) used DNS data to develop improved models of passive scalar transport.

DNS data has also been extremely valuable to study the physics of the subgrid-scale stresses, and devise improved models. This is achieved by filtering the DNS data to compute explicitly the SGS stresses, as well as other important terms (*a priori* test) . Until very recently, multi-point experimental data that could be filtered in such a way was not available. *A priori* tests have been very valuable in understanding the mechanisms that govern the energy transfer between the resolved and unresolved scales of motion (Piomelli *et al.* 1988, Domaradzki *et al.* 1994, or Piomelli *et al.* 1996).

4.3 Turbulence structure

Perhaps the most significant contribution of DNS to date has been the identification and eduction of turbulent structures. Since DNS supplies the velocity and its gradients at each point in space and time, it allows the investigation of the relationship between the vortical structures and the energy and Reynolds stress production (Robinson 1991a, 1991b).

Several methods can be used to visualize the coherent eddies in a turbulent flow. Robinson (1991b) compared various techniques, and found that the pressure is effective in identifying the regions of strong rotation in vortex cores. Hunt *et al.* (1988) proposed the use of the second invariant of the velocity-gradient tensor,

$$Q = -\frac{1}{2}\frac{\partial u_i}{\partial x_j}\frac{\partial u_j}{\partial x_i} = -\frac{1}{2}\left(S_{ij}S_{ij} - \Omega_{ij}\Omega_{ij}\right), \tag{4.1}$$

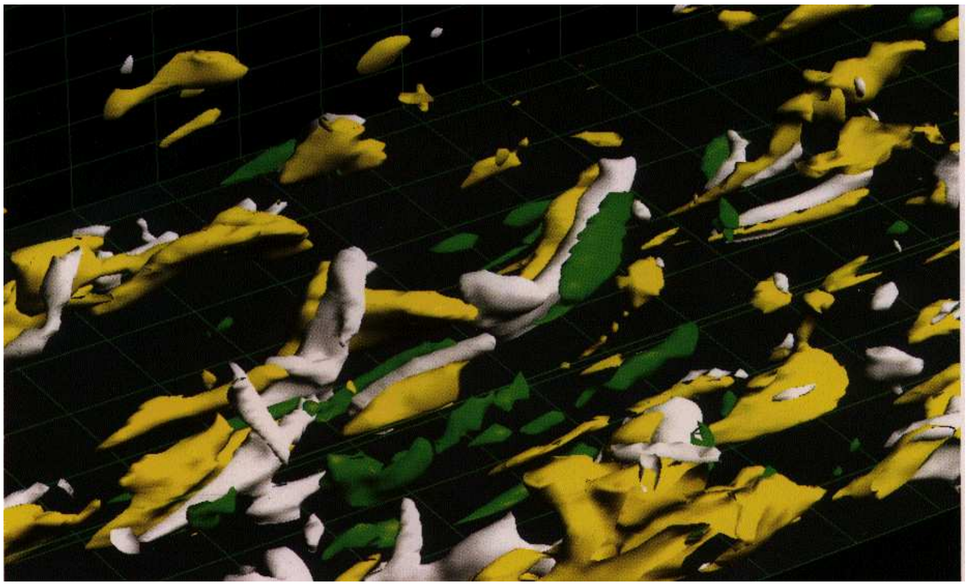

Figure 4.1: Ejections (in yellow), sweeps (in green) accompanied by vortical structures (in white). Turbulent plane channel flow, $Re_\tau = 180$. Reproduced with permission from N. Kasagi.

where S_{ij} and Ω_{ij} are, respectively, the strain-rate and rotation tensors, that is, the symmetric and anti-symmetric parts of the velocity-gradient tensor; in regions where $Q > 0$ the vorticity is significant, and is due to rotation rather than to shear.

In Fig. 4.1 the pressure is used to visualize the coherent eddies in fully developed turbulent channel flow at $Re_\tau = u_\tau \delta/\nu = 180$ (where δ is the channel half-width, and u_τ, the friction velocity, was defined in Chap. 3). This figure shows how the regions of significant Reynolds shear stress occur in close proximity of the quasi-streamwise vortical structures, highlighted by showing the low-pressure regions associated with the vortex cores (regions where $p^+ < -3$). The ejections (regions in which $u' < 0$, $v' > 0$, and $u^{+\prime} v^{+\prime} < -3$), occur on the up-wash side of the vortex, whereas the sweeps (regions in which $u' > 0$, $v' < 0$, and $u^{+\prime} v^{+\prime} < -3$) on the down-wash side.

Figure 4.2 highlights the relationship between the sweeps (regions of high-speed fluid moving towards the wall), the quasi-streamwise vortices, and the regions of large $u'v'$. Around $z^+ = 150$, for example, several quasi-streamwise vortical structures can be observed; very close to these structures, regions of high Reynolds shear stress are located.

4.4 Drag reduction and turbulence control

More recently, DNS have been used to study strategies to control turbulence, both passive and active. Choi *et al.* (1993) performed the simulation of the flow over a grooved surface (a riblet wall) using a second-order-accurate finite-difference method in generalized coordinates. Riblets had been studied experimentally (Walsh 1980, and others), and had been found to produce net drag reduction of up to 8% when the groove spacing was less than 25 wall units, even though the surface exposed to the flow was increased. Despite the experimental studies, the mechanisms by which the riblets reduce drag were not yet understood well. Four configurations were studied, with riblet angles of 45 and 60 degrees, and groove spacings of 20 and 40 wall units. Consistent with the experimental studies, the lower spacing yielded drag reduction of 5 or 6%, while the higher spacing gave rise to a drag increase varying between 2 and 12%, values in excellent agreement with the experiments. The mean flow was found to remain uniform in the spanwise direction, except very near the riblets. The wall shear was substantially reduced over most of the riblet surface; only near the riblet tip the wall shear was larger than on the flat wall.

Figure 4.3a shows contours of the instantaneous wall shear. In the $s^+ = 20$ case regions of high wall shear only occur near the riblet tip, whereas in the drag-increasing case they occur in the groove as well; these regions of high shear are often associated, in wall-bounded flows, with the down-wash of strong

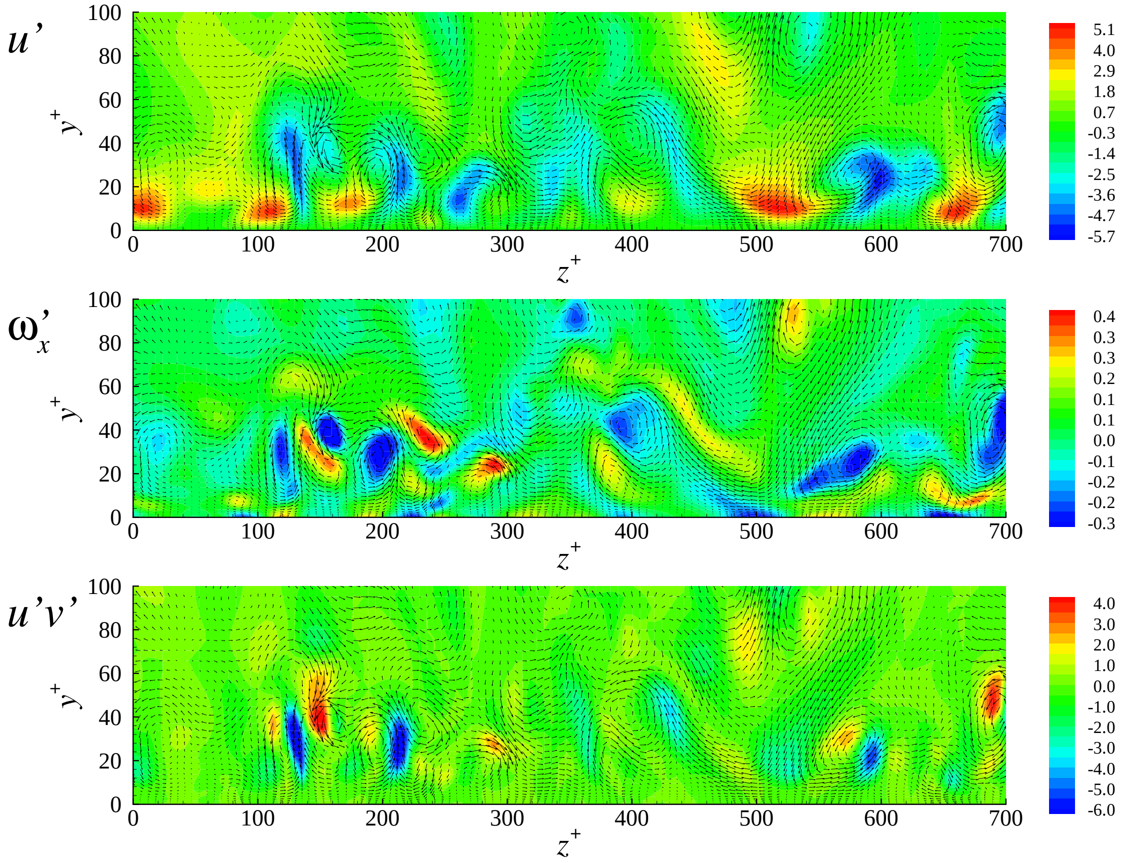

Figure 4.2: Velocity, vorticity, Reynolds stress contours and secondary $(v - w)$ velocity vectors in a cross-plane. Turbulent plane channel flow, $Re_\tau = 180$.

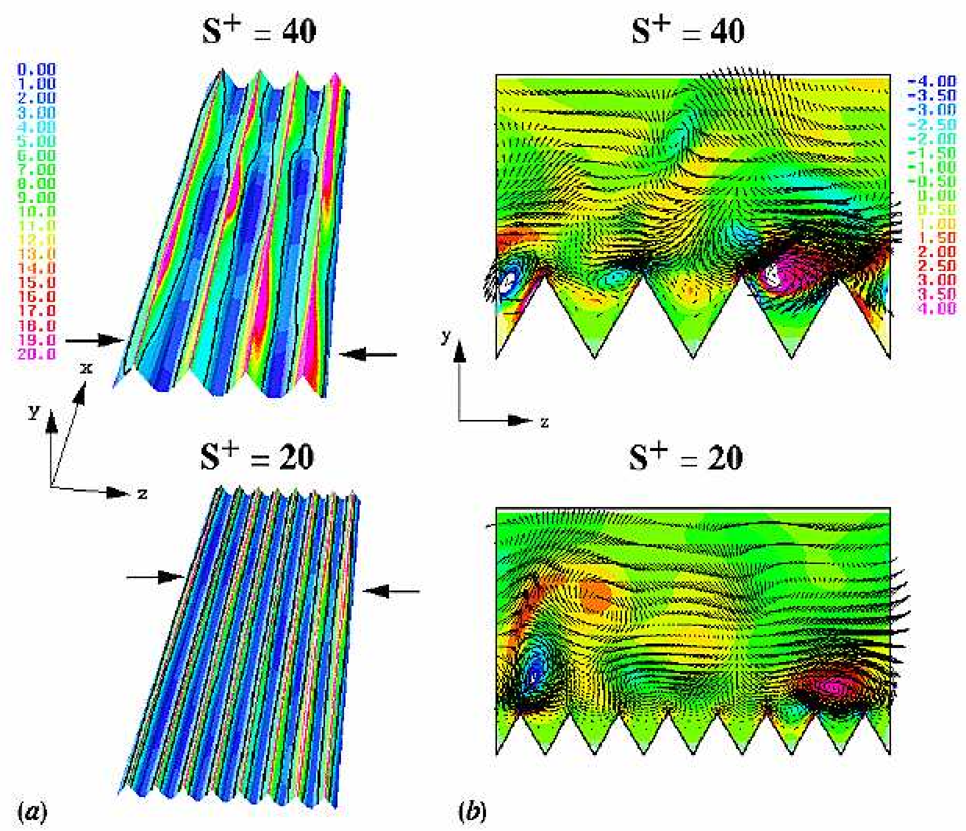

Figure 4.3: Instantaneous flow over the riblets with $\alpha = 60^o$. (a) contours of the wall-shear on the riblet surface; (b) cross-flow velocity vectors and contours of the streamwise vorticity in the $yz-$plane. Reproduced with permission from Choi *et al.* (1993).

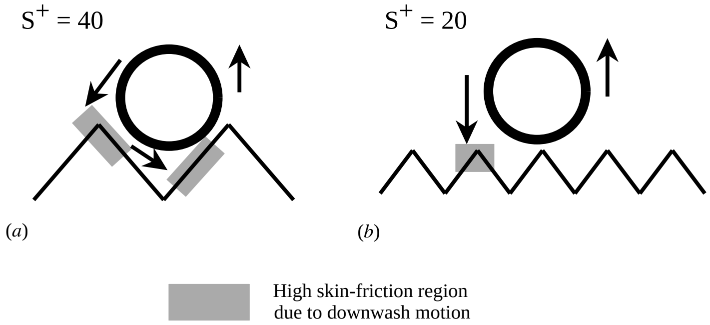

Figure 4.4: Schematic diagram of drag increase and reduction mechanisms by riblets. (a) $s^+ = 40$; (b) $s^+ = 20$. Reproduced with permission from Choi *et al.* (1993).

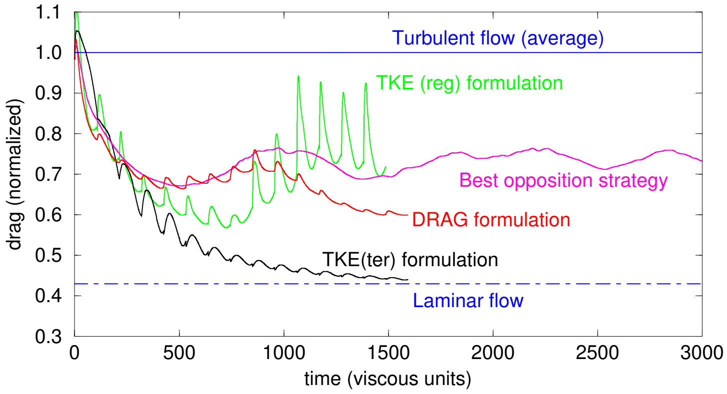

Figure 4.5: Performance of optimized control for different control strategies as computed in direct numerical simulations of turbulent channel flow at $Re_\tau = 100$. The optimization horizon was $T^+ = 100$.

streamwise vortices. The cross-flow velocity contours shown in Fig. 4.3b show this phenomenon very clearly. They also show how the streamwise vortices, whose average diameter is approximately 30 wall units (Kim *et al.* 1987) are more likely to be found inside the groove in the $s^+ = 40$ case than in the $s^+ = 20$ configuration. When the vortices move into the riblet valley (Fig. 4.4), a larger area is exposed to the down-wash of the vortices, resulting in the increase in the average friction coefficient. Conversely, when the spacing is smaller than the average vortex diameter, the vortices are forced to reside above the riblet tips, which results in the thickening of the viscous sublayer, and in a smaller region near the tip being exposed to the down-wash.

Active control strategies have also been explored by DNS (see, for example, the recent review by Lumley & Blossey 1999). Choi *et al.* (1994) applied "opposition control" in channel flow at $Re_\tau = 100$. By applying suction and blowing at the wall to oppose the vertical motion of the fluid some distance away from the wall, they obtained drag reduction up to 25%. Hammond *et al.* (1998), in calculations performed at $Re_\tau = 180$, observed that the opposition control is effective if the detection point is quite close to the wall (a distance of 15 wall units was found to be optimal). If the detection point is too far from the wall, the fluid particle may meander away from the point where the blowing is applied, possibly ending near a point in which suction is applied. This results in an undesirable increase of the turbulence levels.

Bewley *et al.* (2000) applied optimal control theory to reduce drag in turbulent channel flow at $Re_\tau = 100$ and 180. In their approach a cost functional was minimized over a certain time interval, the "horizon". Typical cost functionals involved the drag, the turbulent kinetic energy, the enstrophy or the terminal value of the turbulent kinetic energy. The cost minimization required solution of the adjoint Navier-Stokes operator. They showed that, for long enough horizons, the performance of the optimal control far exceeded the best that could be obtained with opposition control. Figure 4.5 shows the drag history in the plane channel when various control strategies were employed. The best control strategy was the one involving "terminal control" of the turbulent kinetic energy, *i.e.*, one in which the final value of the turbulent kinetic energy (rather than the instantaneous one) was minimized. This approach allows the cost functional to increase within the optimization horizon, but leads to more substantial reduction of the turbulence level at the end the horizon, as shown in the Figure. The flow, when this type of control was applied, became laminar; similar results were obtained at $Re_\tau = 180$. Although the control algorithm was computationally very expensive, to the point of being infeasible in practical application, it was extremely useful in supplying a target, as well as in illustrating how control strategies affect the Reynolds-stress and energy-carrying coherent structures.

Chapter 5

SUBGRID-SCALE MODELING

5.1 Energy transfer mechanisms

In large-eddy simulations, the dissipative scales of motion are resolved poorly, or not at all. The main role of the subgrid-scale model must be, therefore, to remove energy from the resolved scales, mimicking the drain that is usually associated with the energy cascade. Thus, it is not necessary for a model to represent the "exact" SGS stresses accurately at each point in space and time, but only to account for their global effect. To understand the interaction between resolved and unresolved scales better, consider the transport equations for $\overline{q}^2 = \overline{u}_i\overline{u}_i$, twice the total resolved energy (mean and fluctuating), and $q^2_{sgs} = \tau_{kk}$, twice the subgrid-scale kinetic energy:

$$\begin{aligned}
\frac{\partial \overline{q}^2}{\partial t} + \underbrace{\frac{\partial}{\partial x_j}(\overline{q}^2\overline{u}_j)}_{\text{Advection of } \overline{q}^2} = &-2\underbrace{\frac{\partial}{\partial x_j}(\overline{p}\,\overline{u}_j)}_{\text{Press. Diff. of } \overline{q}^2} + \underbrace{\frac{\partial}{\partial x_j}\left(\nu\frac{\partial \overline{q}^2}{\partial x_j}\right)}_{\text{Visc. Diff. of } \overline{q}^2} \\
&-2\underbrace{\frac{\partial}{\partial x_j}(\tau_{ij}\overline{u}_i)}_{\text{SGS Diff.}} -2\underbrace{\nu\frac{\partial \overline{u}_i}{\partial x_j}\frac{\partial \overline{u}_i}{\partial x_j}}_{\text{Visc. Diss. of } \overline{q}^2} +2\underbrace{\tau_{ij}\overline{S}_{ij}}_{\text{SGS Diss.}}
\end{aligned} \tag{5.1}$$

$$\begin{aligned}
\frac{\partial q^2_{sgs}}{\partial t} + \underbrace{\frac{\partial}{\partial x_j}(q^2_{sgs}\overline{u}_j)}_{\text{Advection of } q^2_{sgs}} = &-\underbrace{\frac{\partial}{\partial x_j}(\overline{u_iu_iu_j} - \overline{u_iu_i}\,\overline{u}_j)}_{\text{Turb. Transport}} -2\underbrace{\frac{\partial}{\partial x_j}(\overline{pu_j} - \overline{p}\,\overline{u}_j)}_{\text{Press. Diff. of } q^2_{sgs}} \\
&+\underbrace{\frac{\partial}{\partial x_j}\left(\nu\frac{\partial q^2_{sgs}}{\partial x_j}\right)}_{\text{Visc. Diff. of } q^2_{sgs}} +2\underbrace{\frac{\partial}{\partial x_j}(\tau_{ij}\overline{u}_i)}_{\text{SGS Diff.}} \\
&-2\underbrace{\nu\left(\overline{\frac{\partial u_i}{\partial x_j}\frac{\partial u_i}{\partial x_j}} - \frac{\partial \overline{u}_i}{\partial x_j}\frac{\partial \overline{u}_i}{\partial x_j}\right)}_{\text{Visc. Diss. of } q^2_{sgs}} -2\underbrace{\tau_{ij}\overline{S}_{ij}}_{\text{SGS Diss.}} .
\end{aligned} \tag{5.2}$$

The equations above show that the resolved scales in a control volume (a grid cell, for example), exchange energy with the unresolved scales and the surroundings through several mechanisms. The advection and diffusion terms do not create or destroy resolved energy but only redistribute it between adjoining volumes. The last two terms in (5.1) represent respectively the resolved energy lost by viscous dissipation at the resolved-scale level, and the net energy exchange between the resolved and unresolved scales. Although the subgrid-scale dissipation $\varepsilon_{sgs} = \tau_{ij}\overline{S}_{ij}$ can be positive or negative, on the average energy flows from the large to the small scales, and $\varepsilon_{sgs} < 0$ (forward scatter); backscatter occurs when the energy flow is reversed ($\varepsilon_{sgs} > 0$). The total transfer of energy between large and subgrid scales is the SGS transfer, sum of SGS diffusion and dissipation.

The energy exchange mechanisms for the subgrid scales are similar; the advection and diffusion terms are again redistribution terms. The energy lost by the resolved scales to the subgrid ones appears as a source term in the transport equation for q_{sgs}^2: the SGS diffusion and dissipation have opposite signs in (5.1) and (5.2). It is important to point out the difference between the viscous and SGS dissipation terms. The SGS dissipation ε_{sgs} represents an energy interchange between resolved and unresolved scales, and is generally a dissipative term in the equation for $\overline{q}^2$ and, conversely, a production term in the equation for q_{sgs}^2. The viscous dissipation terms, on the other hand, represent a net loss, the resolved or SGS energy dissipated by the viscous forces.

5.2 Eddy viscosity models

Most subgrid scale models in use presently are eddy-viscosity models of the form

$$\tau_{ij} - \frac{\delta_{ij}}{3}\tau_{kk} = -2\nu_T \overline{S}_{ij}, \tag{5.3}$$

that relate the subgrid-scale stresses τ_{ij} to the large-scale strain-rate tensor $\overline{S}_{ij}$. In most cases, the eddy viscosity ν_T is obtained algebraically to avoid solving additional equations that would increase the cost of an already expensive calculation. Moreover, since the small scales tend to be more homogeneous and isotropic than the large ones, it is hoped that even simple, algebraic models can describe their physics accurately. Finally, since the SGS stresses only account for a fraction of the total stresses, modeling errors should not affect the overall accuracy of the results as much as in the standard turbulence modeling approach.

The eddy viscosity is, by dimensional analysis, the product of a length scale, ℓ, and a velocity scale, q_{sgs}. Since the most active of the unresolved scales are those closest to the cutoff, the natural length scale in LES modeling is the filter width, which is the size of the smallest structure in the flow, and is proportional to the grid size. The velocity scale is usually taken to be the square-root of the trace of the SGS stress tensor, $q_{sgs}^2 = \tau_{kk}$. Although in some cases a transport equation is solved to determine q_{sgs}^2, in most cases the equilibrium assumption is made to simplify the problem further and obtain an algebraic model for the eddy viscosity.

The equilibrium assumption is based on the consideration that the small scales of motion have shorter time scales than the large, energy-carrying eddies; thus, it can be hypothesized that they adjust more rapidly than the large scales to perturbations, and recover equilibrium nearly instantaneously. Under this assumption, the transport equation for q_{sgs}^2, (5.2) simplifies significantly, since all terms drop out, except the production term, $\varepsilon_{sgs} = \tau_{ij}\overline{S}_{ij}$, and the viscous dissipation of SGS energy, ε_v, to yield:

$$-\tau_{ij}\overline{S}_{ij} = \varepsilon_v. \tag{5.4}$$

The equilibrium assumption implies inertial range dynamics: energy is generated at the large-scale level, and transmitted to smaller and smaller scales, where the viscous dissipation takes place. Piomelli *et al.* (1997) carried out a study of the subgrid-scale (SGS) stresses in non-equilibrium, wall-bounded flows. Their findings indicate that the SGS stresses react to the imposition of the perturbation more rapidly than the large-scale ones, although not instantaneously.

5.3 Smagorinsky model

The Smagorinsky model (1963) is, from an historical point of view, the progenitor of all subgrid-scale stress models. It is based on the equilibrium hypothesis (5.4). If the viscous dissipation is modeled as $\varepsilon_v \sim q_{sgs}^3/\ell$, and (5.3) is substituted into (5.4) with $\nu_T \sim \ell q_{sgs}$, one obtains $q_{sgs} \sim \ell|\overline{S}|$, where $|\overline{S}| = (2\overline{S}_{ij}\overline{S}_{ij})^{1/2}$ is the magnitude of the strain-rate tensor. Letting $\ell \sim \overline{\Delta}$, the eddy viscosity can be written as

$$\nu_T = (C_s\overline{\Delta})^2|\overline{S}|. \tag{5.5}$$

Since the constant C_s (the Smagorinsky constant) is real, the model is absolutely dissipative: $\varepsilon_{sgs} = -(C_s\overline{\Delta})^2|\overline{S}|^3 \le 0$.

To evaluate C_s, Lilly (1967) assumed the existence of an inertial-range spectrum $E(k) = \mathrm{Ko}\,\varepsilon^{2/3}k^{-5/3}$, where k is the wavenumber, Ko the Kolmogorov constant, and ε the total viscous dissipation (due to both resolved and subgrid scales) which was assumed to be approximately equal to ε_v. Then $|\overline{S}|$ can be evaluated approximately by integrating the dissipation spectrum over all resolved wave-numbers

$$|\overline{S}|^2 \simeq 2\int_0^{\pi/\overline{\Delta}} k^2 E(k)dk = 2\mathrm{Ko}\,\varepsilon^{2/3}\int_0^{\pi/\overline{\Delta}} k^{1/3}dk = \frac{3}{2}\mathrm{Ko}\,\varepsilon^{2/3}\left(\frac{\pi}{\overline{\Delta}}\right)^{4/3}. \tag{5.6}$$

With Ko = 1.41, this gives

$$C_s \simeq \frac{1}{\pi}\left(\frac{2}{3\mathrm{Ko}}\right)^{3/4} = 0.18. \tag{5.7}$$

It was, however found by Deardorff (1970), and subsequently confirmed in *a priori* tests by McMillan *et al.* (1980), that in the presence of shear the coefficient must be reduced (values of the order of $C_s \simeq 0.065 - 0.1$ are commonly used).

For grids that are uniform in all directions, the filter width is proportional to the grid size in any direction (typically, $\overline{\Delta} = 2\Delta x$). When the grid is inhomogeneous, it is common to use an average filter width given by $\overline{\Delta} = 2(\Delta x \Delta y \Delta z)^{1//3}$. Furthermore, in the presence of solid boundaries the length scale needs to be modified by the introduction of Van Driest (1956) damping to account for the reduced growth of the small scales near the wall; the model is then recast in the form:

$$\nu_T = \left[C_s\overline{\Delta}\left(1 - e^{-y^+/25}\right)\right]^2 |\overline{S}|. \tag{5.8}$$

To reduce the SGS stresses during laminar-turbulent transition an intermittency factor was used by Piomelli *et al.* (1990), while Voke & Yang (1995) developed a low-Reynolds number correction and used only the fluctuating strain-rate tensor in (5.8).

5.4 Two-point closures

Two-point closures have been an alternative way to derive SGS models. Kraichnan (1976), using a two-point closure model for isotropic turbulence, computed the energy transfer from the resolved to the unresolved scales, $T_{sub}(k|k_m)$, given a cutoff wave-number k_m lying in an infinite inertial subrange. He then defined the net eddy-viscosity from the calculated subgrid-scale transfer:

$$\nu_e(k|k_m) = -\frac{T_{sub}(k|k_m)}{2k^2E(k)}. \tag{5.9}$$

For k_m lying in the inertial subrange, the net eddy viscosity approaches a k-independent eddy viscosity for $k << k_m$. Near k_m, however, both a negative and a positive contribution are significant; the negative part corresponds to energy transfer from the small to the large scales (backscatter, or eddy noise). The net eddy viscosity increases with increasing k/k_m to a finite cusp at $k/k_m = 1$.

Chollet & Lesieur (1981) used the Eddy-Damped, Quasi-Normal Markovian (EDQNM) theory to develop a SGS model with similar results. The Chollet-Lesieur (1981) model uses $[k_mE(k_m)]^{1/2}$ as velocity scale, and k_m^{-1} as length scale for the eddy viscosity, which, in wave space, is given by

$$\widehat{\nu}_T(k) = \widehat{\nu}_T^+(k/k_m)\,[E(k_m)/k_m]^{1/2}\,; \tag{5.10}$$

$\widehat{\nu}_T^+(k/k_m)$ can be approximated by (Chollet 1984)

$$\nu_e^+(k/k_m) = \mathrm{Ko}^{-\frac{3}{2}}\left[0.441 + 15.2\exp\left(-3.03k_m/k\right)\right], \tag{5.11}$$

where the value of the Kolmogorov constant was chosen to be Ko = 1.4. The Chollet parameterization of the dimensionless eddy viscosity is shown in Fig. 5.1. The eddy viscosity goes to a k-independent constant for $k/k_m << 1$, and rises to a finite cusp at $k/k_m = 1$.

The Chollet-Lesieur model produces zero eddy viscosity as long as there is no energy near the cutoff; it is, however, defined in wave space, which hampers its extension to finite-difference schemes and to complex geometries. To overcome this shortcoming, Métais & Lesieur (1992) derived the "structure function model." Assuming a cutoff wave number in the inertial region of a Kolmogorov spectrum, they

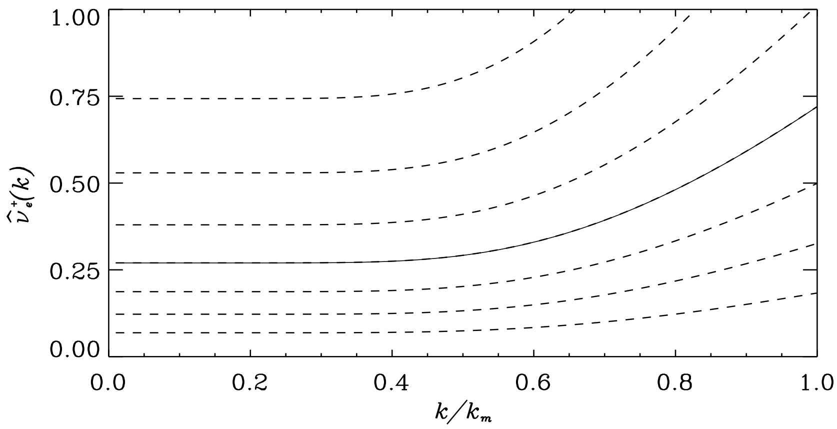

Figure 5.1: Non-dimensional spectral eddy viscosity as parameterized by Chollet (1984) and Métais & Lesieur (1992) for turbulence obeying a k^{-m} spectrum. The lines correspond to $m = 8/3$ (lowest) through $m = 2/3$ (highest); a solid line denotes a Kolmogorov spectrum ($m = 5/3$).

expressed the energy spectrum at the cutoff, $E(k_m)$, in terms of the resolved-scale second-order velocity structure function,

$$\overline{F_2}(\mathbf{x};\overline{\Delta}) = \langle [\overline{u}_i(\mathbf{x}+\mathbf{r}) - \overline{u}_i(\mathbf{x})]\,[\overline{u}_i(\mathbf{x}+\mathbf{r}) - \overline{u}_i(\mathbf{x})]\rangle, \tag{5.12}$$

where $\langle\cdot\rangle$ is an ensemble-average taken over all points such that $|\mathbf{r}| = \overline{\Delta}$, and obtained

$$\nu_T(\mathbf{x}) = 0.063\overline{\Delta}\left[\overline{F}_2(\mathbf{x};\overline{\Delta})\right]^{1/2}. \tag{5.13}$$

It must be remarked that, if an isotropic grid is used, the structure function can be seen as a finite difference approximation of the velocity gradient tensor:

$$\overline{F}_2 \simeq 2\overline{\Delta}^2 \frac{\partial \overline{u}_i}{\partial x_j}\frac{\partial \overline{u}_i}{\partial x_j} = 2\overline{\Delta}^2\left(\overline{S}_{ij}\overline{S}_{ij} + \Omega_{ij}\Omega_{ij}\right) = \overline{\Delta}^2\left(|\overline{S}|^2 + \omega_i\omega_i\right), \tag{5.14}$$

(where Ω_{ij} is the anti-symmetric part of the velocity gradient tensor, and ω_i the vorticity), which gives

$$\nu_T(\mathbf{x}) = 0.063\overline{\Delta}^2\left(|\overline{S}|^2 + |\omega|^2\right)^{1/2}. \tag{5.15}$$

For isotropic flows, the model is less dissipative than the Smagorinsky model, in which values such as $C_s = 0.18 - 0.23$ are commonly used; this is reflected in a more accurate prediction of the inertial range (see, for instance, Fig. 2 in the article by Lesieur & Métais 1995). For sheared flows, however, the structure function may be excessively dissipative. Improved results were obtained by applying a Laplacian filter to remove the contribution of the largest eddies to the velocity gradient before computing the structure function (Ducros *et al.* 1996).

Métais & Lesieur (1992) also proposed a modification of the eddy viscosity in (5.11) to account for deviations of the spectrum from the 5/3 Kolmogorov law. Assuming that $E(k) \propto k^{-m}$ gives a correction to the plateau level, which is decreased for $m > 5/3$ (see Fig. 5.1), while maintaining a cusp-like behavior for $k \simeq k_m$. This "spectral-dynamic model" resulted in improved results in transitional flows, in the near-wall region of turbulent flows, or in regions of intermittent flow, where the spectrum is steeper than $k^{-5/3}$ (see Lamballais *et al.* 1998).

5.5 Scale-similar and mixed models

Scale-similar models are based on the assumption that the most active subgrid scales are those closer to the cutoff, and that the scales with which they interact most are those right above the cutoff (Bardina *et al.* 1980). The "largest subgrid scales" can be obtained by filtering the SGS velocity $u'_i = u_i - \overline{u}_i$ to obtain

$$\overline{u'_i} = \overline{u}_i - \overline{\overline{u}}_i. \tag{5.16}$$

If the SGS stresses are decomposed in terms of $\overline{u}_i$ and u_i', (5.16) is used, and a Smagorinsky model is added to represent the dissipative effect of the small scales, the mixed model can be written as

$$\tau_{ij} - \frac{\delta_{ij}}{3}\tau_{kk} = C_B\left[\overline{\overline{u}_i\overline{u}_j} - \overline{\overline{u}}_i\,\overline{\overline{u}}_j - \frac{\delta_{ij}}{3}\left(\overline{\overline{u}_k\overline{u}_k} - \overline{\overline{u}}_k\,\overline{\overline{u}}_k\right)\right] - 2\nu_T\overline{S}_{ij}. \tag{5.17}$$

The first part of the model is the scale-similar model; the Smagorinsky contribution provides the dissipation that is underestimated by the scale-similar part alone.

Another form of a scale-similar model can be obtained by applying a second filter, $\widehat{G}$, with characteristic length $\widehat{\Delta} > \overline{\Delta}$, to the velocity field (Liu *et al.* 1994). The SGS stresses can be parameterized as

$$\tau_{ij} = -2\nu_T\overline{S}_{ij} + \widehat{\overline{u}_i\overline{u}_j} - \widehat{\overline{u}}_i\,\widehat{\overline{u}}_j. \tag{5.18}$$

This model has been applied by Anderson & Meneveau (1999) to the simulation of homogeneous isotropic turbulence decay. Scale-similar and mixed models have been recently revisited in the framework of dynamic modeling ideas and will be discussed later.

5.6 Dynamic models

The introduction of dynamic modeling ideas (Germano *et al.* 1991) has spurred significant progress in the subgrid-scale modeling of non-equilibrium flows. In dynamic models for the subgrid-scale stresses, the model coefficients are computed dynamically as the calculation progresses, rather than input *a priori* as in the standard Smagorinsky (1963) model. This is accomplished by defining a *test* filter (denoted by a caret) whose width $\widehat{\Delta}$ is larger than the *grid* filter-width $\overline{\Delta}$ (typically, $\widehat{\Delta} = 2\overline{\Delta}$). Dynamic adjustment of the model coefficients is based on the identity (Germano 1992)

$$\mathsf{L}_{ij} \equiv T_{ij} - \widehat{\tau}_{ij}, \tag{5.19}$$

which relates the "resolved turbulent stresses" $\mathsf{L}_{ij} = \widehat{\overline{u}_i\overline{u}_j} - \widehat{\overline{u}}_i\,\widehat{\overline{u}}_j$ (the contribution from the region between test-filter and grid-filter scale), the subgrid-scale stresses τ_{ij} and the subtest stresses $T_{ij} = \widehat{\overline{u_iu_j}} - \widehat{\overline{u}}_i\widehat{\overline{u}}_j$, which are obtained by applying the test filter $\widehat{G}$, of characteristic width $\widehat{\Delta}$, to the filtered Navier-Stokes equations.

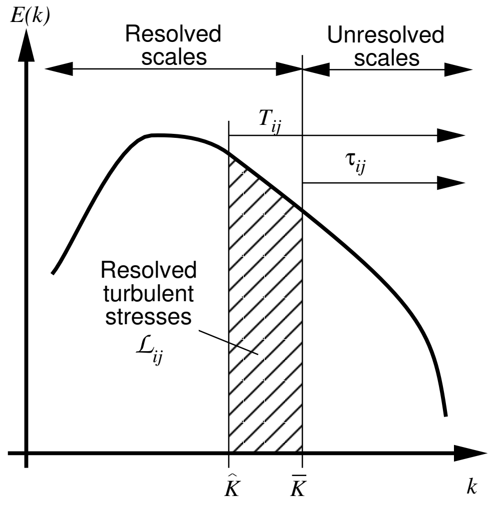

Figure 5.2: Grid- and test-filtering for the dynamic model.

Consider now an eddy-viscosity model to parameterize both subgrid and subtest stresses, of the form

$$\tau_{ij} = -2C\alpha_{ij}; \quad T_{ij} = -2C\beta_{ij}. \tag{5.20}$$

Upon substituting (5.20) into (5.19), the identity (5.19) can be satisfied only approximately, since the stresses are replaced by modeling assumptions, and the system is over-determined (five independent equations are available to determine a single coefficient). Lilly (1992) proposed that the error incurred when a single coefficient is used be minimized in a least-square sense.[1] The error is

$$e_{ij} = \mathsf{L}_{ij} - T_{ij} + \widehat{\tau_{ij}} = \mathsf{L}_{ij} + 2CM_{ij}. \tag{5.21}$$

with $M_{ij} = \beta_{ij} - \widehat{\alpha_{ij}}$. The least-squares minimization procedure requires that

$$\frac{\partial E^2}{\partial C} = \frac{\partial\langle e_{ij}e_{ij}\rangle}{\partial C} = 2\left\langle e_{ij}\frac{\partial e_{ij}}{\partial C}\right\rangle = 0 \tag{5.22}$$

[1] It is assumed here that the model coefficient is smooth on the $\widehat{\Delta}$ scale, and can, therefore, be extracted from the filtering operation.

where the brackets indicate an appropriate ensemble average; since $\partial e_{ij}/\partial C = 2M_{ij}$, this implies that

$$\langle (\mathsf{L}_{ij} + 2CM_{ij})\, M_{ij} \rangle = 0 \tag{5.23}$$

which gives

$$C = -\frac{1}{2}\frac{P_{\mathsf{L}M}}{P_{MM}}, \tag{5.24}$$

where $P_{EF} = \langle E_{ij} F_{ij} \rangle$.

This procedure can be applied to mixed models, or models with more than one coefficient as well. For a one-coefficient mixed model of the form

$$\tau_{ij} = A_{ij} - 2C\alpha_{ij}; \quad T_{ij} = B_{ij} - 2C\beta_{ij}, \tag{5.25}$$

the least-squares minimization procedure gives

$$C = -\frac{1}{2}\frac{P_{\mathsf{L}M} - P_{NM}}{P_{MM}}, \tag{5.26}$$

with $N_{ij} = B_{ij} - \widehat{A_{ij}}$. In the case of two model coefficients

$$\tau_{ij} = C_1 A_{ij} - 2C_2\alpha_{ij}, \quad T_{ij} = C_1 B_{ij} - 2C_2\beta_{ij}, \tag{5.27}$$

it is necessary to require that $\partial E^2/\partial C_1 = \partial E^2/\partial C_2 = 0$ to yield

$$C_1(\mathbf{x},t) = \frac{P_{MN}P_{\mathsf{L}M} - P_{MM}P_{\mathsf{L}N}}{P_{MN}P_{MN} - P_{MM}P_{NN}}, \tag{5.28}$$

$$C_2(\mathbf{x},t) = -\frac{1}{2}\frac{P_{MN}P_{\mathsf{L}N} - P_{NN}P_{\mathsf{L}M}}{P_{MN}P_{MN} - P_{MM}P_{NN}}. \tag{5.29}$$

The ensemble average has the purpose of removing very sharp fluctuations of the coefficient, which tend to destabilize numerical calculations, and make the model inconsistent, since the model coefficients cannot be extracted from the filtering operation (*i.e.*, the difference $\widehat{C\alpha_{ij}} - C\widehat{\alpha_{ij}}$ becomes significant). Germano *et al.* (1991) averaged the model coefficient over all homogeneous directions, thereby removing completely the mathematical inconsistency. Ghosal *et al.* (1995) used an integral formulation of the identity (5.19) that rigorously removed the mathematical inconsistency at the expense of having to solve an integral equation at each time-step (an expense comparable to the solution of a Poisson equation, therefore significant). Localized filtering can be performed over the scale $\widehat{\Delta}$ (somewhat justifiable by the consideration that, if the same coefficient is used to model both τ_{ij} and T_{ij}, it must be smooth on the test-filter scale). Zang *et al.* (1993) performed this type of averaging; the inclusion of the scale-similar part into their model decreased the contribution of the eddy-viscosity term, and no spuriously high values of the coefficient were observed.

Meneveau *et al.* (1996) proposed a Lagrangian ensemble average based on the consideration that the memory effects should be calculated in a Lagrangian framework, following the fluid particle, rather than at an Eulerian point, which sees different particles, with different histories, at each instant. This average is defined as

$$\mathsf{I}_f = \langle f \rangle = \int_{-\infty}^{t} f(t')W(t-t')dt' \tag{5.30}$$

where the integral is carried out following a fluid path-line. If $W(t)$ is chosen to be an exponential function (to give more weight to recent times) the integrals at time-step n are governed by a passive-scalar-type transport equation, and can be conveniently evaluated using a simple relaxation technique; for instance

$$\begin{aligned} \mathsf{I}^n_{\mathsf{L}M} &= \int_{-\infty}^{t} \mathsf{L}_{ij}(t')M_{ij}(t')W(t-t')dt' \\ &= H\left\{\varepsilon \mathsf{L}^n_{ij}M^n_{ij} + (1-\varepsilon)\mathsf{I}^{n-1}_{\mathsf{L}M}(\mathbf{x} - \mathbf{u}^n\overline{\Delta}t)\right\} \end{aligned} \tag{5.31}$$

where H is the Heaviside function, the evaluation of the integrals at the Lagrangian point $\mathbf{x} - \mathbf{u}^n\overline{\Delta}t$ is performed by linear interpolation, and $\varepsilon = (\Delta t/T)/(1 + \Delta t/T)$. The Lagrangian averaging has been performed successfully, within the framework of eddy-viscosity and mixed models, by Wu & Squires (1997), Anderson & Meneveau (1999) and Sarghini *et al.* (1999).

5.7 Deconvolution models

"Deconvolution" is the process of re-constructing the total (unfiltered) velocity $u_i = \overline{u}_i + u_i'$ from the resolved one $\overline{u}_i$. If the filter function G is invertible, deconvolution is trivial, since it simply consists of applying the inverse filter, G^{-1}, to $\overline{u}_i$. The main difficulty involved in deconvolution consists in the fact that filters with compact support in Fourier-space are non-invertible, since their application results in loss of information. This implies that the deconvolution can only be approximate, in the sense that one can only obtain an approximation u_i^* of the total velocity $u_i = \overline{u}_i + u_i'$ from the resolved one $\overline{u}_i$.

Given an approximation u_i^* of the total velocity u_i, the SGS stresses to be modeled directly in terms of the estimated total velocity as

$$\tau_{ij} = \overline{u_i^* u_j^*} - \overline{u}_i \overline{u}_j \qquad \text{or} \qquad \tau_{ij} = \overline{u_i^* u_j^*} - \overline{u_i^*}\ \overline{u_j^*}. \tag{5.32}$$

The scale-similar model (5.17) can be interpreted as a deconvolution model in which $u_i^* = \overline{u}_i$.

Recently, several models have been developed that use approximate deconvolution methods. Shah and Ferziger (1995) defined the inverse filter in terms of a Taylor-series expansion of the filtered velocity (Leonard 1974). They calculated plane-channel flows and obtained improved results compared with the plane-averaged dynamic model.

Domaradzki and co-workers (1997,1999,2000) developed the "Subgrid-scale estimation model". Although their approach was originally developed in Fourier space; Domaradzki and Loh (1999) extended it to the physical representation of the velocity. In physical space the subgrid-scale estimation model consists in estimating the velocity on a finer grid than the LES one by using an approximate deconvolution procedure, an exact inversion of the top-hat filter (which does not give any additional information about the scales below the cutoff), followed by a "dynamic step", a correction that generates smaller-wavelength fluctuations. The dynamics step consists of an approximate integration of the non-linear term of the Navier-Stokes equations computed using the deconvolved velocity. This model also gave improved *a priori* and *a posteriori* results in the LES of plane-channel flow (Domaradzki and Loh 1999) and isotropic turbulence (Domaradzki and Yee 2000).

Stolz and co-workers (1999,2001) have also proposed a model based on approximate deconvolution, in which they define an inverse filtering operator, Q_N, as a truncated series of filtering operations:

$$Q_N = \sum_{n=1}^{N} (I - G)^n \simeq G^{-1}. \tag{5.33}$$

The transfer function of this operator shows that the highest wave-numbers contained in the resolved field are significantly amplified. They include a relaxation term that effectively acts as a dissipative component. They also obtained improved results in channel-flow calculations. Their method is less computationally expensive than either the dynamic computation of the eddy-viscosity coefficient, or the subgrid-scale estimation model; however, it should, however, be pointed out that, among the deconvolution methods discussed here, the subgrid-scale estimation model is the only one in which new information (*i.e.*, shorter-wavelength eddies) is introduced; the methods used both by Shah and Ferziger (1995) and Stolz and co-workers (1999,2001) only modify the existing modes.

Chapter 6

LES – APPLICATIONS

6.1 Building-block flows

The initial applications of LES were to simple, building-block flows: homogeneous turbulence, mixing layers, plane channel flows. Despite the fact that DNS and experiments have been used extensively to investigate these flows, the application of LES to study them can be justified: first, the availability of high-quality DNS data makes them ideally suited as test beds for subgrid-scale modeling ideas. Secondly, LES can be performed at a fraction of the cost of DNS; parametric studies, in which many computations are required, are feasible by LES, not by DNS. As usual, the following should not be construed as a complete review of calculations in this area, but only as a brief panorama of some issues that, in the author's view, are particularly relevant.

6.1.1 Wall-bounded flows

The presence of a solid boundary affects the physics of the subgrid scales in several ways. First, the growth of the small scales is inhibited by the presence of the wall. Secondly, the exchange mechanisms between the resolved and unresolved scales are altered; finally, in the near-wall region the subgrid scales may contain some significant Reynolds-stress producing events, and the SGS model must account for them. As mentioned before, two approaches are possible: the wall layer may be resolved, or modeled. These approaches have substantially different modeling requirements, and allow different degrees of detail and accuracy in the solution.

In simulations in which the wall layer is resolved, the phenomena described before were usually included by decreasing the length scale in the eddy viscosity by the addition of damping functions of the van Driest (1956) type. Substantial progress was achieved with the introduction of the dynamic eddy-viscosity model (Germano *et al.* 1991), which ensures the correct near-wall behavior of the SGS stresses without the need for ad hoc adjustments or wall damping functions. This results in reduced SGS dissipation in the near-wall region compared with the Smagorinsky model, and more accurate prediction of the turbulence physics there.

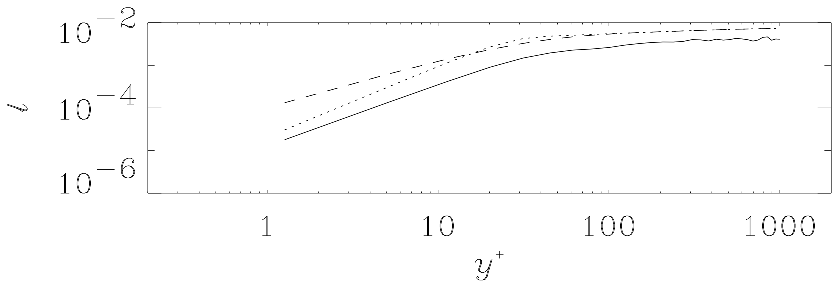

Figure 6.1: Comparison of dynamic model and Smagorinsky model length scales. ——— ℓ_d (dynamic model); - - - ℓ_s (Smagorinsky model); ········ ℓ_p (Smagorinsky model with correct asymptotic behavior). From Piomelli (1993).

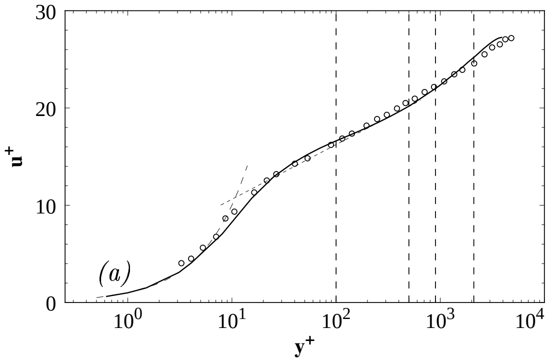

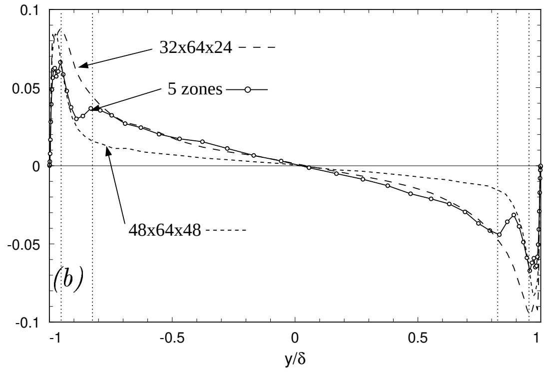

Figure 6.3: (a) Mean velocity profile in fully developed channel flow at $Re_c = 109\,410$. ——— LES on 9-zone embedded grid; ⋄ Experiment, $Re_c = 120\,000$. (b) Subgrid-scale shear stresses in the LES of fully developed channel flow at $Re_c = 46\,300$. - - - Zonal boundaries. Reproduced with permission from Kravchenko *et al.* (1996).

A comparison of the length scales used in the dynamic model, $\ell_d = (C\overline{\Delta}^2)^{1/2}$, and in the Smagorinsky model, $\ell_s = 0.1\overline{\Delta}[1-\exp(-y^+/25)]$ is shown in Fig. 6.1. The length scale ℓ_s is almost ten times larger than ℓ_d in the near-wall region, resulting in a subgrid-scale dissipation that is one hundred times larger. Even if the damping function in the expression for ℓ_s is changed to account for the near-wall behavior of τ_{12} as recommended by Piomelli *et al.* (1988), where the length scale used is $\ell_p = 0.1\overline{\Delta}[1-\exp(-y^{+3}/25^3)]^{1/2}$, the Smagorinsky model remains more dissipative than the dynamic model.

A similar decrease of the eddy viscosity in the near-wall region is achieved when using the filtered structure-function model (Ducros *et al.* 1996). Although the near-wall behavior is incorrect (the decrease of the eddy viscosity in this case is too fast near the wall) the results remain accurate, as long as the grid resolution is sufficient. This result points out an interesting paradox: the SGS models that give the most accurate results in the LES of wall-bounded flows are those in which the wall-layer is treated by DNS.

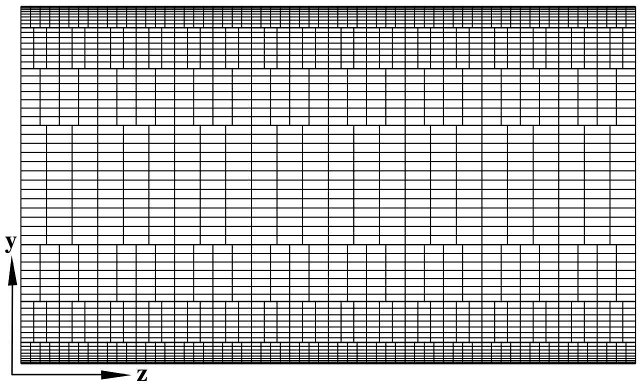

Figure 6.2: Zonal embedded grid with fine grid zones near the walls and coarse zones in the middle of the channel. Reproduced with permission from Kravchenko *et al.* (1996).

As discussed in Section 3.1.2, resolving the wall layer requires extremely fine meshes. If a single structured mesh is used, this resolution requirement results in an excessively fine resolution of the outer flow: the use of block-structured meshes may alleviate this problem. Kravchenko *et al.* (1996) used zonal embedded meshes and a numerical method based on B-splines to compute the flow in a plane channel by DNS and LES. The use of the B-splines allows use of an arbitrarily high order of accuracy for the differentiation, and accurate interpolation at the interface between the zones. A typical grid for the channel flow simulations is shown in Fig. 6.2. The use of zonal grids allowed Kravchenko *et al.* (1996) to perform an LES of the flow at $Re_c = 109\,410$ using 9 embedded zones allowed them to resolve the wall (the grid spacing was $\Delta x^+ \simeq 130$, $\Delta z^+ \simeq 20$) using a total of 2 million points. A single-zone mesh with the same resolution would have under-resolved the wall layer. The mean velocity profile was in excellent agreement with the experimental data (Fig. 6.3a).

Kravchenko *et al.* (1996) used the dynamic eddy viscosity model in the formulation proposed by Lilly (1992); it is interesting to observe the behavior of the SGS stresses near the zonal boundaries (Fig. 6.3b). Since in coarser meshes more energy resides in the subgrid-scale motions, the eddy viscosity increases near the boundary between a finer and a coarser zone. In each zone, moreover, the SGS stress is very close to the value obtained from a single-zone calculation in which the resolution of the embedded zone is matched.

6.1.2 Free-shear flows

Both wall-bounded and free-shear flows have been useful testing grounds for models and numerical methods. Among the latter, the mixing layer has received much attention. LES of temporally developing mixing layers have been performed by Vreman *et al.* (1995a,1997) and others, and spatially developing ones by Comte *et al.* (1998), de Bruin *et al.* (1999) and Li *et al.* (2000). A recent calculation by Balaras *et al.* (2000) shows how the lower computational cost of LES can be used to advantage to perform parametric studies that are not feasible by DNS.

In this calculation the effect of the initial conditions and the size of the computational box on the turbulent statistics and structures were examined in detail. A series of calculations was initialized using two different realizations of a spatially developing turbulent boundary layer with their respective free streams moving in opposite directions. Computations initialized with mean flow plus random perturbations with prescribed moments were also conducted. In all cases, the initial transitional stage, from boundary-layer turbulence or random noise, to mixing-layer turbulence, was followed by a self similar period. The self-similar periods, however, differed considerably: the growth rates, turbulence intensities and vorticity magnitudes showed differences ranging between 10 and 40%, and were affected both by the initial condition and by the computational domain size. In all simulations the presence of quasi two dimensional spanwise rollers is clear, together with 'braid' regions with quasi-streamwise vortices. The development of these structures, however, was different: if strong rollers were formed early (as in the cases initialized by random noise), a well-organized pattern persisted throughout the self-similar period (Fig. 6.4). The presence of boundary-layer turbulence, on the other hand, inhibited the growth of the inviscid instability, and delayed the formation of the roller-braid patterns. Increasing the domain size also tended to make the flow more three-dimensional.

6.2 Transitional and relaminarizing flows

Many flows include regions of transition or relaminarization. Subgrid-scale models, usually based on high Reynolds number dynamics, often have difficulty in these regions. The eddy viscosity predicted by the Smagorinsky model or the structure-function model, for instance, is non-zero in laminar flows; the dissipation introduced by the model during transition is unphysical, and has the effect of damping the growth of the small perturbations. To force the SGS stresses to zero in laminar flows, intermittency factors or low-Reynolds-number corrections have been used (Piomelli *et al.* 1990). In the dynamic eddy-viscosity model, however, the coefficient vanishes in laminar flow, where L_{ij} is identically zero; this results in better prediction of transition without *ad hoc* adjustments.

An additional difficulty in transitional flows is that, during the nonlinear interaction stages of the breakdown, very small structures (thin shear layers, for instance) are generated, that must be resolved even in an LES. Figure 6.5 shows the resolved vertical shear $\partial\overline{u}/\partial y$ in an xy-plane during subharmonic transition in a flat-plate boundary layer. One can observe the development of a shear layer (at $x \simeq 640$ in Fig. 6.5a) that is lifted from the wall and develops the kinks characteristic of the multiple-spike stages. The eddy viscosity (Fig. 6.6) is essentially zero in the laminar region, begins to rise at $x \simeq 700$, and becomes significant where the resolution is marginal. Between the shear layers, the eddy viscosity is small, whereas sharp peaks can be observed where the shear layers are stronger and small scales are being generated. With much coarser resolution than in DNS both the development of the transitional structures and the statistical quantities could be predicted.

Situations in which the perturbations decay leading to a laminar or quasi-laminar state, also occur in engineering applications; in turbulent channel flow, for example, system rotation acts to stabilize the flow near one wall, de-stabilize it near the other. Piomelli & Liu (1995) applied a localized dynamic model to the study of rotating channel flow, and found that the use of a coefficient that was allowed to vary in all space directions, as well as in time, gives better prediction of the turbulent fluctuations than the plane-averaged model, especially on the stable side of the channel where the turbulent activity is concentrated in the down-wash region of the longitudinal roll cells that are formed in this flow. Lamballais *et al.* (1998) also performed DNS and LES of rotating channel flow using the spectral-dynamic model. They explored a range of rotation numbers $Ro_b = 2\Omega\delta/U_b$ (where U_b is the average velocity in the channel, δ the channel half-height and Ω the rotation rate) between 0 and 1.5 (compared with the range $0 \leq Ro_b \leq 0.21$ examined by Piomelli & Liu 1995). They obtained results in fairly good agreement with DNS data and with previous LES calculations.

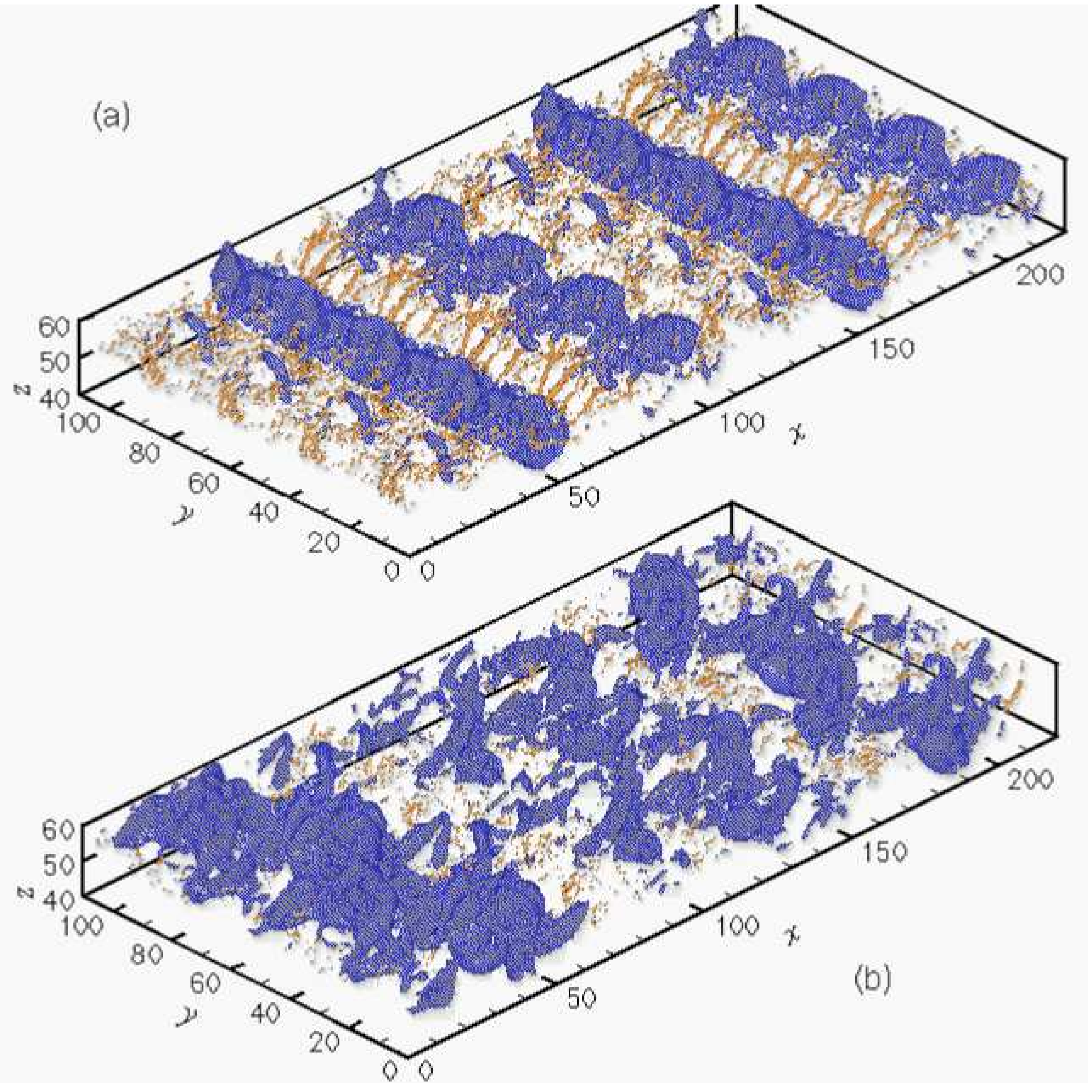

Figure 6.4: Iso-surfaces of P and Q during the self-similar period. (a) Small box calculation initialized with random noise; (b) large box calculation initialized with boundary-layer turbulence. The large domain is repeated twice in the spanwise direction, and the small one three times in the spanwise direction, twice in the streamwise one, for clarity. The iso-surface levels are $P = 0.04\Delta U^2$ (lighter gray) and $Q = 0.05\Delta U^2/\theta_o^2$ (darker gray).

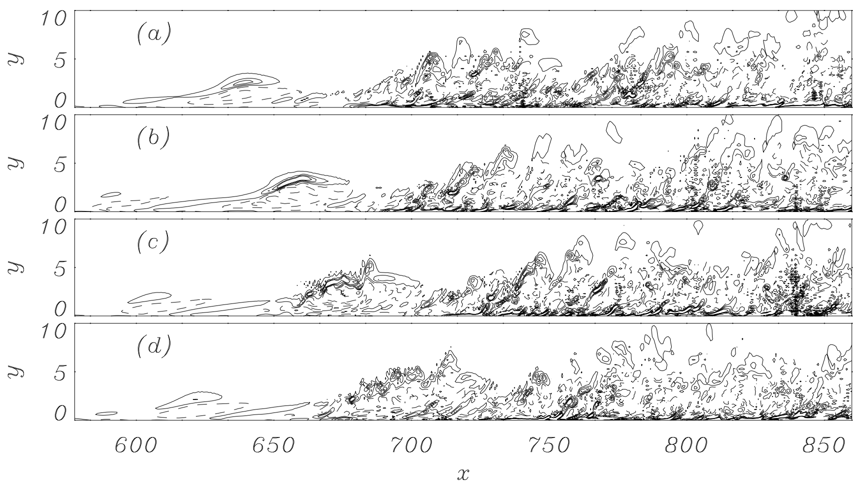

Figure 6.5: Resolved vertical shear $\partial\overline{u}/\partial y$ contours. Subharmonic transition in a flat-plate boundary layer. (a) t_o; (b) $t_o + T/4$; (c) $t_o + T/2$; (d) $t_o + 3T/4$. $T = 136$ is the period of the fundamental wave, and $t_o = 756$. Reproduced with permission from Huai *et al.* (1997).

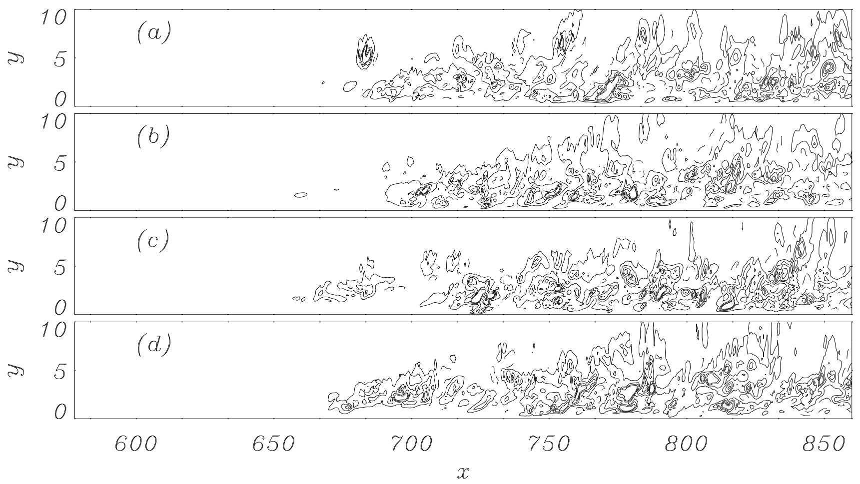

Figure 6.6: Eddy viscosity contours. Subharmonic transition in a flat-plate boundary layer. (a) t_o; (b) $t_o + T/4$; (c) $t_o + T/2$; (d) $t_o + 3T/4$. $T = 136$ is the period of the fundamental wave, and $t_o = 756$. Reproduced with permission from Huai *et al.* (1997).

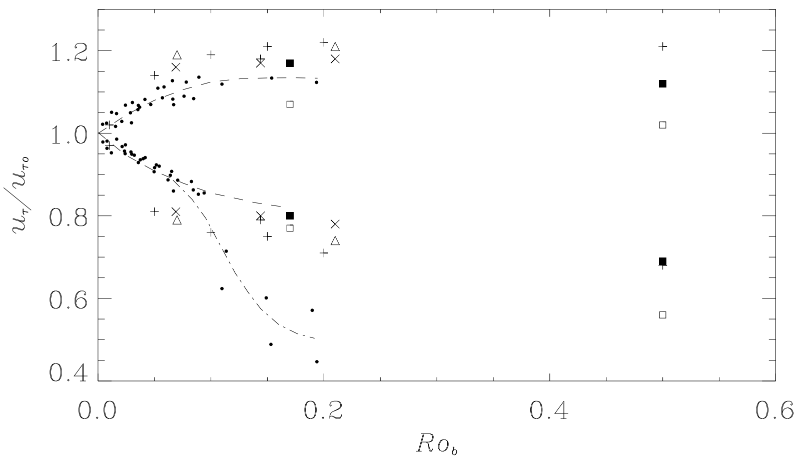

Figure 6.7: Friction velocity in rotating channel flow. ·,– – – ,—·— Experiments (Johnston *et al.* 1972); + DNS (Kristoffersen & Andersson 1993); ■ DNS (Lamballais *et al.* 1998); □ resolved LES (Lamballais *et al.* 1998); × resolved LES (Piomelli & Liu 1995); △ LES with wall models (Balaras *et al.* 1996).

The friction velocity $u_\tau = (\tau_w/\rho)^{1/2}$ (where τ_w is the wall stress and ρ the fluid density) is shown for various rotating-channel cases in Fig. 6.7. The resolved LES of Piomelli & Liu (1995) are in good agreement with DNS data (Kristoffersen & Andersson 1993, Lamballais *et al.* 1998), and with the experimental data on the unstable side of the channel. On the stable side all the numerical calculations predict significantly higher friction velocity than the experiments, in which full relaminarization was observed. This may be due to residual pressure gradients that were present in the experiment due to the small dimensions of the apparatus, which may have increased the tendency of the flow to relaminarize. The resolved LES (Piomelli & Liu 1995, Lamballais *et al.* 1998)) are, however, in good agreement with DNS data (Kristoffersen & Andersson 1993, Lamballais *et al.* 1998) on that side. The LES of Lamballais *et al.* (1998) under-predicts the wall shear on both sides of the channel, but shows trends in good agreement with the DNS results. At the highest rotation rate ($Ro_b = 1.5$, not included in the figure) even the unstable side exhibits a significant decrease in u_τ, predicted by both LES and DNS. Lamballais *et al.* (1998) attributed this to a strong tendency of the vortical structures to be re-oriented in the streamwise direction on the unstable side of the channel (Fig. 6.8). These elongated vortices on the stable side cause rotational motions in the $yz-$plane that result in a decrease in the streamwise *rms* fluctuations (Fig. 6.9), a corresponding increase in the other two components, and an inversion of the flow anisotropy.

A turbulent flow may revert to a laminar one when a boundary layer is subjected to a strong acceleration (a favorable pressure gradient), a situation that occurs in many technological applications (airfoils, ducts, *etc.*). This type of flow fields is not as well understood as the canonical zero-pressure-gradient boundary layer, due to the much wider parameter space, and to the difficulty in determining universal scaling laws similar to those for the zero-pressure-gradient case. A large percentage of the investigations of accelerating flows to date have concentrated on self-similar cases, in which such scaling laws (for instance, the logarithmic law) could be found. Piomelli *et al.* (2000) were the first to perform large-eddy simulations of spatially turbulent boundary layers in strong favorable pressure gradients. The use of LES made possible the calculation of the flow in a long domain, to allow the study of the region in which the flow experiences a perturbation due to the mean-flow acceleration, and the return to equilibrium after the pressure gradient was removed. A DNS of these configuration would have been prohibitively expensive.

Two cases were examined, one in which the acceleration is insufficient to cause reversion to laminar state of the initially turbulent flow (Fig. 6.10a), and one in which the acceleration is stronger, so that relaminarization begins to take place; the pressure gradient was not maintained long enough for full reversion to occur. The mean velocity profile deviated significantly from the logarithmic law-of-the-wall, and showed, in the strongly accelerated case, a tendency to approach the laminar profile, and the turbulent kinetic energy increases less rapidly than the energy of the mean flow. This is reflected in a significant increase of the shape factor $H = \delta^*/\theta$ (where δ^* and θ are respectively the displacement

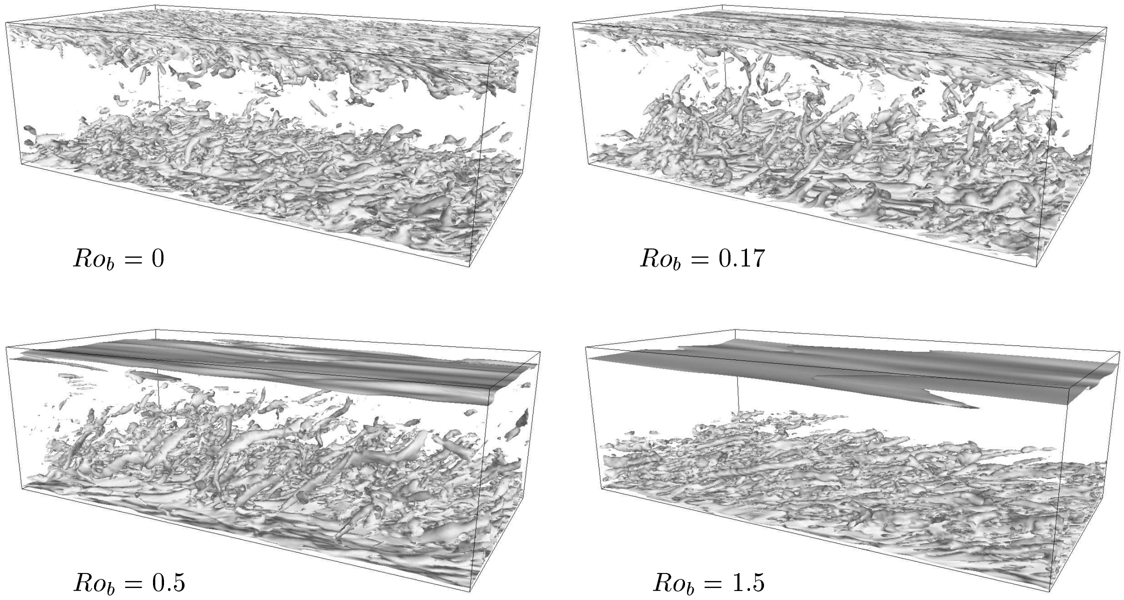

Figure 6.8: Iso-surfaces of the vorticity modulus $\omega = 3U_b/\delta$. $Re_b = 14\,000$. Reproduced with permission from Lamballais *et al.* (1998).

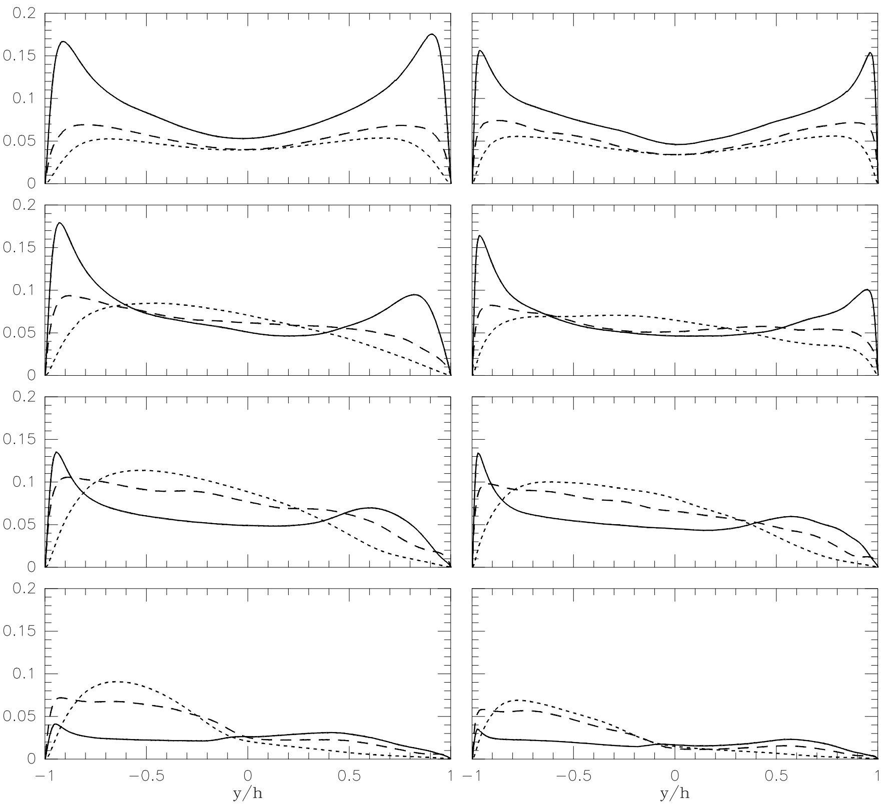

Figure 6.9: *Rms* of the fluctuating velocity components (normalized by U_b). ——— streamwise, ········ wall-normal, – – – spanwise. Left figures: DNS, $Re_b = 5\,000$; right figures: LES, $Re_b = 14\,000$. From top to bottom: $Ro_b = 0$, 0.17, 0.5 and 1.5. h is the channel half-width, δ. Reproduced with permission from Lamballais *et al.* (1998).

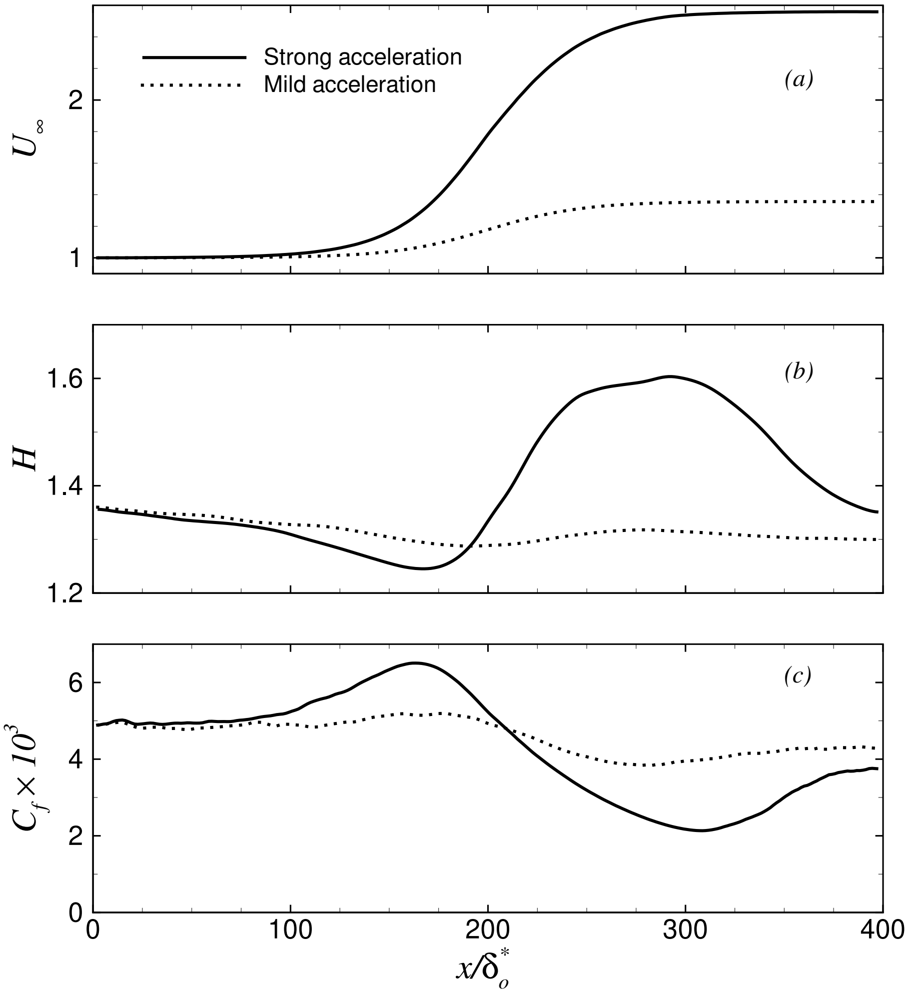

Figure 6.10: Spatial development of mean quantities in the accelerating boundary layer. (a) Mean velocity; (b) shape factor H; (c) skin-friction coefficient C_f.

and momentum thicknesses of the boundary layer), shown in Fig. 6.10b. The skin friction coefficient $C_f = \tau_w/\rho U_\infty^2$, shown in Fig. 6.10c, decreases significantly during the acceleration.

The structure of the inner layer is also significantly altered. In the near-wall region, the streaks become more elongated, and show fewer undulations, due to a significant decrease of the spanwise fluctuations relative to the streamwise ones. The coherent eddies also become fewer, more elongated, and aligned in the streamwise direction, and fewer ejections are observed. In Fig. 6.11, iso-surfaces of Q (defined in Chapter 4) are shown. In the zero-pressure-gradient region, the iso-surfaces of Q highlight the quasi-streamwise vortices known to populate the wall region of equilibrium boundary-layers (Robinson 1991a,1991b). In the mild-acceleration case, the structure in the favorable-pressure-gradient region is not significantly different, although fewer structures can be observed. In the strong-acceleration case, on the other hand, considerably fewer coherent eddies are found. Furthermore, in the zero-pressure-gradient region the eddies form an angle to the wall, and often extend for several hundred wall units into the outer layer, while in the favorable-pressure-gradient region (in the strong acceleration case) they become essentially aligned in the streamwise direction, and much more elongated. Their vorticity is approximately the same as in the zero-pressure-gradient region, despite the presence of an additional vortex-stretching mechanism. This may be due to increased dissipation of the thinner, more intense vortices due to this additional vorticity-generating term.

Scotti and Piomelli (2001) performed LES and DNS of pulsating channel flow. Inherent unsteadiness of the driving conditions characterizes many turbulent flows, both natural (*e.g.* the gravity wave induced in ocean-bottom boundary layers, the blood flow in large arteries, the flow of air in lungs) and artificial (such as the flow in the intake of a combustion engine or the flow in certain heat exchangers). To study the response of turbulence to an oscillating mean flow, a plane-channel flow driven by an oscillating pressure gradient was studied. The physical configuration is illustrated in Fig. 6.12: the flow between two flat plates that extend to $\pm\infty$ in the streamwise (x) and spanwise (y) directions is simulated. To drive this periodic flow, a pressure gradient per unit length is introduced on the right-hand-side of the Navier-Stokes equations as a source term. In the case under investigation, this pressure gradient is given by $1 \times 10^{-4} + \omega \sin \omega t$, where ω is the angular frequency of the oscillation. The flow admits a laminar solution, which is a trivial extension of the Stokes problem. The flow first decelerates (as it is subjected to the adverse pressure gradient during the first half of the cycle), then accelerates again. During the acceleration phase, as observed before, the flow tends to relaminarize, whereas the adverse-pressure-gradient has the opposite effect, and makes the flow more turbulent.

Since the core of the flow, where the velocity is large, is dominated by convective effects, while the regions near the solid boundary, where the velocity gradients are significant, are dominated by diffusive effects, there is a disparity in time-scales between these two regions: the diffusive time-scale being smaller than the convective one by orders of magnitude. Thus, as the frequency is changed, one would expect a significantly different coupling between the near-wall region (the inner layer) and the core of the flow (the outer layer). To study this coupling, calculations were carried out for a range of frequencies. Although the geometry is rather simple, and the grids used relatively coarse, this calculation still requires a large amount of CPU time, due to the long integration time necessary to achieve convergence. Since phase-averaged data is required, between eight and ten cycles of the oscillation are needed to obtain converged statistical samples. If the frequency is low, the equations of motion must be integrated for very long integration. The Reynolds number based on channel height and the time-averaged centerline velocity was 7500 for all calculations. Simulations were carried out for several values of the frequency of the driving pressure-gradient, resulting in a Reynolds number, based on the thickness of the laminar oscillating layer, $\delta = (2\nu/\omega)^{1/2}$ and the oscillating component of the velocity, ranging between $Re_\delta = 100$ and 1000.

The centerline velocity, shown in Fig. 6.13, lags behind the stress at the wall; the phase difference is $\pi/4$ at high frequencies, and drops to zero at low frequencies, where the flow is essentially in equilibrium. The good agreement between DNS and LES at the high frequency can also be observed in this figure. At high frequencies the response of the system is essentially at the driving frequency, despite the non-linear character of the equations. As the frequency is lowered, however, higher harmonics are excited.

Different behaviors of the near-wall region as the frequency is decreased are evident in Fig. 6.14, in which contours of the turbulent kinetic energy are shown. At the highest frequency the inner and outer layers appear largely decoupled. A thickening of the inner layer can be observed at the end of the deceleration phase ($t/T \simeq 1$), which, however, does not propagate far into the outer layer: by $z/H \simeq 0.2$ the contours are nearly undisturbed. At lower frequencies, however, the inner layer has the time to adapt

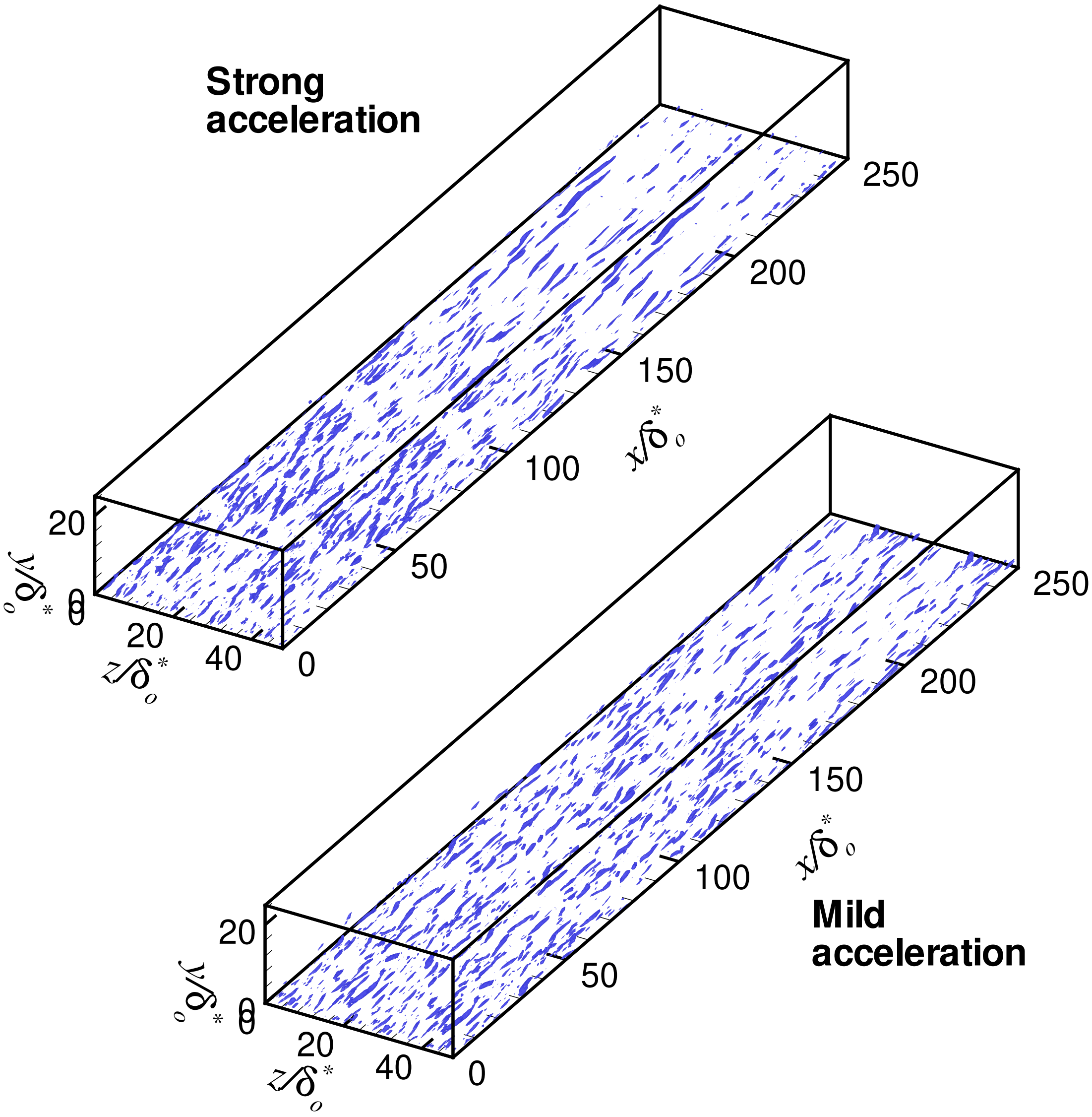

Figure 6.11: Instantaneous iso-surfaces of $Q = 0.02$. Top: strongly accelerating boundary layer. Bottom: mildly accelerating boundary layer.

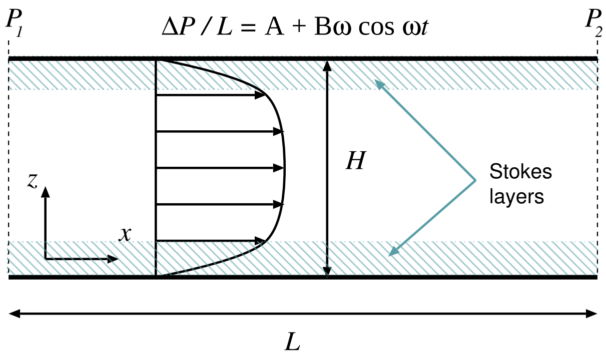

Figure 6.12: Sketch of the physical configuration. Oscillating channel flow.

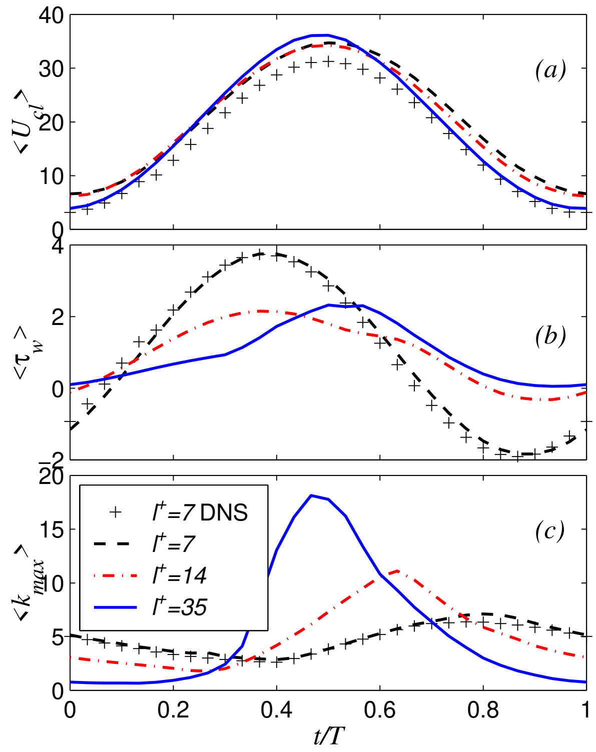

Figure 6.13: Time series of the (a) centerline velocity; (b) wall stress; (c) maximum of the turbulent kinetic energy k.

to the perturbation introduced by the pressure pulse; at the lowest frequencies in particular the flow can be observed to relaminarize, as indicated by the absence of turbulent kinetic energy.

It is interesting to note the asymmetric response of the turbulent kinetic energy at low and intermediate frequencies: at the lowest frequencies the flow at the beginning of the acceleration phase is essentially laminar (although the velocity profile is not, as the viscous time needed to relax to the Poiseuille profile $t^+ \sim Re_\tau^2$ exceeds the period). Figure 6.15 shows contours of the streamwise velocity fluctuations u' during the cycle. One can observe a nearly quiescent flow for $t/T = 0$. As the flow picks up momentum, very long and smooth streaks develop, which, eventually, become unstable and burst into a localized turbulent spot, at $t = 3T/8$, which eventually fills the whole channel. At high frequencies, the process is very different (Fig. 6.16). Fairly healthy streaky structures can be observed for the entire period. During the acceleration phase the flow begins to re-laminarize: some very long, nearly straight low-speed streaks can be observed ($1/8 \leq t/T \leq 2/8$).

6.2.1 Three-dimensional flows

It was mentioned before that large-eddy simulations are based on the assumptions that the small scales are more isotropic, and less affected by the boundary conditions, than the large scales. This assumption justifies the use of simple, equilibrium-based models, even in flows in which the resolved scales are not in equilibrium. By the same token, LES should be more suitable than the Reynolds-averaged approach to study highly three-dimensional or separated flows, especially those in which the gradient transport hypothesis, and consequently one- and two-equation models of turbulence, fails.

Piomelli *et al.* (1997) used the velocity fields from a DNS of the flow in a three-dimensional boundary layer obtained by imposing an impulsive spanwise motion, with magnitude equal to 47% of the initial mean centerline velocity, to the lower wall of a fully-developed plane channel flow (Coleman *et al.* 1996) to study the physics of the SGS stresses subjected to a three-dimensional perturbation. The *a priori* tests showed that the SGS stresses react to the imposition of the secondary shear $\partial W/\partial y$ more rapidly than the large-scale ones, and return to equilibrium before the resolved stresses do. The simulations

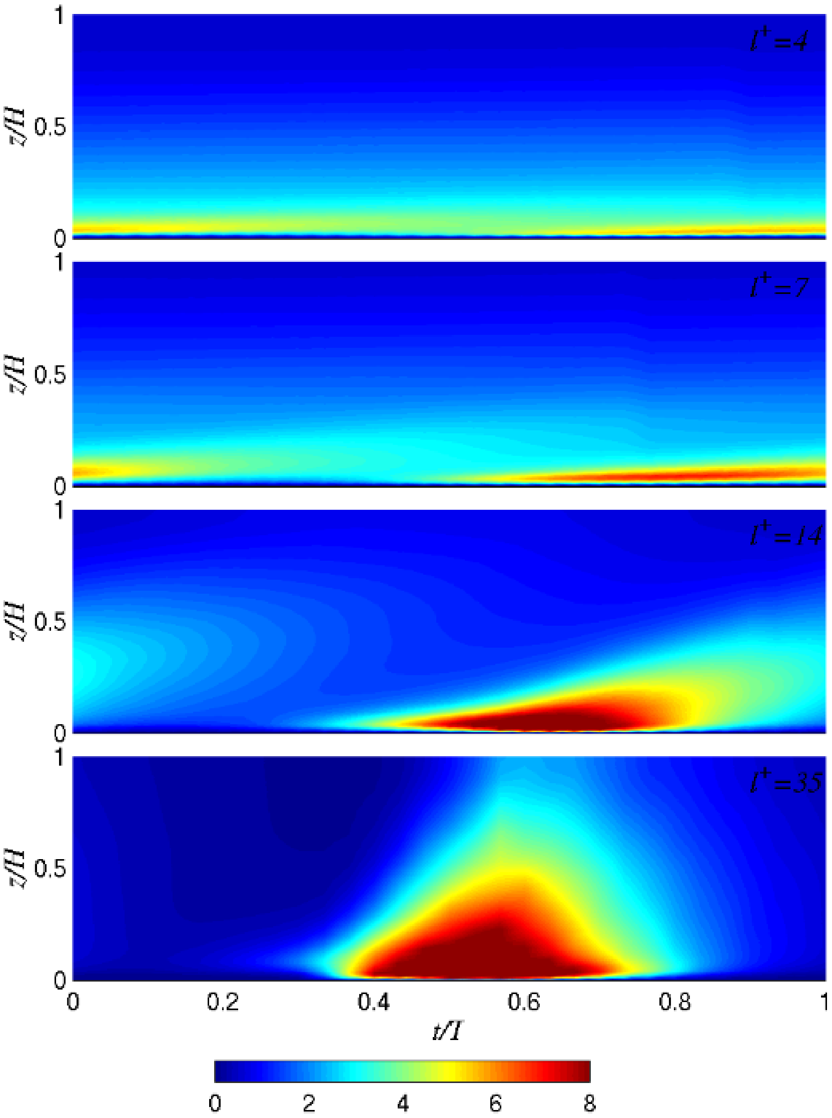

Figure 6.14: Contours of the turbulent kinetic energy (normalized by the mean wall stress) in the oscillating channel. 26 equi-spaced contours between 0 and 12.5 are shown

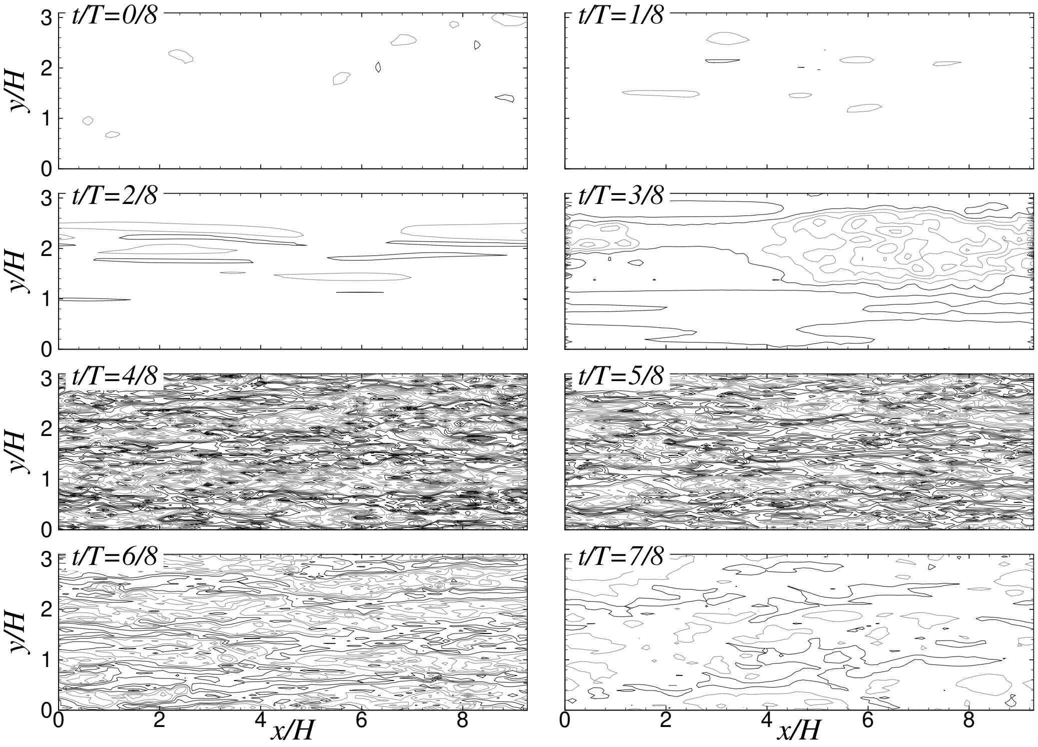

Figure 6.15: Contours of the streamwise velocity fluctuations in the $z^+ = 10$ plane. $l_s^+ = 35$.

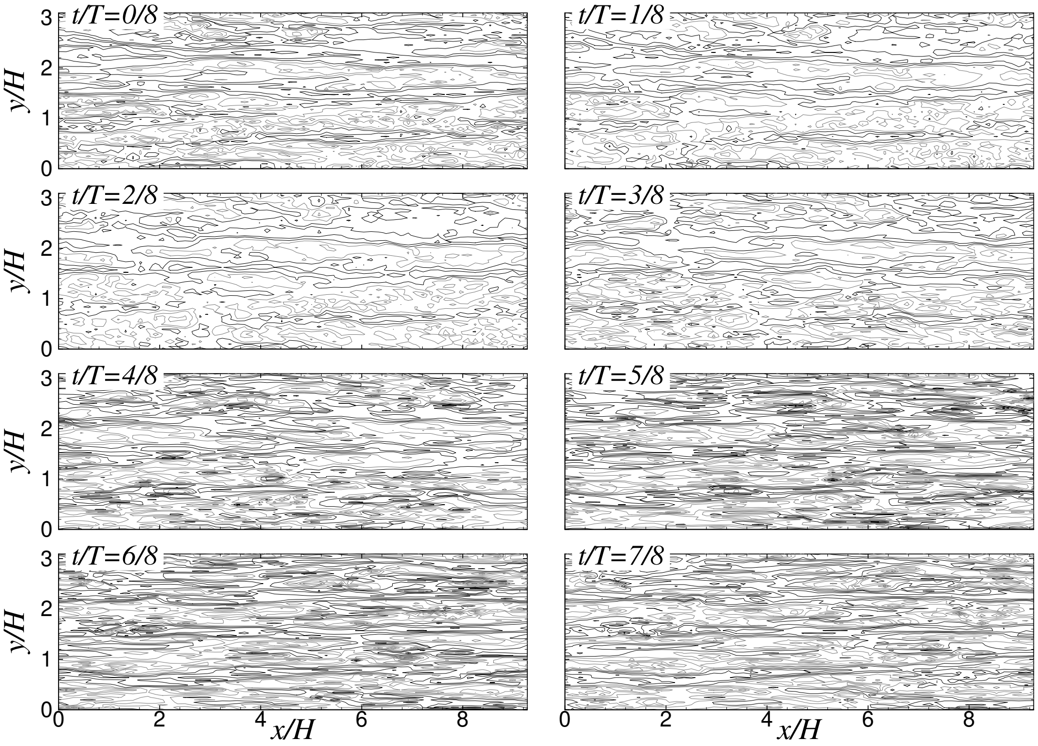

Figure 6.16: Contours of the streamwise velocity fluctuations in the $z^+ = 10$ plane. $l_s^+ = 7$.

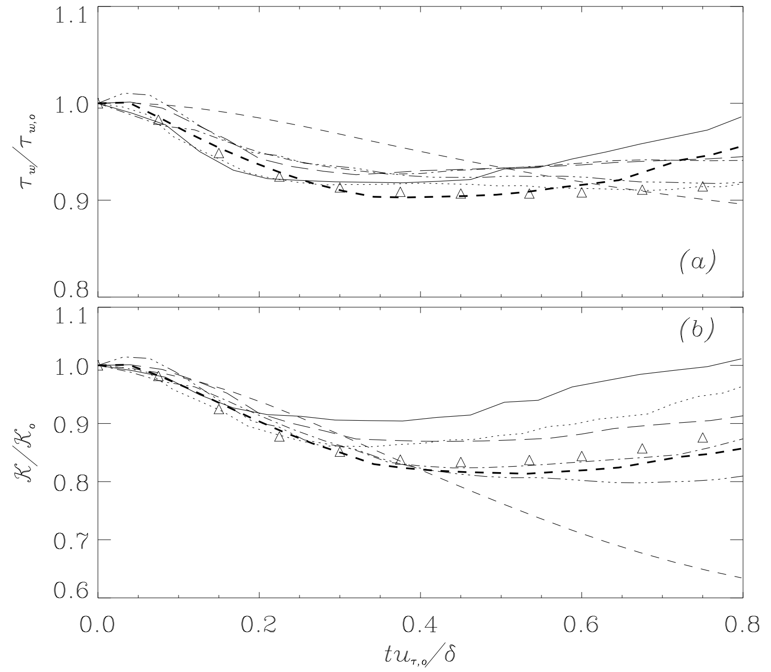

Figure 6.17: Time history of the wall shear stress and average turbulent kinetic energy in the three-dimensional boundary layer flow. All quantities are initialized by their initial values. (a) $\tau_w/\tau_{w,o}$; (b) $\mathcal{K}/\mathcal{K}_o$. ——— Coarse DNS; - - - Smagorinsky Model; —·— Dynamic Eddy-Viscosity Model; ········ Dynamic Mixed Model; —···— One-Coefficient Lagrangian Mixed Model; ▬ Two-Coefficient Lagrangian Mixed Model; △ DNS (Coleman *et al.* 1996).

of Sarghini *et al.* (1999) confirmed the *a priori* tests results: dynamic and scale-similar models give more accurate prediction of the transient, non-equilibrium phenomena. Figure 6.17 shows the time-development of the wall stress τ_w and turbulent kinetic energy $\mathcal{K}$ integrated over the entire computational domain; both quantities are normalized by their initial values. Several models were tested. Computations performed without any model are unable to predict the non-equilibrium effects, and give the incorrect time-development of all the quantities examined. The Smagorinsky model also gives significant errors: before the shear is applied, the model over-predicts the dissipation slightly, especially in the buffer region. The imposition of the strain leads to a doubling of the SGS dissipation that results in excessive damping of the turbulent fluctuations. Dynamic models predict the initial decrease in the turbulence quantities and the successive recovery of the turbulent kinetic energy well. The one-coefficient Lagrangian mixed model (5.17) gives the most accurate results, at a minor penalty in terms of computational cost.

A related study was carried out by Kannepalli & Piomelli (2000). They simulated a spatially developing boundary layer in which a section of the wall was set in motion. A transverse boundary layer develops on the moving plate, that is is found to be decoupled from the streamwise flow. The Reynolds stresses are drastically modified by the imposition of the shear. Significant decreases in the axial skin-friction and turbulent kinetic energy are observed at the junctions of the moving wall, despite the fact that additional energy is delivered to the fluid by the wall motion. The RANS approach has been rather unsuccessful in this type of flow, due to a strong misalignment between the principal axes of the Reynolds-stress and strain-rate tensors. LES, on the other hand, gives statistics in good agreement with experimental data (Lohmann 1976, Driver & Hebbar 1987, Driver & Johnston 1990). The availability of the resolved field allowed Kannepalli & Piomelli (1999) to calculate the Reynolds stress budgets. They found that the decrease in turbulent kinetic energy at the plate junctions is mostly due to a decrease in production, while the dissipation and pressure terms play a relatively minor role. Flow visualizations (Fig. 6.18) showed that at the moving plate junction the additional shear disrupts the near-wall eddies, resulting in a decrease of the Reynolds stress $\langle u'v' \rangle$, and a corresponding decrease in the production of turbulent kinetic energy, not accompanied by an analogous decrease in the dissipation. As the eddies are regenerated, however, the secondary Reynolds stress $\langle v'w' \rangle$ becomes significant, the production increases again,

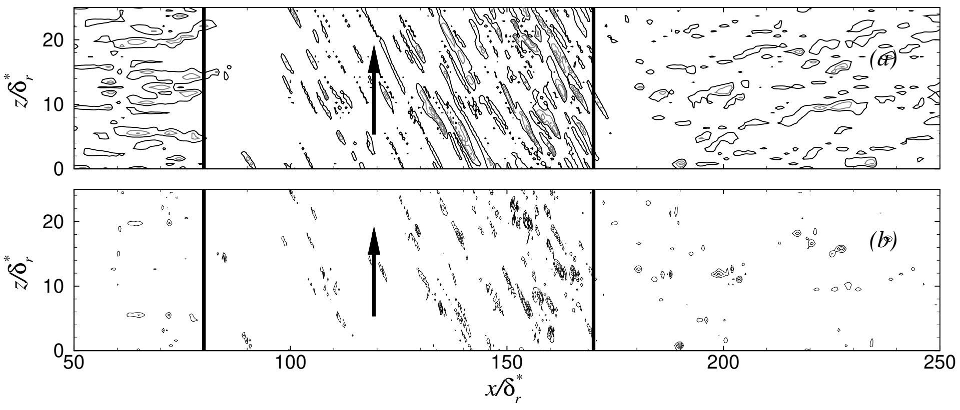

Figure 6.18: Instantaneous contours of (a) u' and (b) $u'v'$ on the $y^+ = 6$ plane. $W_s/U_\infty = 1$. Negative contours in gray.

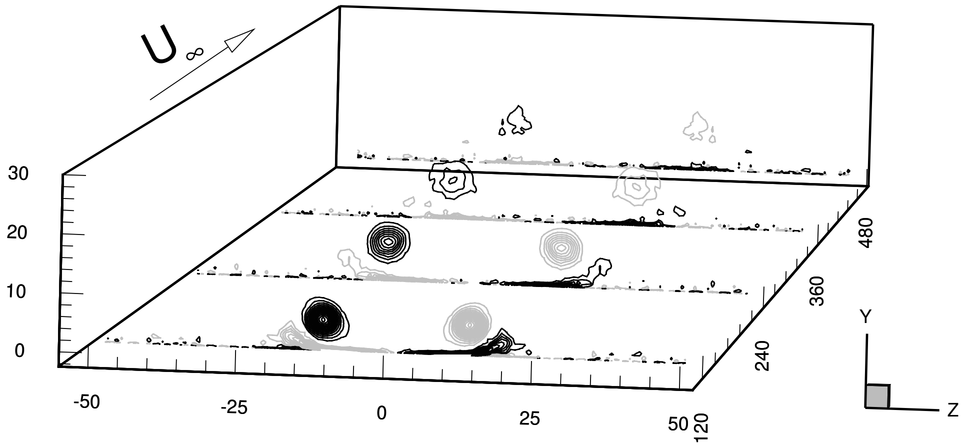

Figure 6.19: Contours of streamwise vorticity at the four streamwise stations. Gray: negative contours, black: positive contours. Reproduced with permission from Liu *et al.* (1996).

and the flow reaches a quasi-equilibrium collateral state, characterized by higher turbulent kinetic energy and Reynolds stresses.

Liu *et al.* (1996) computed the flow in a turbulent boundary layer on which a pair of strong counter-rotating vortices was superimposed, using a localized dynamic model. The vortices generate the extra strain components $\partial V/\partial y$, $\partial V/\partial z$, $\partial W/\partial y$ and $\partial W/\partial z$. The mean streamwise vorticity development is predicted much more accurately than when $\mathcal{K}-\varepsilon$ models are used, due to the fact that two-equation models cannot predict the gradients of the normal stress anisotropy, which play an important role in the development of Ω_x. The magnitude of the eddy viscosity that would be used in $\mathcal{K}-\epsilon$ models is shown in Fig. 6.20. A dot product is used to produce an eddy viscosity:

$$\nu_e \equiv -\frac{\langle u_i'' u_j' \rangle \langle S_{ij} \rangle}{2 \langle S_{ij} \rangle \langle S_{ij} \rangle}. \tag{6.1}$$

(using this "least-squares" definition, ν_e is the eddy viscosity that would give the correct production rate, transferring the correct amount of kinetic energy from the mean flow to the turbulence). The figure compares this quantity and an eddy viscosity calculated from the $\mathcal{K}-\epsilon$ formula, $\nu_e = C_\mu \mathcal{K}^2/\epsilon$, with $C_\mu = 0.09$. The values of ν_e predicted by the $\mathcal{K}-\epsilon$ formulation are close to those obtained directly from the LES away from the vortex; inside the vortex, however, they are roughly double the LES values. This explains the rapid decay of the streamwise vorticity that is observed in $\mathcal{K}-\epsilon$ solutions.

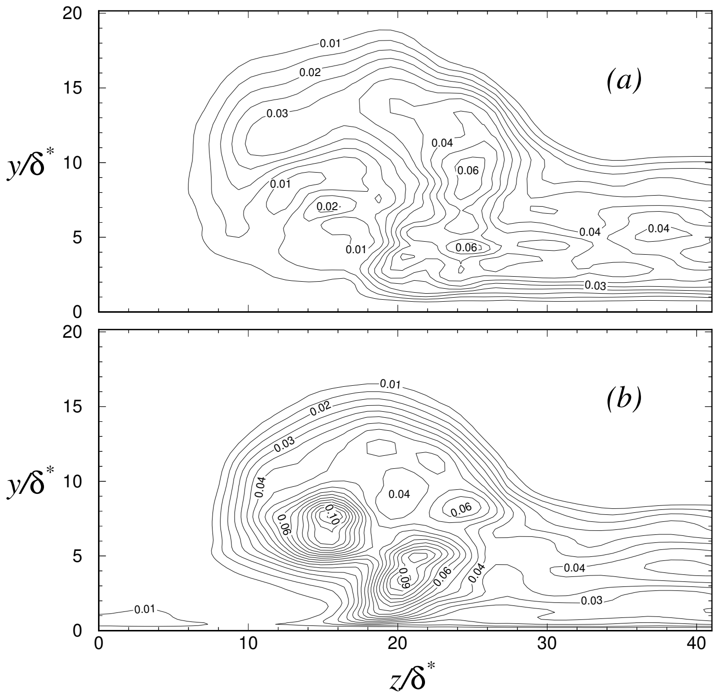

Figure 6.20: Contours of the eddy-viscosity at $x = 340$. (a) ν_e from least-squares fit to LES results; (b) $\nu_e = C_\mu \mathcal{K}^2/\epsilon$. Reproduced with permission from Liu *et al.* (1996).

6.2.2 Separated flows

Separated flows constitute another class of non-equilibrium flows in which RANS models have had mixed success. They present significant challenges for LES calculations as well. Beaudan & Moin (1994) used the dynamic and Smagorinsky SGS models for the LES of the wake of a circular cylinder at $Re = 3\,900$ (based on cylinder diameter and freestream velocity). The dynamic model gave results in better agreement with the experiments than the Smagorinsky model, especially in the recirculation region behind the cylinder. If the boundary layer before separation is subcritical, for instance, along the separation streamline a shear layer develops that is often inviscidly unstable; the grid, in this region, must be sufficiently fine to capture the shear-layer roll-up, and the SGS model must give vanishing eddy viscosity in this region. The dynamic model correctly predicted zero viscosity along the shear layers following separation, unlike the Smagorinsky model.

This calculation highlighted an important numerical issue, that of the effect of numerical dissipation on the resolved scales and on the subgrid-scale model. Mittal & Moin (1997) performed calculations of the same flow, using a second-order central scheme instead of the fifth-order upwind-biased method employed by Beaudan & Moin (1994). They found that the numerical dissipation due to the upwind scheme affected very significantly the spectra (Fig. 6.21). Near the cylinder, the mean velocity and Reynolds stresses were in only slightly better agreement with the experiments, presumably because they are mostly due to large scales contained in a small band of frequencies that was well resolved even when the upwind scheme was used. In the far-wake, on the other hand, the non-dissipative central scheme, and the B-spline block-structured approach applied on the same geometry by Kravchenko (1998) and Kravchenko & Moin (2000) gave more accurate results.

Other separated flows that have been computed by LES include the backward-facing step (Akselvoll & Moin 1995, Delcayre & Lesieur 1997, as well as others), and the coaxial jet, a configuration frequently used as a combustor (Akselvoll & Moin 1996, Pierce & Moin 1998) and an asymmetric plane diffuser (Kaltenbach *et al.* (1999). This flow is particularly difficult to simulate because of the disparity of scales: due to the expansion, the mean velocity and the Reynolds number in the outlet region are 4.7 times lower than in the inlet, and the inertial time scale is $4.7^2 \simeq 22$ times larger. Furthermore, an adverse pressure gradient exists that leads to an unsteady separation. This simulation highlights the effect of

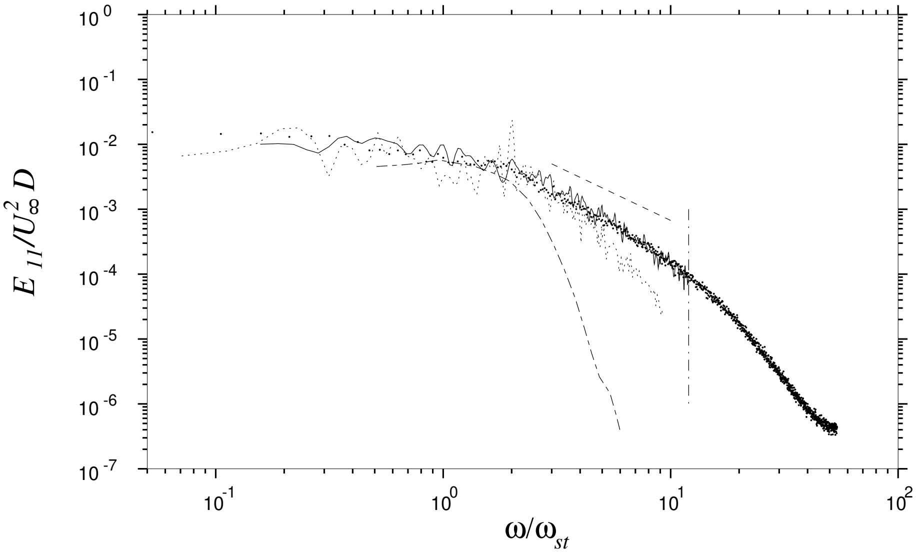

Figure 6.21: One-dimensional frequency spectrum at $x/D = 7.0$. • experiment; ——— B-Splines; ········ central differences; —·— upwind differences; - - - -5/3 slope. Reproduced with permission from Kravchenko & Moin (1998).

the boundary conditions on the accuracy of the results. Kaltenbach *et al.* (1999) found that, when fully developed channel flow was used to supply the inflow data, the separation point was predicted incorrectly, a very small reversed-flow region was observed, and the recovery region was not predicted very accurately . When an inlet velocity profile that more closely matched the measured one was assigned, however, much improved results were obtained. This numerical experiment pointed out very strongly that, in order to compare meaningfully experiments and simulations, the boundary conditions must be matched very carefully. Discrepancies between the computational and experimental results should not be attributed too hastily to numerical or modeling errors without investigating in detail whether the numerical flow conditions matched the experimental ones.

Chapter 7

LES – FUTURE DEVELOPMENTS

7.1 Compressible flows

The applications of LES to compressible flows have been far fewer than for incompressible cases. This is also an area that will conceivably see enhanced effort in the near future. In compressible flows, it is convenient to use Favre-filtering (Favre 1965a,1965b) to avoid the introduction of subgrid-scale terms in the equation of conservation of mass. A Favre-filtered variable is defined as:

$$\tilde{f} = \overline{\rho f}/\overline{\rho}; \tag{7.1}$$

the Favre-filtered equations of motion can be written in the form:

$$\frac{\partial \overline{\rho}}{\partial t} + \frac{\partial}{\partial x_j}\left(\overline{\rho}\widetilde{u}_j\right) = 0, \tag{7.2}$$

$$\frac{\partial \overline{\rho}\,\widetilde{u}_i}{\partial t} + \frac{\partial}{\partial x_j}\left(\overline{\rho}\widetilde{u}_i\widetilde{u}_j\right) + \frac{\partial \overline{p}}{\partial x_i} - \frac{\partial \widetilde{\sigma}_{ji}}{\partial x_j} = \underbrace{-\frac{\partial \tau_{ji}}{\partial x_j}}_{\mathsf{I}} + \underbrace{\frac{\partial}{\partial x_j}\left(\overline{\sigma}_{ji} - \widetilde{\sigma}_{ji}\right)}_{\mathsf{II}}, \tag{7.3}$$

where a perfect-gas equation of state is assumed, and

$$\overline{\sigma}_{ij} = \overline{2\mu \overline{S}_{ij}} + \overline{\left(\mu_2 - \frac{2}{3}\mu\right)\delta_{ij}\overline{S}_{kk}} \tag{7.4}$$

$$\widetilde{\sigma}_{ij} = 2\widetilde{\mu}\widetilde{S}_{ij} + \left(\widetilde{\mu}_2 - \frac{2}{3}\widetilde{\mu}\right)\delta_{ij}\widetilde{S}_{kk}; \tag{7.5}$$

here $\widetilde{S}_{ij}$ is the Favre-filtered strain-rate tensor, μ is the molecular viscosity, and μ_2 the bulk viscosity; $\widetilde{\mu} = \mu(\widetilde{T})$ and $\widetilde{\mu}_2 = \mu_2(\widetilde{T})$ are their values at the filtered temperature $\widetilde{T}$.

Two unclosed terms appear in (7.3): term I, the divergence of the SGS stresses $\tau_{ij} = \overline{\rho}(\widetilde{u_i u_j} - \widetilde{u}_i\widetilde{u}_j)$, and term II, which is due to the nonlinearity of the viscous stresses. While the former is modeled, the latter is invariably neglected (*i.e.*, it is assumed that $\overline{\sigma}_{ji} - \widetilde{\sigma}_{ji} = 0$). The trace of the SGS stresses in compressible flows cannot be included in the modified pressure, and requires separate modeling, although it is frequently neglected (Zang *et al.* 1992).

In addition to the momentum and mass conservation equations, an energy equation is required. Several options are available: one can solve the internal energy, the enthalpy or the total energy equation. Each of these choices results in a different set of terms that must be modeled. The equation for the internal energy per unit mass ϵ, for instance, is

$$\begin{aligned}\frac{\partial(\overline{\rho}\,\widetilde{\epsilon})}{\partial t} + \frac{\partial}{\partial x_j}\left(\overline{\rho}\widetilde{u}_j\widetilde{\epsilon}\right) + \frac{\partial \widetilde{q}_j}{\partial x_j} + \overline{p}\widetilde{S}_{kk} - \widetilde{\sigma}_{ji}\widetilde{S}_{ij} = &\underbrace{-\frac{\partial}{\partial x_j}\left[\overline{\rho}\left(\widetilde{u_j\epsilon} - \widetilde{u}_j\widetilde{\epsilon}\right)\right]}_{\mathsf{III}} \\ &\underbrace{-\frac{\partial}{\partial x_j}[\overline{q}_j - \widetilde{q}_j]}_{\mathsf{IV}} - \underbrace{\left[\overline{p S_{kk}} - \overline{p}\widetilde{S}_{kk}\right]}_{\mathsf{V}} + \underbrace{\left[\overline{\sigma_{ji} S_{ij}} - \widetilde{\sigma}_{ji}\widetilde{S}_{ij}\right]}_{\mathsf{VI}};\end{aligned} \tag{7.6}$$

here

$$\overline{q}_j = -\overline{k\frac{\partial T}{\partial x_j}}, \quad \widetilde{q}_j = -\widetilde{k}\frac{\partial \widetilde{T}}{\partial x_j}, \tag{7.7}$$

are heat fluxes, and $\widetilde{k} = k(\widetilde{T})$ is the value of the thermal conductivity obtained using the filtered temperature.

The under-braced terms must be modeled. Term III is the divergence of the subgrid-scale heat flux:

$$\overline{\rho}\left(\widetilde{u_j\epsilon} - \widetilde{u}_j\widetilde{\epsilon}\right) = Q_j/\gamma. \tag{7.8}$$

Term IV is usually neglected, as was the analogous term in the momentum equation. Term V is the SGS pressure-dilatation, and term VI is the SGS contribution to the viscous dissipation. In past applications (Moin *et al.* 1991, El-Hady *et al.* 1994) the subgrid-scale heat-flux Q_i was modeled, while terms V and VI were neglected (as well as the diffusion nonlinearities IV). Vreman *et al.* (1995b) performed *a priori* tests using DNS data obtained from the calculation of a mixing layer at Mach numbers in the range 0.2–0.6, and concluded that neglecting the nonlinearities of the diffusion terms in the momentum and energy equations (terms II and IV) is acceptable; they found, however, that the SGS pressure-dilatation and SGS viscous dissipation are of the same order as the divergence of the SGS heat flux, Q_j, and that modeling term VI improves the results, especially at moderate or high Mach numbers.

Similar terms arise if the equation for the enthalpy $h = \epsilon + p/\rho$ is used:

$$\begin{aligned} &\frac{\partial(\overline{\rho}\widetilde{h})}{\partial t} + \frac{\partial}{\partial x_j}\left(\overline{\rho}\widetilde{u}_j\widetilde{h}\right) + \frac{\partial \widetilde{q}_j}{\partial x_j} - \frac{\partial \overline{p}}{\partial t} - \widetilde{u}_j\frac{\partial \overline{p}}{\partial x_j} - \widetilde{\sigma}_{ji}\widetilde{S}_{ij} = \\ &\quad \underbrace{-\frac{\partial}{\partial x_j}\left[\overline{\rho}\left(\widetilde{u_jh} - \widetilde{u}_j\widetilde{h}\right)\right]}_{\mathsf{VII}} \underbrace{-\frac{\partial}{\partial x_j}[\overline{q}_j - \widetilde{q}_j]}_{\mathsf{IV}} \\ &\quad + \underbrace{\left[\overline{u_j\frac{\partial p}{\partial x_j}} - \widetilde{u}_j\frac{\partial \overline{p}}{\partial x_j}\right]}_{\mathsf{VIII}} + \underbrace{\left[\overline{\sigma_{ji}S_{ij}} - \widetilde{\sigma}_{ji}\widetilde{S}_{ij}\right]}_{\mathsf{VI}}. \end{aligned} \tag{7.9}$$

Terms IV and VI also appear in the internal energy equation; term VII is equal to the divergence of Q_j. The velocity-pressure gradient term VIII can be decomposed to yield the pressure-dilatation term, and a pressure-diffusion part that can be related to Q_j:

$$\begin{aligned} \overline{u_j\frac{\partial p}{\partial x_j}} - \widetilde{u}_j\frac{\partial \overline{p}}{\partial x_j} &= \frac{\partial}{\partial x_j}\left[\overline{pu_j} - \overline{p}\,\widetilde{u}_j\right] - \left[\overline{pS_{jj}} - \overline{p}\widetilde{S}_{jj}\right] \\ &= \frac{\gamma - 1}{\gamma}\frac{\partial Q_j}{\partial x_j} - \left[\overline{pS_{jj}} - \overline{p}\widetilde{S}_{jj}\right], \end{aligned} \tag{7.10}$$

where the equation of state has been used to give

$$\overline{pu_j} - \overline{p}\,\widetilde{u}_j = \overline{\rho}R\left(\widetilde{Tu_j} - \widetilde{T}\widetilde{u}_j\right) = \frac{\gamma - 1}{\gamma}Q_j. \tag{7.11}$$

The pressure-dilatation term has been neglected in the past (Speziale *et al.* 1988, Erlebacher *et al.* 1992).

The third option is to use an equation for the filtered total energy per unit mass $\widetilde{E} = \widetilde{\epsilon} + \widetilde{u_ju_i}/2$:

$$\begin{aligned} &\frac{\partial}{\partial t}(\overline{\rho}\,\widetilde{E}) + \frac{\partial}{\partial x_j}\left(\overline{\rho}\,\widetilde{u}_j\widetilde{E}\right) + \frac{\partial \widetilde{q}_j}{\partial x_j} + \frac{\partial}{\partial x_j}(\overline{p}\widetilde{u}_j) - \frac{\partial}{\partial x_j}(\widetilde{\sigma}_{ji}\widetilde{u}_j) = \\ &\quad \underbrace{-\frac{\partial}{\partial x_j}\left[\overline{\rho}\left(\widetilde{u_jE} - \overline{\rho}\widetilde{u}_j\widetilde{E}\right)\right]}_{\mathsf{IX}} \underbrace{-\frac{\partial}{\partial x_j}[\overline{q}_j - \widetilde{q}_j]}_{\mathsf{IV}} \\ &\quad \underbrace{-\frac{\partial}{\partial x_j}\left[\overline{pu_j} - \overline{p}\widetilde{u}_j\right]}_{\mathsf{X}} + \underbrace{\frac{\partial}{\partial x_j}\left[\overline{\sigma_{ji}u_i} - \widetilde{\sigma}_{ji}\widetilde{u}_j\right]}_{\mathsf{XI}}. \end{aligned} \tag{7.12}$$

In this case the convective term IX gives rise to two unclosed terms:

$$\begin{aligned}\overline{\rho}\left(\widetilde{u_jE}-\overline{\rho}\widetilde{u}_j\widetilde{E}\right) &= \overline{\rho}\left(\widetilde{u_j\epsilon}-\widetilde{u}_j\widetilde{\epsilon}\right)+\overline{\rho}\left(\frac{\widetilde{u_ju_ku_k}}{2}-\frac{\widetilde{u}_j\widetilde{u}_k\widetilde{u}_k}{2}\right)\\ &= \frac{Q_j}{\gamma}+\overline{\rho}D_j, \end{aligned}\tag{7.13}$$

where

$$D_j=\frac{1}{2}\left(\widetilde{u_ju_ku_k}-\widetilde{u}_j\widetilde{u_ku_k}\right)=\frac{1}{2}\left(\widetilde{u_ju_ku_k}-\widetilde{u}_j\widetilde{u}_k\widetilde{u}_k-\widetilde{u}_j\tau_{kk}\right)\tag{7.14}$$

is similar to the turbulence diffusion that appears in the subgrid-scale kinetic energy equation. Knight *et al.* (1998) proposed that $D_j \simeq \tau_{jk}\widetilde{u}_k$. The other two unclosed terms in (7.13) do not require separate modeling, since they include the already-modeled SGS stresses and heat flux. Term IV is usually neglected, term X can be expressed in terms of the SGS heat flux Q_j using (7.11); term XI is analogous to the SGS viscous dissipation VI in the internal energy or enthalpy equations, and is probably not negligible.

Vreman *et al.* (1995b) derived an equation for a modified total energy, the total energy of the filtered field, $\widehat{\rho E}=\overline{\rho}(\widetilde{\epsilon}+\widetilde{u}_k\widetilde{u}_k/2)$. In this transport equation the pressure-dilatation term V, the SGS viscous dissipation VI, and a term of the form $\widetilde{u}_j(\partial\tau_{ij}/\partial x_i)$ require modeling.

In summary, in compressible flows the following terms are unclosed:

1. SGS stresses τ_{ij} (from I); various models have been proposed, based on incompressible models such as eddy-viscosity (Yoshizawa 1986), mixed (Speziale *et al.* 1988), dynamic (Moin *et al.* 1991, El-Hady *et al.* 1994), and structure function (Normand & Lesieur 1992) models. The need to predict the normal stresses increases the model complexity (an additional model coefficient may be required).

2. SGS heat flux Q_j (from III, VII or IX); it can be obtained from the SGS stress term by using either a constant or a dynamically-adjusted turbulent Prandtl number (Moin *et al.* 1991) or a mixed model (Speziale *et al.* 1988).

3. Pressure dilatation, V (the velocity-pressure gradient term can be reduced to the pressure dilatation, and the pressure diffusion can be modeled directly in terms of Q_j). Vreman *et al.* (1995b) proposed a scale-similar model for this term.

4. Viscous dissipation (term VI) or viscous work of (term XI), depending on the equation chosen. Vreman *et al.* (1995b) proposed a scale-similar model for this term as well.

5. Turbulent diffusion D_j in (7.14). This appears only if the total energy equation is used.

6. Terms arising from the nonlinearity of the diffusive fluxes (II and V). It is probably safe to neglect them at low or moderate temperatures.

If the diffusive nonlinearities are neglected, depending on the set of equations chosen, four of the above terms must be modeled: models for the SGS stresses and heat flux are always required, as well as a model for one of the viscous terms. The internal energy, enthalpy and modified energy equations require modeling of the pressure dilatation, while the total energy requires modeling of the divergence of the turbulent diffusion D_j. It is not known whether there are advantages to either approach.

While Vreman *et al.* (1995b) found most of these terms to be important in a mixing layer, a comparison of the unclosed terms in the energy equation is shown in Fig. 7.1 for a 128^3 simulation of homogeneous isotropic decay with turbulent Mach number $M_t = 0.52$, Reynolds number (based on the Taylor microscale λ) $Re_\lambda = 34.5$, and a filter width $\overline{\Delta}/\Delta = 4$ (Martín *et al.* 2000). The pressure-diffusion term, which does not require separate modeling but can be expressed in terms of Q_j is significant, while the pressure-dilatation term is negligible. The viscous terms are also negligible, while the turbulent diffusion is significant.

Subgrid-scale stress modeling for compressible flows is at a much less advanced stage than for incompressible ones, partly due to the lack of suitable databases for *a priori* tests. Correspondingly, there are few baseline calculations of building-block flows, and very few *a posteriori* evaluations of SGS models.

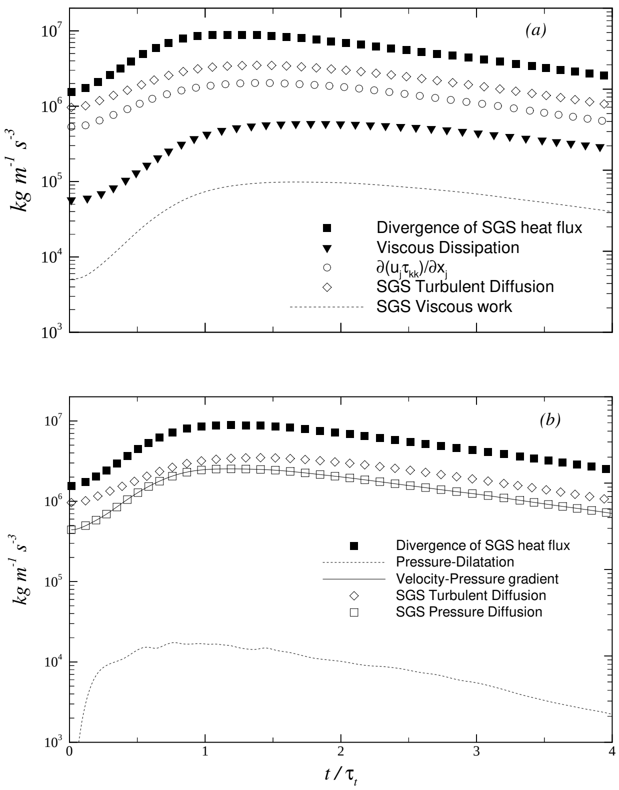

Figure 7.1: Comparison of unclosed terms in the energy equations (Martín *et al.* 2000).

7.2 Wall layer modeling

Perhaps the most urgent challenge that needs to be met, in order to apply LES to technologically relevant flows, is the modeling of the wall layer. The presence of a solid boundary affects the physics of the subgrid scales in several ways. First, the growth of the small scales is inhibited by the presence of the wall. Secondly, the exchange mechanisms between the resolved and unresolved scales are altered; in the near-wall region the subgrid scales may contain some significant Reynolds-stress producing events, and the SGS model must account for them. Finally, the length scale of the energy-carrying large structures is Reynolds-number dependent near the wall. If the wall layer is resolved, the important energy-producing events must be captured; since their dimensions scale with the Reynolds number, so will the cost of an LES calculation. It was mentioned previously that Chapman (1979) estimated that the resolution required for the outer layer of a boundary layer is proportional to $Re^{0.4}$, while for the wall layer (which, in aeronautical applications, only accounts for approximately 1% of the boundary layer thickness) the number of points needed increases at least like $Re^{1.8}$. This requirement makes application of LES to high (order of $10^6 - 10^9$) flows practically impossible.

Alternatively, approximate boundary conditions, or wall models, may be used. When the grid is not fine enough to resolve the near-wall eddies, the wall layer must be modeled by specifying a correlation between the velocity in the outer flow and the stress at the wall. This approach allows the first grid point to be located in the logarithmic layer, and, since the energy-producing vortical structures in the viscous and buffer regions do not have to be resolved, it permits the use of coarser meshes in the other directions as well: $\Delta x^+ \simeq 100-600$, $\Delta z^+ \simeq 100-300$. The modeling of the wall-layer physics, however, introduces further empiricism in the calculations. The basic assumption behind this approach is that the interaction between the modeled, near-wall region, and the resolved, outer region, is weak. Some support for this assumption can be obtained, for instance, from a recent paper of Brooke & Hanratty (1993), in which the way the near-wall vortices are born is investigated utilizing DNS databases from a turbulent channel flow. They found that the flow structures in the viscous wall region, which are responsible for most of the shear stress production, regenerate themselves; no interaction with the outer layer structures was detected.

In general terms, wall models are based on a zonal approach in which the inner and outer layer are treated using different sets of equations, and different modeling strategies. In the outer layer, the filtered Navier-Stokes equations are used. In the inner layer, various alternatives are possible. If one assumes that only the Reynolds shear stress is significant, and that Prandtl's mixing-length hypothesis holds, the inner-layer equations can be integrated analytically, yielding the logarithmic law-of-the-wall (Deardorff 1970, Schumann 1975, Piomelli *et al.* 1989). With this approach, the stress at the wall can be computed in terms of the velocity at the first inner point, for example by solving the logarithmic law for u_τ. This approach assumes that the dynamics of the wall layer are universal, and that some generalized law-of-the-wall can be imposed.

Another option, which was first proposed by Balaras and coworkers (Balaras & Benocci 1994, Balaras *et al.* 1996) consists in solving the boundary-layer equations in the inner layer with some turbulence model. This approach is based on the consideration that, as the Reynolds number increases, a significant disparity of length and time-scales develops between the near-wall region and the outer flow. If the grid-cell dimensions are large compared to the typical eddy size in the near-wall layer, the cell closest to the wall will contain a very large number of such eddies (Fig. 7.2), large enough to be considered a statistically significant sample. Furthermore, since these eddies are small compared to the grid size, their life-cycle is short compared to the time-step. Thus, the filtered velocity is not affected directly by each of these eddies, but only by their combined effect, and it is not necessary to resolve separately each Reynolds-stress-producing event that takes place in the wall-layer, but only to account for them in a statistical sense, through a RANS-like model. In the outer flow, then, the filtered Navier-Stokes equations are solved using as the wall-boundary condition the wall stress supplied by the inner-layer calculation. In the inner layer (*i.e.*, from the first grid point, to the wall), the boundary-layer equations for the mean (*i.e.*, averaged over the cell, in the plane parallel to the solid boundary) velocity are solved. The velocity profile obtained in this manner yields the cell-averaged viscous stress at the wall, required for the calculation of the outer flow at the next time-step.

The two-layer model was applied by Balaras *et al.* (1996) to the flow in a plane channel, in a square duct and in a rotating channel. The model gave better results than models based on the law-of-the-wall, most notably for the rotating channel flow, in which significant deviations from the logarithmic profile are

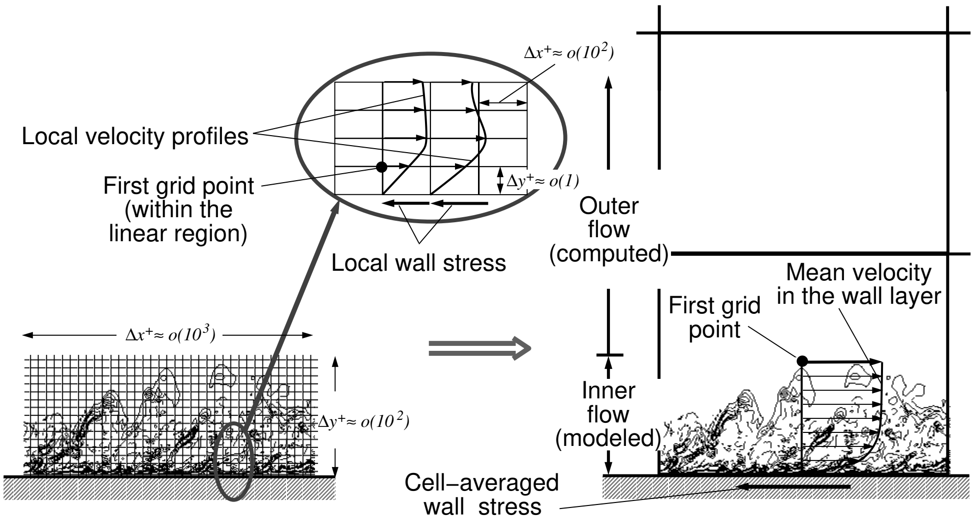

Figure 7.2: Sketch of the two-layer model concept.

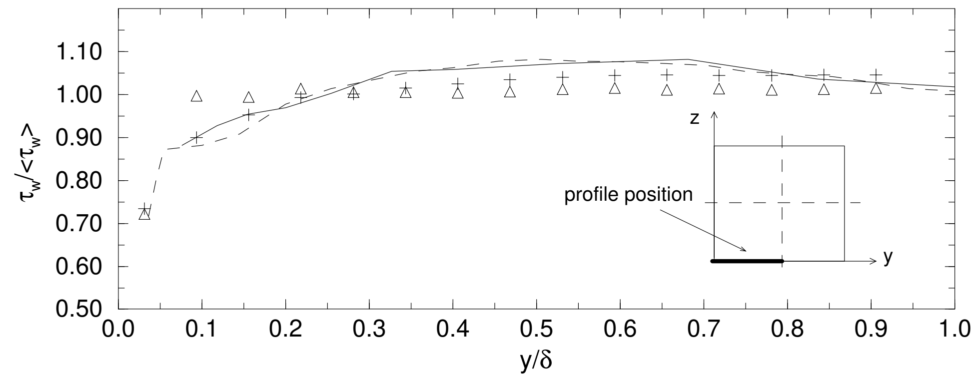

Figure 7.3: Square duct flow; $\tau_w/\langle\tau_w\rangle$ profile along the lower wall. + Two-layer model; △ shifted model; ——— , – – – experimental data. Reproduced with permission from Balaras *et al.* (1996).

observed, that were captured well by the two-layer model (see Fig. 6.7). The calculation of the flow in the square duct also gave results in good agreement with the experimental data (Fig. 7.3). Backward-facing step calculations were performed by Cabot (1996), who used the Balaras *et al.* (1996) formulation, and Diurno *et al.* (2001). The LES gives fairly good prediction of the mean flow (Fig. 7.4): the reattachment region is predicted to within 5% of the value obtained from the resolved LES, at a fraction of the cost (the simulation that uses the approximate boundary conditions requires about two hours on a Pentium II 300MHz processor, whereas the resolved LES (Akselvoll and Moin 1996) used 20-30 Cray CPU hours).

An alternative method has been recently proposed by Spalart *et al.* (1997). It is also a zonal approach, based on the consideration that RANS model predict attached boundary layers fairly accurately, but fail to predict the separated flow regions well; in particularly, they do not capture adequately the vortex shedding that is responsible for much of the noise generation in such flows, as well as for unsteady loads. Due to its emphasis on the prediction of the flow in separated regions, this technique is known as "Detached Eddy Simulation" (DES). With DES, not only the wall layer, but the entire boundary layer is computed using the RANS framework.

In massively separated flows, DES has met with some success. Costantinescu & Squires (2000a,2000b) have performed calculations of the flow over a sphere. They compared several approaches: the standard LES, in which the boundary layer on the sphere is fully resolved, the DES technique, and the unsteady RANS (URANS) approach, in which the ensemble-averaged Navier-Stokes equations are solved using a standard turbulence model. URANS are supposed to be able to capture the large-scale unsteadiness of

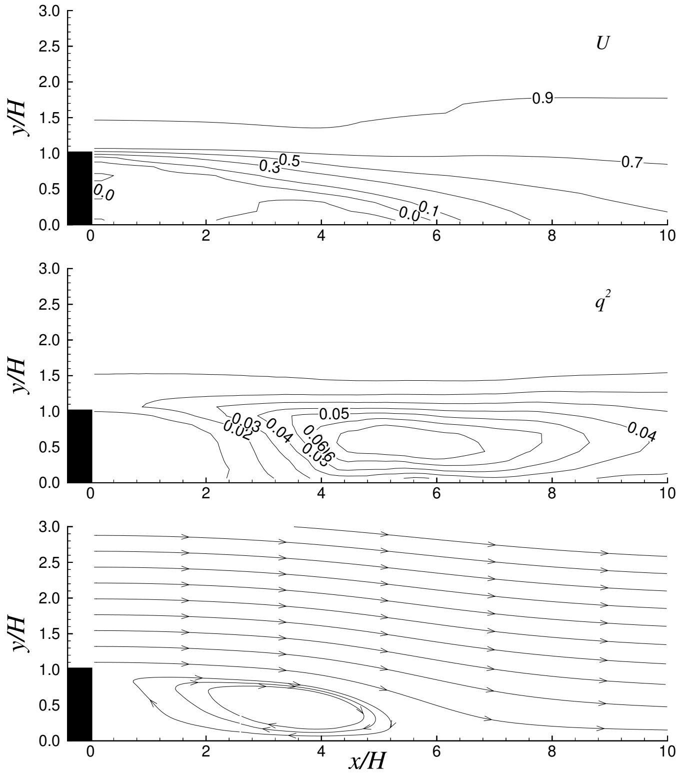

Figure 7.4: Flow over the backward-facing step; $Re = 5,100$. Top: mean velocity contours; middle: contours of $q^2 = \langle u_i' u_i' \rangle$; bottom: streamlines. Reproduced with permission from Diurno *et al.* (2001).

the flow (in this case, the shed vortices). The LES used the dynamic eddy-viscosity model (Germano *et al.* 1991, Lilly 1992). The DES used a modification of the Spalart-Allmaras (1994) model, a one-equation model based on a single transport equation for the eddy viscosity that is widely used in aerodynamics. The URANS computations used various models such as the $\mathcal{K}-\varepsilon$ and $\mathcal{K}-\omega$ two-equation models, the $v^2 - f$ model (Durbin 1991) and the Spalart-Allmaras (1994) model.

In Fig. 7.5 a comparison of the instantaneous out-of-plane vorticity is shown. The unsteady RANS calculations fail to predict the instability of the separating shear layer that leads to the generation of vortex tubes in the wake of the sphere, as well as the unsteady eddies in the recirculating region. The $\mathcal{K}-\varepsilon$ model, in particular, does not predict the shear-layer development with any degree of accuracy. DES predicts the unsteady, three-dimensional structure of the recirculating region much more accurately. Both LES and DES predict the energy content and frequency of the shedding much more accurately than any of the RANS models, although the LES demonstrates a better capability in capturing the development of the Kelvin-Helmholtz instability in the detached shear layer.

7.3 URANS, LES and commercial codes

The calculations described in the previous Section highlight significant differences between the results obtained with LES and unsteady RANS. These differences result from the conceptual development of the techniques, and affect the modeling, the numerics, the resolution requirements and the boundary conditions to be applied. As commercial codes increasingly include an LES option, it is important to highlight these differences, and to give some words of caution to potential users of such codes.

The governing equations for unsteady RANS are the ensemble-averaged Navier-Stokes equations. The character of these equations is essentially different from that of the filtered Navier-Stokes equations solved in LES. First, if the grid size is decreased, since the filter size is related to the grid, LES tend towards direct simulations: fewer and fewer eddies are removed by the filtering operation until, as $\overline{\Delta} \to 0$ all scales of motion are resolved. In the URANS approach, on the other hand, a Reynolds-stress term is

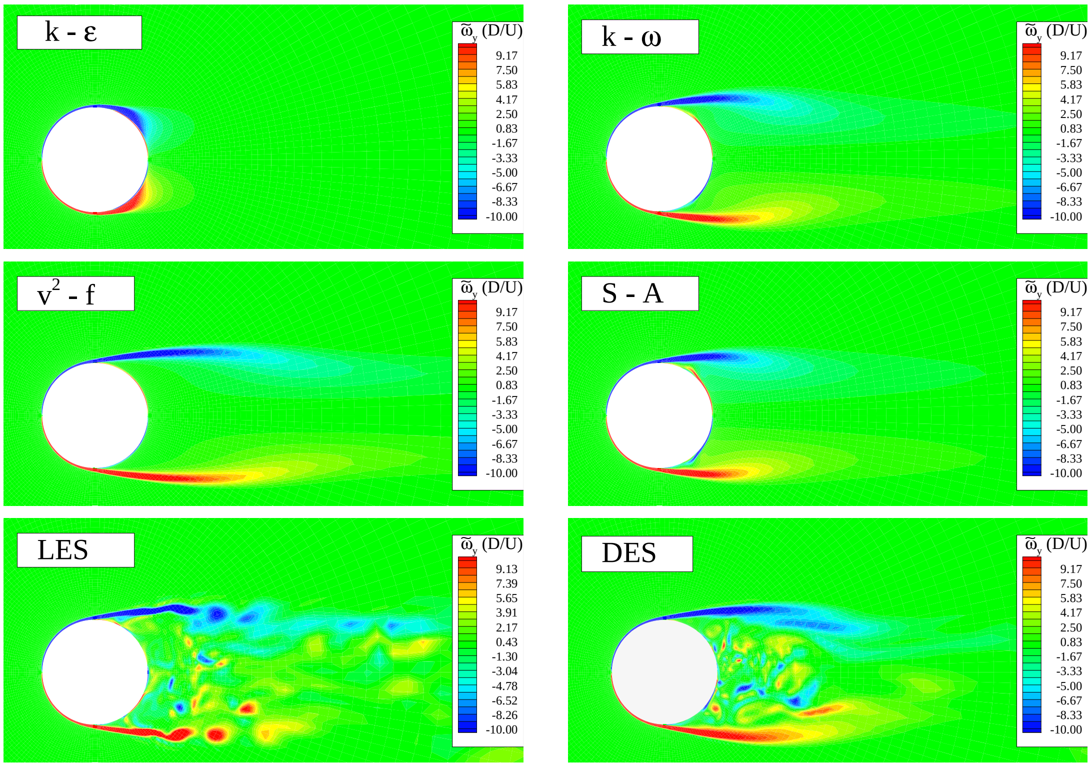

Figure 7.5: Turbulent flow over a sphere. Out-of-plane vorticity contours in an azimuthal plane. Reprinted with permission from Constantinescu & Squires (2000b).

always present, independent of the grid size, to represent the effect of the turbulent fluctuations that are removed by the ensemble average. This difference is reflected in the models: a subgrid-scale model should give (and most do) vanishingly small eddy viscosity as $\overline{\Delta} \to 0$. A $\mathcal{K} - \varepsilon$ model, on the other hand gives Reynolds stresses that become grid-independent (but non-zero) as the grid is refined.

Furthermore, geometric symmetry properties can be exploited in URANS to reduce the computational cost; the sphere calculations described above could have been carried out using an axi-symmetric grid, for instance; similarly, backward-facing step calculations can be two-dimensional. LES, on the other hand, are inherently three-dimensional: the energy-carrying eddies that must be resolved are three-dimensional, and are intensified by the vortex-stretching that that cannot be taken into account in two-dimensional calculations. For this reason, two-dimensional calculations cannot be described as "large-eddy simulations", since they are unable to capture correctly the dynamics of the important vortical structures.

Another important difference is in the boundary conditions required by the two techniques. In RANS and URANS, only the ensemble-averaged velocity (plus whichever turbulent statistics the model requires) need to be specified at inflows. In a flow with large-scale unsteadiness that is not due to the boundary conditions (such as the flow around the sphere) the inflow conditions are steady. Not so for the LES: if the inflow is turbulent, temporally and spatially varying inflow conditions must be specified. As mentioned in Section 3.6, even the use of random noise fluctuations superimposed on a mean velocity profiles may not be sufficient to ensure an accurate prediction of the flow downstream. Similar care must be used when assigning wall boundary conditions: the wall functions that are used in RANS calculations are not always suitable for LES.

The grid requirements of the URANS and LES are also substantially different: in RANS or URANS, only the mean gradients have to be resolved; in LES, all the energy-carrying structures must be computed accurately. The grids required by LES tend, therefore, to be finer than those used by RANS calculations. As a consequence, changing a RANS model to an SGS model on a given grid does not guarantee improved results. On the contrary, if the mesh is insufficient to capture the important three-dimensional structures, switching from, say, a $\mathcal{K}-\varepsilon$ model to a Smagorinsky model is likely to decrease the accuracy, unless the grid is sufficiently fine.

The different characteristics of the two techniques are reflected also in the numerical methods that can be used. RANS and URANS give smooth solutions; the use of upwind schemes in RANS codes is, therefore, not tremendously damaging. In LES, on the other hand, the numerical dissipation of upwind schemes affects the accuracy of the results substantially. Among its typical symptoms are thickening of the wall layers (and high values of the intercept of the logarithmic layer); reduced turbulence intensities, especially in regions of relaminarization; delay, or even suppression, of the onset of transition. Upwind methods, are often the default in commercial codes, in which the robustness of the method is an important priority; however, should be avoided when performing LES.

Chapter 8

CONCLUSIONS

It was the purpose of these Lecture Notes to give an introduction to two methods that have become increasingly popular for the solution of turbulent flow problems, the direct and large-eddy simulation techniques. It is hoped that they constitute a suitable starting point for more in-depth readings for those interested in using LES, and that they supply the peruser of the technical literature with the tools to understand better the power, limitations and achievements of these approaches.

Direct simulations have been mostly an instrument for the study of the physics of turbulence, since resolution requirements limit their application to relatively low Reynolds numbers. Although engineering configurations are beyond the capabilities of DNS, at least in the near future. DNS, however, allow very detailed control over the flow parameters, which can be used in aeroacoustics, applications involving reacting flows and flow control.

The purpose, and range of application, of LES overlaps with the applications suitable for DNS on one end, those suitable for RANS methodologies on the other. The principal advantage of LES over DNS is the fact that it allows one to compute flows at Reynolds numbers much higher than those feasible in DNS, or at the same Reynolds numbers but at a considerably smaller expense. One should not expect to be able to extract from LES the same information that can be extracted from DNS, since modeling the small scales affects high-order statistics more than the lower-order ones. Thus, LES is expected to be more reliable for first and second moments, and to reproduce qualitatively the basic structures of the flows (existence of shear layers, vortical structures and so on).

Large-eddy simulation is considerably more expensive than RANS techniques for flows that are one- or two-dimensional in the mean and steady. For this reason, it should be applied to problems in which its cost is comparable to that of the solution of the RANS equations or to problems in which lower-level turbulence models fail. Such problems include unsteady or three-dimensional boundary layers, vortex–boundary layer interactions, separated flows and flows involving geometries with sharp corners (in square ducts, for example).

Large-eddy simulation has already demonstrated its capabilities in calculations of relatively complex flows, at Reynolds numbers that could not be reached by DNS. At present, to maximize the returns, LES should be applied to problems in which its cost is comparable to that of the solution of the RANS equations, or to problems in which lower-level turbulence models fail. Such problems include unsteady or three-dimensional boundary layers, vortex-boundary layer interactions, separated flows and flows involving geometries with sharp corners. These are problems in relatively simple geometries, that, however, isolate one (or a few) of the factors that are expected to be relevant in such configurations, albeit within a simplified geometry. Large-eddy simulation of these flows can improve the understanding of the turbulence physics, and also be used to provide data for the development of more accurate lower-level models (especially pressure statistics, which are difficult to measure experimentally).

Among its next targets are, first and foremost, flows that include additional geometric, as well as physical, complexities. Interest in compressible flows and in aeroacoustics is also increasing. The challenges that need to be faced to achieve significant advancements in these areas include the development of near-wall models, of accurate non-equilibrium and compressible SGS models, and of high-order methods in curvilinear coordinates and on unstructured meshes.

Progress in computer technology has made it possible to perform significant calculations on affordable desktop workstations. The simulations that required hundreds of Cray XMP CPU hours when the author was working on his dissertation, ten years ago, are now routinely carried out by his students on Pentium II machines. Further technological advances will benefit both the affordability of run-of-the-mill calculations, and the possibility of performing larger, leading-edge calculations in parallel environments.

Large-eddy and direct simulations should not be construed as fool-proof tools to obtain answers to turbulent flow problems, nor, yet, as design tools that can be used for real-time optimization. With these *caveats* in mind, however, the outlook for these techniques is reasonably bright. The notable advancements in modeling and numerics over the last few years, and the increasing number of researchers that are applying their talents in the nnumerical simulation area are both a measure of past achievements, and a reason for optimism for the future.

Bibliography

Akselvoll, K., & Moin, P. 1996 Large-eddy simulation of turbulent confined coannular jets. *J. Fluid Mech.* **315**, 387.

Anderson, R., & Meneveau, C. 1999 Effects of the similarity model in finite-difference LES of decaying isotropic turbulence using a Lagrangian dynamic mixed model. *Flow, Turbulence and Combustion* **62**, 201.

Balaras, E., & Benocci, C. 1994 Subgrid-scale models in finite-difference simulations of complex wall bounded flows. *AGARD CP 551*, 2.1.

Balaras, E., Benocci, C., & Piomelli, U. 1996 Two-layer approximate boundary conditions for large-eddy simulations. *AIAA J.* **34**, 1111.

Bardina, J., Ferziger, J. H., & Reynolds, W. C. 1980 Improved subgrid scale models for large eddy simulation. *AIAA Paper No. 80–1357.*

Bardina, J., Ferziger, J. H. & Rogallo, R.S. 1985 Effect of rotation on isotropic turbulence: computation and modelling. *J. Fluid Mech.* **154**, 321.

Bewley, T. R., Temam, R., & Moin, P. 2000 DNS-based predictive control of turbulence: an optimal benchmark for feedback algorithms. Submitted to *J. Fluid Mech.*

Brooke, J. W., & Hanratty, T. J. 1993 Origin of turbulence-producing eddies in a channel flow. *Phys. Fluids* **5**,1011 (1993).

Brown, G.L. & Roshko, A. 1974 On density effects and large structure in turbulent mixing layers. *J. Fluid Mech.* **64**, 775-816.

Cabot, W. H. 1996 Near-wall models in large-eddy simulations of flow behind a backward-facing step. In *Ann. Res. Briefs–1996.* Center for Turbulence Research, NASA Ames/Stanford Univ., 199.

Canuto, C., Hussaini, M. Y., Quarteroni, A., and Zang, T. A. 1988 *Spectral methods in fluid dynamics* (Springer-Verlag, Heidelberg).

Chapman, D. R. 1979 Computational aerodynamics development and outlook *AIAA J.* **17**, 1293.

Choi, H., Moin, P., & Kim, J. 1993 Direct numerical simulation of turbulent flow over riblets. *J. Fluid Mech.* **255**, 503.

Choi, H., Moin, P., & Kim, J. 1994 Active turbulence control for drag reduction in wall-bounded flows. *J. Fluid Mech.* **262**, 75.

Chollet, J. P. 1984 Two-point closures as a subgrid modelling for large-eddy simulation. In *Turbulent Shears Flow IV*, edited by F. Durst and B. Launder, (Springer-Verlag, Heidelberg), 62.

Chollet, J. P. & Lesieur, M. 1981 Parameterization of small scales of three-dimensional isotropic turbulence utilizing spectral closures. *J. Atmo. Sci.* **38**, 2747.

Chorin, A. J. 1969 Numerical solution of the Navier-Stokes equations. *Math. Comput.* **22**, 745.

COLEMAN, G. N., KIM, J. & LE, A. T. 1996 A numerical study of three-dimensional wall-bounded flows. *Int. J. Heat Fluid Flow* **17**, 333.

COMTE, P., SILVESTRINI, J. H., & BÉGOU, P. 1998 Streamwise vortices in large-eddy simulations of mixing layers, *Eur. J. Mech. B/Fluids* **17**, 615.

COSTANTINESCU, G. S., & SQUIRES, K. D. 2000a LES and DES investigation of turbulent flow over a sphere. *AIAA Paper 2000–0540.*

COSTANTINESCU, G. S., & SQUIRES, K. D. 2000b Prediction of turbulent flow over a sphere. Submitted to *AIAA J.*

DEARDORFF, J. W. 1970 A numerical study of three-dimensional turbulent channel flow at large Reynolds numbers. *J. Fluid Mech.* **41**, 453.

DE BRUIN, I., GEURTS, B., DRIESEN, C., & KUERTEN J. 1999 Robustness of flow phenomena in a spatially developing turbulent mixing layer. In *Recent advances in DNS and LES*, edited by D. Knight and L. Sakell (Kluwer, Dordrecht), pp. 111–120.

DELCAYRE, F. & LESIEUR, M. 1997 In *Advances in DNS/LES*, edited by C. Liu and Z. Liu, (Greyden Press, Columbus), 425.

DIURNO, G.V., BALARAS E., & PIOMELLI U. 2001. "Wall-layer models for LES of separated flows." In *Modern simulation strategies for turbulent flows*, ed. B Geurts, pp. 207–222. Philadelphia:RT Edwards.

DOMARADZKI, J. A., LIU, W., HÄRTEL, C., AND KLEISER, L. 1994 Energy transfer in numerically simulated wall-bounded turbulent flows. *Phys. Fluids* **6**, 1583.

DOMARADZKI, J. A. & SAIKI, E. M. 1997 "A subgrid-scale model based on the estimation of unresolved scales of turbulence." *Phys. Fluids* **9**, 2148.

DOMARADZKI, J. A. & LOH, K.-C. 1999 "The subgrid-scale estimation model in the physical space representation." *Phys. Fluids* **11**, 2330.

DOMARADZKI, J. A. & YEE, P. P. 2000 "The subgrid-scale estimation model for high Reynolds number turbulence." *Phys. Fluids* **12**, 193.

DRIVER, D. M. & HEBBAR, S. K. 1987 Experimental study of a three-dimensional, shear-driven, turbulent boundary layer. *AIAA J.* **25**, 35.

DRIVER, D. M. & JOHNSTON, J. P. 1990 Experimental study of a three-dimensional shear-driven turbulent boundary layer with streamwise adverse pressure gradient. *NASA TM 102211.*

DUCROS, F., COMTE, P., & LESIEUR, M. 1996 Large-eddy simulation of transition to turbulence in a boundary layer developing spatially over a flat plate. *J. Fluid Mech.* **326**, 1.

DURBIN, P. A. 1991 Near-wall turbulence closure without damping functions. *Theoret. Comput. Fluid Mech.* **3**, 659.

EL-HADY, N., ZANG, T. A., & PIOMELLI, U. 1994 Application of the dynamic subgrid-scale model to axisymmetric transitional boundary layer at high speed. *Phys. Fluids A* **6**, 1299.

ERLEBACHER, G., HUSSAINI, M. Y., SPEZIALE, C. G., & ZANG, T. A. 1992 Toward the large-eddy simulation of compressible turbulent flows, *J. Fluid Mech.* **238**, 155.

FAVRE, A. 1965a Équations des gaz turbulents compressible. I. Formes générales. *J. de Mécanique* **4**, 361.

FAVRE, A. 1965b Équations des gaz turbulents compressible. II. Méthode des vitesses moyennes; méthode des vitesses macroscopiques pondérées par la masse volumique. *J. de Mécanique* **4**, 391.

GERMANO, M. 1992 Turbulence: the filtering approach. *J. Fluid Mech.* **238**, 325.

GERMANO, M., PIOMELLI, U., MOIN, P. AND CABOT W. H. 1991 A dynamic subgrid-scale eddy viscosity model. *Phys. Fluids A* **3**, 1760.

GHOSAL, S., & MOIN, P. 1995 The basic equations for the large eddy simulation of turbulent flows in complex geometries, *J. Comput. Phys.* **118**, 24.

GHOSAL, S., LUND, T. S., MOIN, P. & AKSELVOLL, K. 1995 A dynamic localization model for large-eddy simulation of turbulent flow. *J. Fluid Mech.* **286**, 229.

HAMMOND, E. P., BEWLEY, T. R., & MOIN, P. 1998 Observed mechanisms for turbulence attenuation and enhancement in opposition-controlled turbulent channel flow. *Phys. Fluids* **10**, 2421.

HUAI, X., JOSLIN, R. D., & PIOMELLI, U. 1997 Large-eddy simulation of transition to turbulence in boundary layers. *Theoret. Comput. Fluid Dyn.* **9**, 149.

HUNT, J. C. R., WRAY, A. A., & MOIN, P. 1988 Eddies, Streams and Convergence Zones in Turbulent Flows. *Proc. Summer Program 1988*, Center for Turbulence Research, 193.

JOHNSTON, J. P., HALLEEN, R. M., & LEZIUS, R. K. 1972 Effect of spanwise rotation on the structure of two-dimensional fully developed turbulent channel flow. *J. Fluid Mech.* **56**, 533.

KALTENBACH, H-J., FATICA, M., MITTAL, R., LUND, T. S., & MOIN, P. 1999 Study of flow in a planar asymmetric diffuser using large-eddy simulation. *J. Fluid Mech.* **390**, 151.

KANNEPALLI, C., & PIOMELLI, U. 2000 Large-eddy simulation of a three-dimensional shear-driven turbulent boundary layer. *J. Fluid Mech.* **423**, pp. 175–203.

KIM, J., & MOIN, P. 1985 Application of a fractional step method to incompressible Navier-Stokes equations. *J. Comput. Phys.* **59**, 308.

KIM, J., MOIN, P. & MOSER, R. D. 1987 Turbulence statistics in fully developed channel flow at low Reynolds number. *J. Fluid Mech.* **177**, 133.

KLINE, S.J., REYNOLDS, W.C., SCHRAUB, F.A., & RUNSTADLER, P.W. 1967 The structure of turbulent boundary layers. *J. Fluid Mech.* **30**, 741.

KNIGHT, D., ZHOU, G., OKONG'O, N., AND SHUKLA, V. 1998 Compressible large eddy simulation using unstructured grids. *AIAA Paper 98-0535.*

KRAICHNAN, R. H. 1976 Eddy viscosity in two and three dimensions. *J. Atmo. Sciences* **33**, 1521.

KRAVCHENKO, A., MOIN, P., & MOSER, R. D. 1996 Zonal embedded grids for numerical simulations of wall-bounded turbulent flows. *J. Comput. Phys.* **127**, 412.

KRAVCHENKO, A. 1998 B-spline methods and zonal grids for numerical simulations of turbulent flows.*Ph. D. Dissertation*, Stanford University.

KRAVCHENKO, A., & MOIN, P. 2000 Numerical studies of flow over a circular cylinder at $Re_D =$ 3900. *Phys./ Fluids* **12**, 403–417.

KRISTOFFERSEN, R., & ANDERSSON, H. I. 1993 Direct simulation of low-Reynolds number turbulent flow in rotating channel. *J. Fluid Mech.* **256**, 163.

LAMBALLAIS, E., MÉTAIS, O., & LESIEUR, M. 1998 Spectral-dynamic model for large-eddy simulations of turbulent rotating channel flow. *Theoret. Comput. Fluid Dyn.* **12**, 149.

LE, H., MOIN, P. & KIM, J. 1997 Direct numerical simulation of turbulent flow over a backward-facing step, *J. Fluid Mech.* **330**, 349.

LEE, S., LELE, S. K., & MOIN, P. 1992 Simulation of spatially evolving turbulence and the applicability of Taylor's hypothesis in compressible flow, *Phys. Fluids A* **4**, 1521.

LEONARD, A. 1974 Energy cascade in Large-Eddy Simulations of turbulent fluid flows. *Adv. Geophys.* **18A**, 237.

LESIEUR, M. & MÉTAIS, O. 1995 New trends in large-eddy simulation of turbulence. *Annu. Rev. Fluid Mech.* **28**, 45 (1995).

LI, N., BALARAS, E., & PIOMELLI, U. 2000 Inflow conditions for large-eddy simulations of mixing layers. To appear, *Phys. Fluids* **12**.

LILLY, D. K. 1967 The Representation of Small-Scale Turbulence in Numerical Simulation Experiments. *Proc. IBM Scientific Computing Symposium on Environmental Sciences.* Yorktown Heights, N.Y., 195.

LILLY, D. K. 1992 A proposed modification of the Germano subgrid-scale closure method. *Phys. Fluids A* **4**, 633.

LIU, J., PIOMELLI, U., & SPALART, P. R. 1996 Interaction between a spatially growing turbulent boundary layer and embedded streamwise vortices. *J. Fluid Mech.* **326**, 151.

LIU, S., MENEVEAU, C., & KATZ, J. 1994 On the properties of similarity subgrid–scale models as deduced from measurements in a turbulent jet. *J. Fluid Mech.* **275**, 83.

LOHMANN, R. P. 1976 Response of a developed boundary layer to local transverse surface motion. *ASME J. Fluids Engng* **98**, 151.

LUMLEY, J., & BLOSSEY, P. 1998 Control of turbulence. *Annu. Rev. Fluid Mech.* **30**, 311–327.

LUND, T. S., WU, X., & SQUIRES, K. D. 1998 Generation of inflow data for spatially-developing boundary layer simulations, *J. Comput. Phys.* **140**, 233.

MANSOUR, N. N., KIM, J., AND MOIN, P. 1988 Reynolds stress and dissipation-rate budgets in a turbulent channel flow. *J. Fluid Mech.* **194**, 15.

MARTÍN, M. P., PIOMELLI, U., & CANDLER, G. V. 2000 Subgrid-scale models for compressible large-eddy simulations. *Theoret. Comput. Fluid Dynamics* **13**, 361.

MCMILLAN, O. J., FERZIGER, J. H. & ROGALLO, R. S. 1980 Tests of new subgrid-scale models in strained turbulence. *AIAA Paper No. 80–1339.*

MENEVEAU, C., LUND, T. S., & CABOT, W. H. 1996 A Lagrangian dynamic subgrid-scale model of turbulence. *J. Fluid Mech.* **319** 353.

MENEVEAU, C., & KATZ, J. 2000 Scale-invariance and turbulence models for large-eddy simulation. *Annu. Rev. Fluid Mech.* **32**, 1.

MOIN, P. 1997 Progress in large eddy simulation of turbulent flows. *AIAA Paper No. 97-0749.*

MOIN, P., SQUIRES, K. D., CABOT, W. H., & LEE, S. 1991 A dynamic subgrid-scale model for compressible turbulence and scalar transport. *Phys. Fluids A* **3**, 2746.

MOIN, P., & MAHESH, K. 1998 Direct numerical simulation: A tool in turbulence research. *Annu. Rev. Fluid Mech.* **30**, 539 (1998).

MORINISHI, Y., LUND, T. S., VASILYEV, O. V., & MOIN, P. 1998 Fully conservative higher order finite difference schemes for incompressible flows. *J. Comput. Phys.* **143**, 90.

NORMAND, X. AND LESIEUR, M. 1992 Direct and large-eddy simulation of laminar breakdown in high-speed axisymmetric boundary layers. *Theoret. Comput. Fluid Dyn.* **3**, 231.

ORLANSKY, I. 1976 A simple boundary condition for unbounded hyperbolic flows. *J. Comput. Phys.* **21**, 251.

Pierce, C. D., & Moin, P. 1998 Method for generating equilibrium swirling flow conditions. *AIAA J.* **36** 1325.

Piomelli, U. 1993 High Reynolds number calculations using the dynamic subgrid-scale stress model. *Phys. Fluids A* **5**, 1484.

Piomelli, U. 1999 Large-eddy simulation: achievements and challenges. *Progress Aero. Sci.* **35**, 335.

Piomelli, U., Moin, P. & Ferziger, J. H. 1988 Model consistency in large eddy simulation of turbulent channel flows. *Phys. Fluids* **31**, 1884.

Piomelli, U., Moin, P., Ferziger, J. H., & Kim, J. 1989 New approximate boundary conditions for large eddy simulations of wall-bounded flows. *Phys. Fluids A* **1**, 1061.

Piomelli, U., Zang, T. A., Speziale, C. G., & Hussaini, M.Y. 1990 On the large-eddy simulation of transitional wall-bounded flows. *Phys. Fluids A* **2**, 257.

Piomelli, U. and Liu, J. 1995 Large eddy simulation of rotating channel flows using a localized dynamic model. *Phys. Fluids A* **7**, 839.

Piomelli, U. & Chasnov, J. R. 1996 Large-eddy simulations: theory and applications. In *Transition and turbulence modelling*, edited by D. Henningson, M. Hallbäck, H. Alfreddson and A. Johansson, (Kluwer Academic Publishers, Dordrecht), 269.

Piomelli, U., Yu, Y., and Adrian, R. J. 1996 Subgrid-scale energy transfer and near-wall turbulence structure. *Phys. Fluids* **8**, 215.

Piomelli, U., Coleman, G. N., & Kim, J. 1997 On the effects of non-equilibrium on the subgrid-scale stresses. *Phys. Fluids* **9**, 2740.

Piomelli, U., Balaras, E., & Pascarelli, A. 2000 Turbulent structures in accelerating boundary layers. Submitted to *Journal of Turbulence*.

Rai, M. M., & Moin, P. 1993 Direct numerical simulation of transition and turbulence in a spatially evolving boundary layer. *J. Comput. Phys.* **109**, 169.

Robinson, S. K. 1991a Coherent motions in the turbulent boundary layer. *Annu. Rev. Fluid Mech.* **23**, 601.

Robinson, S. K. 1991b The kinematics of turbulent boundary layer structure. *NASA TM-103859.*

Rogers, M. M., Mansour, N. N., and Reynolds, W. C. 1989 An algebraic model for the turbulent flux of a passive scalar. *J. Fluid Mech.* **203**, 77.

Sarghini, F., Piomelli, U., & Balaras, E. 1999 Scale-similar models for large-eddy simulations. *Phys. Fluids* **11**, 1607.

Schumann, U. 1975 Subgrid scale model for finite difference simulation of turbulent flows in plane channels and annuli. *J. Comput. Phys.* **18**, 376.

Scotti A. & Piomelli, U. 2001 "Numerical simulation of pulsating channel flow." *Phys. Fluids* **13**, 1367.

Shah, K. B. & Ferziger, J. H. 1995 "A new non-eddy viscosity subgrid-scale model and its application to channel flow." In *Center for Turbulence Research Annual Briefs 1995* Stanford University, 73.

Smagorinsky, J. 1963 General circulation experiments with the primitive equations. I. The basic experiment. *Monthly Weather Review* **91**, 99.

Spalart, P. R. 1986 Numerical study of sink-flow boundary layers. *J. Fluid Mech.* **172**, 307.

SPALART, P. R. 1988 Direct numerical simulation of a turbulent boundary layer up to $Re_\theta = 1410$. *J. Fluid Mech.* **187**, 61.

SPALART, P. R. & WATMUFF, J. H. 1993 Experimental and numerical study of a turbulent boundary layer with pressure gradients. *J. Fluid Mech.* **249**, 337.

SPALART, P.R. AND ALLMARAS, S. R. 1994 A one-equation turbulence model for aerodynamic flows. *La Recherche Aérospatiale*, **1**, 5.

SPALART, P. R., JOU, W. H., STRELETS, M., & ALLMARAS, S. R. 1997 Comments on the feasibility of LES for wings, and on a hybrid RANS/LES approach. In *Advances in DNS/LES*, edited by C. Liu and Z. Liu, (Greyden Press, Columbus), 137.

SPEZIALE, C. G., ERLEBACHER, G., ZANG, T. A., & HUSSAINI, M.Y. (1988) The subgrid-scale modeling of compressible turbulence. *Phys. Fluids A* **31**, 940.

STOLZ, S. & ADAMS, N. A. 1999 "An approxmate deconvolution model for large-eddy simulation." *Phys. Fluids* **11**, 1699.

STOLZ, S., ADAMS, N. A., & KLEISER, L. 2001 "An approxmate deconvolution model for large-eddy simulation with application to incompressible wall-bounded flows." *Phys. Fluids* **13**, 997.

STREETT, C. L. & MACARAEG, M. G. 1989 Spectral multi-domain technique for large-scale fluid-dynamic simulations. *Applied Num. Math.* **6**, 123.

VAN DRIEST, E. R. 1956 On the turbulent flow near a wall. *J. Aero. Sci.* **23**, 1007.

VOKE, P., & YANG, Z. 1995 Numerical study of bypass transition. *Phys. Fluids* **7**, 2256.

VREMAN, B., GEURTS, B., & KUERTEN, H. 1995a *A priori* tests of large eddy simulation of the compressible mixing layer. *J. Eng. Math.* **29**, 299.

VREMAN, B., GEURTS, B., & KUERTEN, H. 1995b Subgrid-modeling in LES of compressible flow. *Applied Sci. Res.* **54**, 191.

VREMAN, B., GEURTS, B., & KUERTEN, H. 1997 Large eddy simulation of the turbulent mixing layer. *J. Fluid Mech.* **339**, 357.

WALSH, M. J. 1980 Drag characteristics of V-groove and transverse curvature riblets. In *Viscous drag reduction* (G. R. Hough, ed.), AIAA.

WU, X. & SQUIRES, K. D. 1997 Large-eddy simulation of an equilibrium three-dimensional turbulent boundary layer. *AIAA J.* **35**, 67.

YOSHIZAWA, A. 1986 Statistical theory for compressible turbulent shear flows, with the application to subgrid modeling. *Phys. Fluids A* **29**, 2152.

ZANG, T. A., DAHLBURG, R. B., & DAHLBURG, J. P. 1992 Direct and large-eddy simulations of three-dimensional compressible Navier-Stokes turbulence. *Phys. Fluids A* **4**, 127.

ZANG, Y., STREET, R. L., & KOSEFF, J. 1993 A dynamic mixed subgrid-scale model and its application to turbulent recirculating flows. *Phys. Fluids A* **5**, 3186.